

國立交通大學
光電工程研究所

博士論文

氮化鎵材料發光二極體與面射型雷射之
製作與特性研究

**Fabrication and Characteristics of
GaN-based Light-Emitting Diodes and
Vertical-Cavity Surface-Emitting Lasers**



研究生：朱榮堂

指導教授：王興宗教授

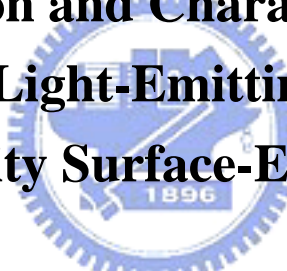
郭浩中教授

中華民國九十七年六月

國立交通大學
光電工程研究所
博士論文

氮化鎵材料發光二極體與面射型雷射之
製作與特性分析

**Fabrication and Characteristics of
GaN-based Light-Emitting Diodes and
Vertical-Cavity Surface-Emitting Lasers**

The logo of National Tsing Hua University is a circular emblem with a blue border. Inside the circle, there is a stylized gear or cogwheel design. At the bottom of the circle, the year '1896' is inscribed.

研究生：朱榮堂

Student: Jung-Tang Chu

指導教授：王興宗

Advisor: Shing-Chung Wang

郭浩中

Hao-Chung Kuo

中華民國九十七年六月

氮化鎵材料發光二極體與面射型雷射之
製作與特性分析

**Fabrication and Characteristics of
GaN-Based Light-Emitting Diodes and
Vertical-Cavity Surface-Emitting Lasers**

研究生：朱 榮 堂
指導教授：王 興 宗
郭 浩 中

**Student: Jung-Tang Chu
Advisor: Shing-Chung Wang
Hao-Chung Kuo**



**A dissertation
Submitted to Institute of Electro-Optical Engineering
College of Electrical Engineering and Computer Science
National Chiao Tung University
In Partial Fulfillment of the Requirements
For the Degree of
Doctor of Philosophy
In Electro-Optical Engineering
June 2008
Hsin-chu, Taiwan**

中華民國 九十七 年 六 月

國立交通大學

論文口試委員會審定書

本校光電工程研究所博士班朱榮堂君

所提論文 氮化鎵材料發光二極體與面射型雷射之製作與特性研究

合於博士資格標準、業經本委員會評審認可。

口試委員：張振雄

張振雄

張守進

張守進

彭隆瀚

彭隆瀚

吳耀銓

吳耀銓

盧廷昌

盧廷昌

指導教授：王興宗

王興宗

郭浩中

郭浩中

所長：趙了取 教授

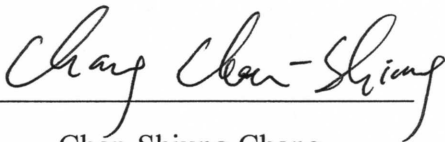
系主任：黃中堯 教授

中華民國 97 年 6 月 18 日

Institute of Electro-Optical Engineering
National Chiao Tung University
Hsinchu, Taiwan, R.O.C.

Date : 18 June, 2008

We have carefully read the dissertation entitled Fabrication and Characteristics of GaN-based Light-Emitting Diodes and Vertical-Cavity Surface-Emitting Lasers submitted by Jung-Tang Chu in partial fulfillment of the requirements of the degree of DOCTOR OF PHILOSOPHY and recommend its acceptance.



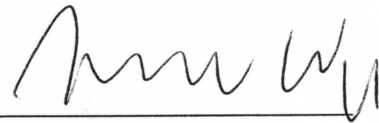
Chen-Shiung Chang



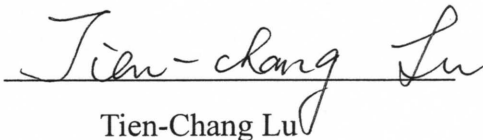
Shou-Jinn Chang



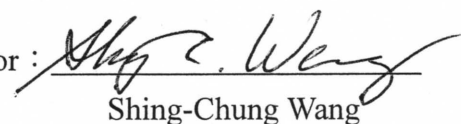
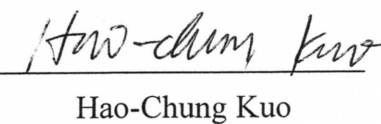
Lung-Han Peng



YewChung Sermon Wu

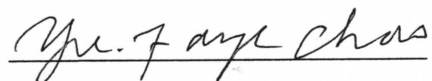


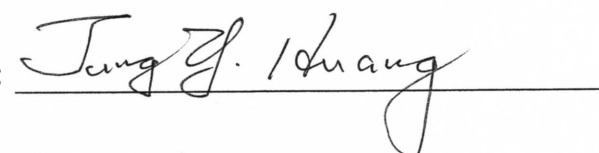
Tien-Chang Lu

Thesis Advisor :  

Shing-Chung Wang

Hao-Chung Kuo

Director of Institute of Electro-Optical Engineering : 

Chairman of Department of Photonics : 

氮化鎵材料發光二極體與面射型雷射之 製作與特性研究

研究生：朱榮堂

指導教授：王興宗 教授
郭浩中 教授

國立交通大學光電工程研究所

摘要

由於氮化鎵基材發光元件可廣泛的應用於如指示燈、各種照明、光儲存等領域，因此自 1960 年代以來氮化鎵相關材料成為世界上各研發團體的重要研究課題之一，且在此數十年間氮化鎵材料與元件特性上有屢有重大的發現與進展。在本研究論文中，我們製作氮化鎵發光二極體(LED)於金屬基板上與包含兩介電質反射鏡的氮化鎵面射型雷射(VCSEL)，並研究分析此二元件之主要特性。

首先我們製作大發光面積 ($1 \times 1 \text{ mm}^2$) 藍光發光二極體於銅基板上。利用金屬接合與雷射剝離製程，成長於sapphire 基板上之藍光發光二極體可以被轉移至銅基板上。因具有良好的電流分佈，此大發光面積LED不需要透明電極便可以提供均勻的發光圖形。且因銅基板為良好的導電與導熱材料，此LED可以操作高至 1 安培且其光輸出功率呈線性增加。以在晶圓上(未切割及封裝)量測方式，此LED 在 1 安培輸入電流的操作下，光輸出功率為 240 mW。

而當單一發光二極體的面積增大並於高電流操作時，則需要考慮電流聚集效應(current crowding)對於元件光電特性之影響。依實驗結果得到的電流擴散長度為 $400 \text{ }\mu\text{m}$ ，我們針對銅基板上的大發光面積 LED 設計了不同的電極圖形以研究電極圖形對於元件特性之影響。實驗結果顯示，設計良好的電極圖形可以提供均勻的電流分佈而讓 LED 有均勻的發光圖形。在 1 安培操作電流下，含有良好電

極圖形之 LED 的光輸出功率為含有簡單圓形電極之 LED 的 4 倍。

另一方面，我們也提出了含有上下兩介電質反射鏡之氮化鎵面射型雷射結構。利用雷射剝技術並沉積成長介電質反射鏡，我們可以製作一含有氮化鎵與氮化銦鎵(GaN/InGaN)多量子井(MQW)的面射型雷射結構。在室溫下以一雷射(波長為 355 nm)為激發光源，在光激發操作下，研究其發光特性。此氮化鎵面射型雷射的Q 系數 (quality factor) 為 518，雷射波長為 415.9 nm，雷射頻譜之半高寬為 0.25 nm。由頻譜半高寬的減小、雷射頻譜之極化率與在發光孔徑中的雷射輻射圖形等結果，明確地顯示垂直雷射的行為。此氮化鎵面射型雷射於室溫下之臨界條件為 270 nJ 且特徵溫度為 278 K，自發輻射係數約為 1×10^{-3} 。

我們也利用 Hakki-Paoli 方法量測並計算此面射型雷射之增益特性。在室溫臨界條件時，光增益為 $2.9 \times 10^3 \text{ cm}^{-1}$ 。在不同操作溫度下，我們發現越低溫時，光增益隨著注入載子數目增加而增加的速率越大。線寬增加係數 (linewidth enhancement factor) 在室溫下為 2.8，其數值隨著操作溫度降而降低，溫度為 80 K 時，線寬增加係數為 0.6。

此外，我們也觀察到當激發光源的能量增加時，在面射型雷射之發光孔徑中會有數個相對於不同輻射波長的雷射亮點。利用微螢光激發(micro-PL)方式量測發現在雷射發光孔徑中有螢光強度不均勻的現象。此一結果可以歸因於銦含量在 MQWs 中的不均勻分佈所造成。而銦含量的不均勻也造成在一個發光孔徑中所觀察到的多個雷射亮點。

最後，我們提出一個雙介電質反射鏡電激發操作氮化鎵面射型雷射的結構，並討論此電激發面射型雷射結構的製程與結果。

Fabrication and Characteristics of GaN-based Light-Emitting Diodes and Vertical-Cavity Surface-Emitting Lasers


Student: Jung-Tang Chu

Advisor: Dr. Shin-Chung Wang

Dr. Hao-Chung Kuo

Department of Photonics & Institute of Electro-Optical Engineering
National Chiao Tung University

Abstract

The logo of National Chiao Tung University is a circular emblem with a blue border. Inside the circle, there is a stylized building with the letters 'ES' on it, and a banner at the bottom with the year '1896'.

Due to the widespread applications such as indicators, back lighting, ambient lighting, display, optical storage, optical communication, etc., the GaN-based light emitting devices are widely investigated and have many remarkable breakthroughs in performance. In this study, the fabrication of GaN-based light emitting diodes (LEDs) on a metal substrate and vertical-cavity surface-emitting lasers (VCSELs) with two dielectric mirrors are demonstrated. The characteristics and performance of the LEDs and VCSELs are analysed and characterized.

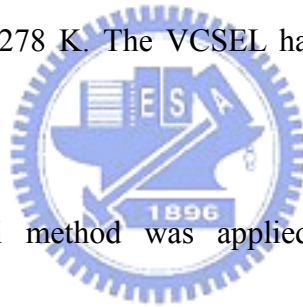
We demonstrated a large emission-area ($1 \times 1 \text{ mm}^2$) blue LEDs on copper substrate. The LEDs structure grown on sapphire substrate by metal organic chemical vapor deposition system was transferred onto a Cu substrate using bonding and laser

lift off techniques. The large emission-area LEDs showed a uniform light-emission pattern over entire defined mesa area without the transparent contact layer on the n-type GaN. The operating current of the LEDs can be driven up to 1000 mA with continuously increasing light output-power. Under wafer-level measurement, the light output-power is 240 mW with a driving current of 1000 mA.

As the area of a single LED chip is scaled up, the current crowding effect under high current operation should be considered, while the current spreading length in the LEDs on Cu is about 400 μm . For optimizing the n-electrode pattern, we observed and reported the effect of n-electrode patterns on the optical characteristics of the large emission-area. The light emitting patterns showed an obvious current crowding effect in the LEDs with a simple circular n-electrode pattern. The LEDs with well-designed n-electrode pattern showed a uniform distribution of light emission and a higher output power due to uniform current spreading. Under 1000 mA operation, the LEDs with a well-designed n-electrode showed about a 4-fold increase in the light output power over the LEDs with a simple circular n-electrode pattern.

On the other hand, we also proposed a GaN-based VCSEL structure consists of InGaN/GaN MQWs and two dielectric DBRs with high reflectivity. The GaN-based cavity including MQWs was grown on a sapphire substrate. Then the grown cavity was embedded by two dielectric DBRs and transferred onto a silica substrate.

The laser emission characteristics of a GaN-based vertical-cavity surface-emitting laser with two dielectric distributed Bragg reflectors were investigated under optically pumped operation at room temperature. The quality factor of the VCSEL is 518, indicating a good interfacial layer quality of the structure. The laser emits emission wavelength at 415.9 nm with a linewidth of 0.25 nm. The measurement results, including the linewidth reduction, degree of polarization of 70% and emission images confined inside apertures, clearly indicate a vertical lasing action. The laser has a threshold pumping energy of 270 nJ at room temperature and a characteristic temperature of 278 K. The VCSEL has a high spontaneous emission factor of about 1×10^{-3} .



Meanwhile, Hakki-Paoli method was applied to analyze the temperature dependent optical gain and linewidth enhancement factor of the VCSELs. Due to multiple cavity modes in the structure, the optical gain can be obtained by measuring the photoluminescence spectra below the threshold condition. At room temperature, the optical gain of $2.9 \times 10^3 \text{ cm}^{-1}$ was estimated at the threshold condition with a carrier density of $6.5 \times 10^{19} \text{ cm}^{-3}$. Under different ambient temperature, it is found that the gain increases more rapidly as a function of the injected carrier density at lower temperature. The linewidth enhancement factor (α -factor) shows dependence on the wavelength and was smaller at shorter wavelength. The α -factor at room temperature

was estimated as 2.8 and decreased to as low as 0.6 at 80K. The characterization of temperature dependent gain and α -factor provides further understanding in operation of the GaN-based VCSEL.

The laser emission patterns show single and multiple emission spots spatially with different emission spectra under different pumping conditions. μ -PL intensity mapping indicated that the nonuniform PL emission intensity across the VCSEL aperture. The CL and TEM images of the as-grown cavity used in the VCSEL also showed the inhomogeneity of indium composition in the InGaN/GaN MQWs. The inhomogeneous material gain distribution resulting in nonuniform PL emission could be due to the fluctuated indium composition in the MQW active layers and result in multiple emission spots in an aperture.



In the final chapter, we presented a two dielectric DBRs VCSEL structure for current injection operation. The issues of modifying the fabrication and design for the proposed VCSELs structure were also characterized and discussed.

致謝

碩士班與博士班共七年在交通大學光電工程研究所的時光裡有幸得到許多人在各方面的指導與協助。

感謝指導教授王興宗老師與郭浩中老師的指導。王老師除了在學術研究上嚴肅並認真地給予學生指導與討論之外，最令人難忘的就是王老師爽朗的笑聲與過於常人的精力。感謝王老師教導我嚴謹的研究方法與研究態度，還有授予我豐富的學識。感謝郭浩中老師的指導與鞭策，許多研究工作才得以完成。

感謝盧廷昌老師的指導與對於實驗內容及結果的討論。也特別要感謝交通大學材料所的吳耀銓教授，在架設實驗設備與實驗方法上的指導。

還要感謝同實驗室的朱振甫博士在實驗上的協助與指導，感謝林佳鋒博士、姚忻宏博士、張亞銜博士、賴芳儀博士、薛道鴻博士、黃泓文博士、高志強博士在實驗上的協助。以及實驗室歷屆的研究生與博士生們的幫助，讓我的研究得以順利進行。另外，與實驗室成員們在生活上的相處也讓我得到精神上的滿足與歡愉。

感謝我重要的家人，我的母親與三位兄長全方面的支持。

感謝研究生過程中所有曾經予以我協助的所有人，有以上諸位的協助與我個人些許的努力，此論文才得以完成。

再次感謝所有人幫助我取得博士學位並完成此論文。

Contents

Abstract (in Chinese)	I
Abstract	III
Acknowledgement	VII
Contents	VIII
List of tables	XI
List of figures	XII

Chapter 1 Introduction..... 1

1.1 GaN-based materials and light-emitting diodes..... 1

1.2 GaN-based laser diodes..... 4

1.3 An overview of the dissertation..... 6

Reference



Chapter 2 Fundamental of GaN-based light emitting device..... 14

2.1 Light emitting diodes..... 14

2.1.1 Issues involved in GaN-based LEDs on sapphire substrate..... 14

2.1.2 GaN-based LEDs on copper substrate..... 16

2.2 Vertical-cavity surface-emitting lasers..... 18

2.2.1 Fundamental of VCSELs..... 18

2.2.2 Obstacles in achieving a GaN-based VCSEL..... 19

2.2.3 GaN-based VCSELs with two dielectric mirrors..... 22

2.3 An approach: laser lift-off technique.....22

Reference

Chapter 3 Large emission-area GaN-based blue LEDs.....28

3.1 Fabrication of large emission-area vertical LEDs.....28

3.2 Characteristics of large emission-area vertical LEDs.....31

3.3 Current spreading length.....32

**3.4 Effects of different n-electrode patterns on characteristics of the large
emission-area LEDs.....33**

Reference



Chapter 4 GaN-based Vertical-Cavity Surface-Emitting Lasers.....53

4.1 Structure design and simulation.....53

4.1.1 Distributed Bragg reflector.....53

4.1.2 Resonant Cavity.....57

4.2 Fabrication of the GaN-based VCSEL with two dielectric DBRs.....59

Reference

Chapter 5 Performance and characteristics of the two dielectric DBR

GaN-VCSELs	74
5.1 Measurement setup	74
5.2 Threshold condition and spectrum evolution	74
5.3 Temperature dependent threshold	79
5.4 Temperature dependent gain characteristics	80
5.5 Effect of Indium inhomogeneity on laser characteristic	84

Reference

Chapter 6 Summary and future works.....

6.1 Summary	108
6.1.1 Large emission-area LEDs on Cu substrate	109
6.1.2 Two dielectric DBRs VCSELs	110
6.2 Future works	112

Reference

Publication list.....

119

List of tables

Chapter 3

Table 3.1 Electrical and thermal properties for several materials used in this dissertation.....42

Table 3.2 Detailed dimensions of the four electrode patterns.....47

Chapter 4

Table 4.1 Maximum reflectivity corresponding to pair numbers for $\text{SiO}_2/\text{TiO}_2$, $\text{SiO}_2/\text{Ta}_2\text{O}_5$ and GaN/AlN DBRs.....65



List of figures

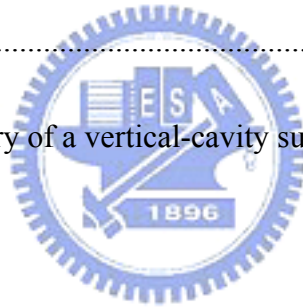
Chapter 1

Figure 1.1 Lattice constant as a function of bandgap energy of III-V nitride compounds.....8

Chapter 2

Figure 2.1 Schematic diagram of a conventional GaN-based LED on a sapphire substrate.....24

Figure 2.2 Basic geometry of a vertical-cavity surface-emitting laser.....25



Chapter 3

Figure 3.1 Schematic fabrication steps of the large-area GaN LEDs on Cu substrate.....38

Figure 3.2 Schematic diagram of the fixture for metal bonding process.....40

Figure 3.3 SEM image of the n-GaN surface after LLO process. Arrows indicate some of the Ga droplets left by the decomposition of GaN.....41

Figure 3.4 Schematic structure of the large-area emission LED on Cu.....43

Figure 3.5 SEM image of the LED on Cu substrate.....44

Figure 3.6 (a) <i>L-I-V</i> characteristics of the large-area-emission GaN LEDs on Cu substrate under continuous-wave operation. (b) Electroluminescence of the LLO-LED under a driving current of 200 mA.....	45
Figure 3.7 Normalized emission intensity as a function of the distance from the electrode edge. Inset shows the micrograph of the optical emission from the LED driven at 200 mA.....	46
Figure 3.8 The schematic diagrams top view of the LED devices with four different n-electrode patterns.....	47
Figure 3.9 <i>L-I</i> characteristics of LED <i>a</i> under <i>cw</i> and pulse operations with various duty cycles.....	48
Figure 3.10 Light emission patterns and intensity distributions of the LEDs with different n-electrode patterns.....	49
Figure 3.11 3-D isometric plot of the spatial intensity distribution of the LED <i>a</i> , LED <i>b</i> , LED <i>c</i> and LED <i>d</i> with different electrode patterns respectively.....	50
Figure 3.12 <i>L-I</i> characteristics of the LEDs with four different n-electrode patterns under <i>cw</i> operation.....	51

Chapter 4

- Figure 4.1** The transmission matrix can be determined by solving Maxwell's equation at the interfaces of layer b.....61
- Figure 4.2** Schematic of distributed Bragg reflector incorporating m pairs of two mediums with indices n_1 and n_262
- Figure 4.3** Numerically determined spectral reflectivity $R(\lambda)$ for SiO₂/TiO₂ DBRs with different number of pairs.....63
- Figure 4.4** Numerically determined spectral reflectivity $R(\lambda)$ for SiO₂/Ta₂O₅ DBRs with different number of pairs.....64
- Figure 4.5** The layer structure used for calculation of standing wave patterns. The structure was constructed according to the fabricated dielectric DBRs VCSLEs.....66
- Figure 4.6** The simulated standing wave (square of electric field) patterns inside the cavity for the dielectric DBRs VCSEL structure.....67
- Figure 4.7** PL spectrum of the as grown cavity consists of 10 pairs of 5 nm GaN barriers and 3 nm In_{0.1}Ga_{0.9}N wells.....68
- Figure 4.8** Measured spectral reflectivity of 6 pairs of SiO₂ and TiO₂ DBR and 8 pairs SiO₂/Ta₂O₅ DBR.....69
- Figure 4.9** Surface morphology and cross-sectional profile of the GaN surface

after LLO and polishing process.....70

Figure 4.10 Schematic fabrication steps of the GaN-based dielectric DBRs

VCSEL.....71

Figure 4.11 (a) A photograph of the fabricated VCSEL on a silica host substrate.

(b) Microscopic image of a fabricated 2x2 VCSEL array. The

circular areas are the locations of VCSELs with DBRs, also serving

the emission apertures.....72

Chapter 5

Figure 5.1 Schematic diagram of measurement setup for the characteristics of

the GaN-based two dielectric DBRs VCSEL.....88

Figure 5.2 Laser emission intensity obtained from the emission spectra as a

function of pumping energy at room temperature.....89

Figure 5.3 Spectral evolution of the VCSEL emission different pumping

level.....90

Figure 5.4 Spontaneous emission spectrum below threshold condition shows

multiple cavity modes.....91

Figure 5.5 Laser emission intensity as a function of normalized pumping

intensity in logarithmic scale.....92

Figure 5.6 2-D contour plot (a) and 3-D isometric plot of the spatial intensity distribution of the laser beam from the VCSEL.....	93
Figure 5.7 The angle dependent laser intensity.....	94
Figure 5.8 Temperature dependence of the lasing threshold of the VCSEL.....	95
Figure 5.9 Normalized photoluminescence spectra of the GaN-based VCSEL under different pumping power levels at 300K.....	96
Figure 5.10 Gain spectra of the VCSEL under different pumping power levels at 300K.....	97
Figure 5.11 Pumping carrier density dependence of the peak gain of the lasing mode (at ~420 nm) for different measurement temperature.....	98
Figure 5.12 The g_0 factor as a function of temperature.....	99
Figure 5.13 Calculated α -factors as a function of wavelength for different measurement temperature.....	100
Figure 5.14 Emission pattern of the VCSEL at pumping energies of (a) $1.15E_{th}$ with single laser emission spot and (b) $1.2E_{th}$ with two laser emission spots. The arrows indicate the position of the first and second emission spots. (c) Spectra of the first emission spot and second emission spot at pumping energies of $1.15E_{th}$ and $1.2E_{th}$, respectively.....	101

Figure 5.15 (a) Micro-PL intensity mapping image of the VCSEL aperture. (b) Fine micro-PL scan inside the square area in (a).....	102
Figure 5.16 PL spectra of bright point (A) and dark point (B) areas.....	103
Figure 5.17 Monochromatic CL map of the as-grown InGaN MQWs sample at 410 nm.....	104
Figure 5.18 TEM image of the as-grown MQWs used in the VCSELs cavity.....	105

Chapter 6

Figure 6.1 Schematic diagram of the two dielectric DBRs VCSEL structure for electrical driving.....	115
Figure 6.2 SEM image of the two dielectric DBRs VCSEL structure.....	116
Figure 6.3 Emission images of the two dielectric VCSEL structure operated under different injection current.....	117

Chapter 1 Introduction

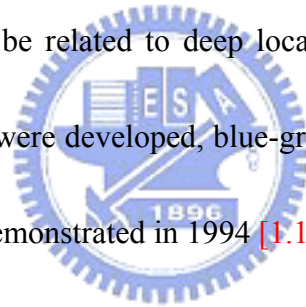
After the single-crystalline gallium nitride bulks were demonstrated in late 1960s [1.1], the development of III–V nitride compound have induced much advertence and have great progress. GaN based-compound with wide band gap and possible emission wavelength ranging from red to ultra-violet make it a compelling material system for light emitting devices application. GaN-based shot-wavelength devices, such as blue light-emitting diodes (LEDs) and laser diodes (LDs), are required for a number of applications, including solid-state lighting, full-color electroluminescent displays, laser printers, read-write laser sources for high-density information storage on magnetic and optical media, and sources for short-distance optical communications. The solid-state lighting is the most high-profile and desired application of the GaN-based materials due to the high luminaire efficiency, reliability and durability of the semiconductor light-emitting devices.

1.1 GaN-based materials and light-emitting diodes

III-V nitride-based semiconductors have a direct band gap that is suitable for blue light-emitting devices. The bandgap energy of aluminum gallium indium nitride (AlGaInN) varies between 6.2 and 1.89 eV, depending on its composition (Fig. 1.1).

Thus, red- to ultraviolet-emitting devices are possible to be fabricated by using AlGaInN. The first main progress in III–V nitride-based semiconductors was the use of AlN [1.2, 1.3] or GaN [1.4, 1.5] nucleation layers for the GaN growth. Using these nucleation layers, high-quality GaN films with a flat surface, a high mobility and a strong photoluminescence (PL) intensity could be obtained. The second important progress was realization of p-type GaN and understanding of the reason why p-type GaN had not been obtained. For the LEDs and LDs p/n layers are used to inject holes and electrons into the active layers, therefore, both p-type and n-type conductivity control are required to fabricate those devices. N-type GaN was easy to form but it was impossible to obtain p-type GaN films for a long period [1.6, 1.7]. In 1989, Amano et al [1.8] obtained p-type GaN films using Mg-doping for the acceptor impurity and a post low-energy electron-beam irradiation (LEEBI) treatment by means of metal organic chemical vapour deposition (MOCVD) growth method. After the growth, LEEBI treatment was performed for Mg-doped GaN films to obtain a low-resistivity p-type GaN film. In 1992, Nakamura et al [1.9, 1.10] obtained p-type GaN films with a resistivity of $2 \Omega\text{cm}$ [1.9] using post N_2 -ambient thermal annealing for Mg-doped GaN. The third main progress was the growth of InGaN film. InGaN is the most important compound semiconductor among III–V nitride compounds because InGaN active layers emit light by the recombination of the injected electrons

and holes in the InGaN. In 1992, Nakamura and Mukai [1.11] grew high-quality InGaN films for the first time which emitted a strong band-to-band emission from green to ultraviolet (UV) by changing the In content of InGaN using MOCVD system. Finally, an InGaN multiquantum-well (MQW) structure and confirmed an enhanced strong PL intensity from the quantized energy levels of the InGaN well layer with a thickness of 25 Å for the first time [1.12]. A small amount of indium added to the GaN is very important for obtaining a strong band-to-band emission because GaN without the indium cannot emit a strong band-to-band emission at room-temperature. This reason is considered to be related to deep localized energy states [1.13-1.17]. After these major techniques were developed, blue-green InGaN single-quantum-well (SQW) structure LEDs was demonstrated in 1994 [1.18].



Substrate is also an important issue for III-V nitride material growth. Comparing to the GaAs material system, GaN-based substrate generally have a large lattice mismatch. Sapphire has been used for GaN growth, despite the large lattice mismatch (13%; shown in Fig. 1.1). The crystal structure of GaN grown on sapphire is wurtzite. SiC is a more proper candidate for the substrate for GaN since it has small lattice mismatch for GaN. However, the cost of a SiC substrate is very expensive. Therefore, sapphire becomes a suitable and alternative substrate for GaN growth.

Hereafter, many efforts were done on improving the internal quantum efficiency

(IEQ) and light extraction efficiency (LEE) of GaN-based LEDs. Textured or roughened surface [1.20; a], substrate shaping [1.21], thin-film LED [1.22], flip-chip LED [1.23] and photonic crystal on LED [1.24] ect. were proposed to improve the light extraction efficiency. In the meanwhile, current blocking layer [1.25] and current spreading layer [1.26] in GaN-based LEDs, superlattice structure in the n-type cladding layer [1.27] and AlN/sapphire [1.28] were reported to reduce dislocation or defect and improve the light extraction efficiency.

1.2 GaN-based laser diodes

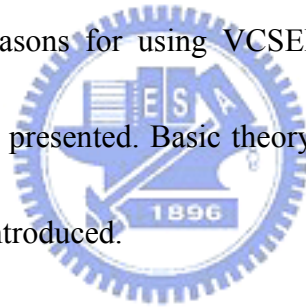
After the demonstration of InGaN QW LEDs, the RT violet edge-emitting laser (EEL) with InGaN MQW/GaN/AlGaIn-based heterostructures under pulsed operation were achieved [1.19]. After that, many groups have reported pulsed operation of EELs [1.29-1.35]. The latter results have shown that the lifetime became as long as and 10,000 hours [1.36] under RT continuous-wave (CW) operation. Also, high-power LDs were fabricated using epitaxially laterally overgrown GaN (ELOG) [1.37] and GaN substrates [1.38]. At present day (2007), the violet/blue EELs lasing at 400-410 nm with an optical output power of 200 mW have become commercial products mainly used in optical storage system [1.39].

Vertical-cavity surface-emitting lasers (VCSELs), different from edge-emitting

lasers in device structure, is another type of semiconductor lasers. The VCSEL structures, in particular with a small optical mode volume can emit a single longitudinal mode with a symmetrically circular beam and a small beam divergence that are superior than the edge emitting lasers and desirable for many practical applications in high density optical storage, laser printing, etc. In addition to the practical applications, the strong cavity field in the VCSEL microcavity can facilitate the investigation of the cavity quantum electrodynamics effect such as single photon and polariton emission, controlled spontaneous emission, and low threshold or thresholdless lasing [1.40-1.42]. The realization of GaN-based VCSEL has attracted many attention after the edge-emitting LDs were demonstrated. Several groups have reported optically pumped GaN-based VCSELs using different kinds of vertical resonant cavity structure [1.43-1.45]. Due to the obstacles of obtaining a proper reflector and fabrication process, the electrical operated GaN-based VCSELs are not achieved for a long period after the EELs were demonstrated. A breaking through of demonstrating an electrical operated GaN-VCSEL was reported by S. C. Wang *et al* [1.46].

1.3 An overview of the dissertation

Chapter 2 outlines the GaN-based light emitting devices including LEDs and VCSELs. Conventional LEDs structure grown on sapphire substrate and the issues of sapphire substrate are discussed. Laser-lift off technique for transferring a LED on sapphire to a metal substrate is described. The motivation and advantage of fabricating GaN-based thin film LEDs on metal substrates are presented. Ingredients of a laser/VCSEL structure are addressed and discussed. We discuss the obstacles of fabricating a GaN-based VCSEL and overview the three main types of proposed GaN-based VCSELs. The reasons for using VCSEL structure with two dielectric mirrors in the dissertation are presented. Basic theory of laser lift-off technique used in our work is reviewed and introduced.

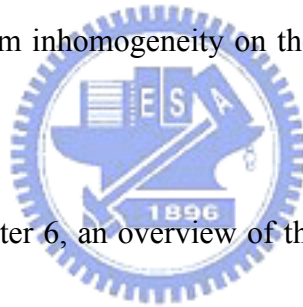


Chapter 3 presents the fabrication steps of the large emission-area GaN-based LEDs on Cu substrate. Characteristics of the LEDs are shown and studied. The current spreading length in the LEDs on Cu is measured and analysed. Effects of current crowding on the performance of the LEDs are characterized. Different patterns of n-type pads are designed to characterize the influence of current spreading length and current crowding effect on the performance of the LEDs.

Chapter 4 shows the structure and designing issues of the GaN-based VCSELs with two dielectric mirrors. The spectral reflectivity of the $\text{SiO}_2/\text{TiO}_2$ and $\text{SiO}_2/\text{Ta}_2\text{O}_5$

DBRs are calculated by transfer matrix method. The standing optical field in the resonant cavity were also simulated in order to design the epitaxial structure for obtaining a optimal optical gain. The fabrication steps of the two dielectric DBRs VCSELs are also demonstrated.

Chapter 5 shows the performance of the optically pumped GaN-based VCSELs. The threshold condition, cavity Q factor, characteristic temperature, polarization of the laser emission, gain and linewidth enhancement factor are characterized and discussed. The inhomogeneous indium composition in the InGaN/GaN MQWs are observed. Effects of the indium inhomogeneity on the characters of the VCSELs are investigated.



In the final chapter, chapter 6, an overview of this dissertation and directions of future works are given and proposed.

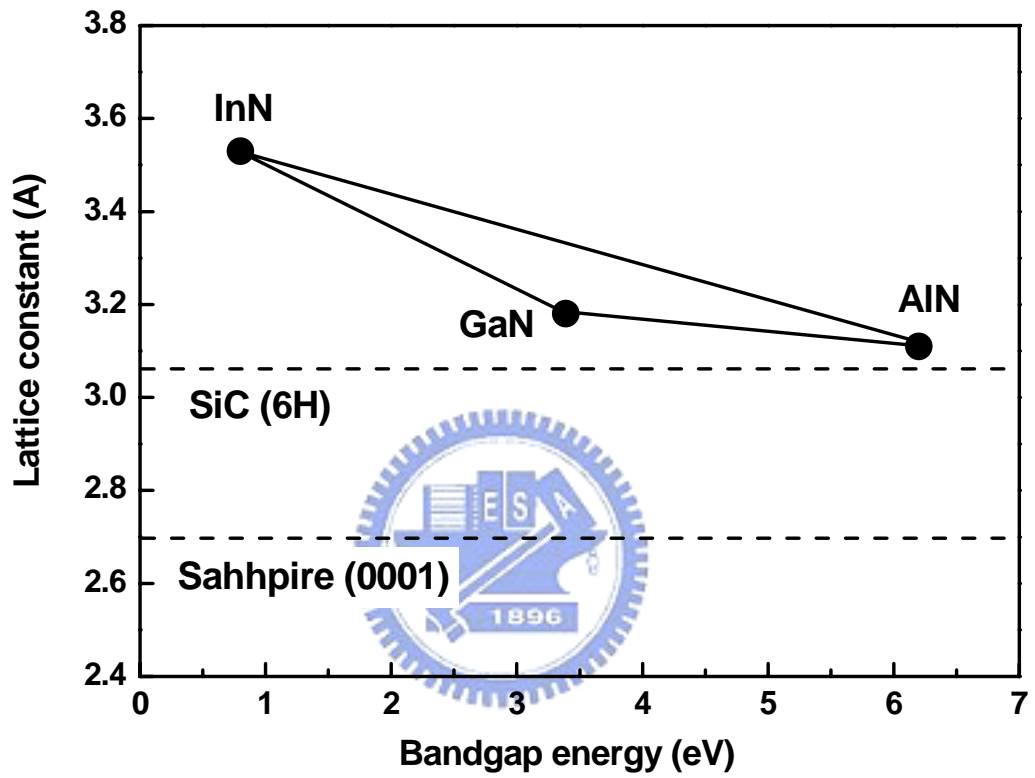


Figure 1.1 Lattice constant as a function of bandgap energy of III-V nitride compounds.

References

- [1.1] H. P. Maruska and J. J. Tietjen: Appl. Phys. Lett. **65**, 520 (1969)
- [1.2] S. Yoshida, S. Misawa and S. Gonda: Appl. Phys. Lett. **42**, 427 (1983)
- [1.3] H. Amano, N. Sawaki, I. Akasaki and T. Toyoda: Appl. Phys. Lett. **48**, 353 (1986)
- [1.4] S. Nakamura and G. Fasol: *The Blue Laser Diode* (Heidelberg: Springer, 1997)
- [1.5] S. Nakamura: Jpn. J. Appl. Phys. **30**, L1705 (1991)
- [1.6] S. Strite and H. Morko: J. Vac. Sci. Technol. B **10**, 1237 (1992)
- [1.7] F. A. Ponce and D. P. Bour: Nature **386**, 351 (1997)
- [1.8] H. Amano, M. Kito, K. Hiramatsu and I. Akasaki: Japan. J. Appl. Phys. **28**, L2112 (1989)
- [1.9] S. Nakamura, T. Mukai , M. Senoh and N. Iwasa: Japan. J. Appl. Phys. **31**, L139 (1992)
- [1.10] S. Nakamura, N. Iwasa, M. Senoh and T. Mukai: Japan. J. Appl. Phys. **31**, 1258 (1992)
- [1.11] S. Nakamura and T. Mukai: Jpn. J. Appl. Phys. **31**, L1457 (1992)
- [1.12] S. Nakamura , T. Mukai, M. Senoh, S. Nagahama and N. Iwasa: J. Appl. Phys. **74**, 3911 (1993)

- [1.13] S. Chichibu, T. Azuhata, T. Sota and S. Nakamura: Appl. Phys. Lett. **69**, 4188 (1996)
- [1.14] S. Chichibu, T. Azuhata, T. Sota and S. Nakamura: Appl. Phys. Lett. **70**, 2822 (1997)
- [1.15] Y. Narukawa, Y. Kawakami, Sz Fujita, Sg Fujita and S. Nakamura: Phys. Rev. B **55**, 1938 (1997)
- [1.16] Y. Narukawa, Y. Kawakami, M. Funato, Sz Fujita, Sg Fujita and S. Nakamura: Appl. Phys. Lett. **70**, 981 (1997)
- [1.17] S. Chichibu, K. Wada and S. Nakamura: Appl. Phys. Lett. **71**, 2346 (1997)
- [1.18] S. Nakamura, T. Mukai and M. Senoh: Appl. Phys. Lett. **64**, 1687 (1994)
- [1.19] S. Nakamura, M. Senoh, S. Nagahama, N. Iwasa, T. amada, T. Masushita, H. Kiyoku and Y. Sugimoto: Jpn. J. Appl. Phys. **35**, L74 (1996)
- [1.20] C. Huh, K. S. Lee, E. J. Kang and S. J. Park: J. Appl. Phys. **93**, 9383 (2003)
- [1.21] Compound Semiconductors 7(1), 7 (2001).
- [1.22] W. S. Wong and T. Sands: Appl. Phys. Lett. **75**, 1036 (1999)
- [1.23] J. J. Wierer, D. A. Steigerwald, M. R. Krames, J. J. O'Shea, M. J. Ludowise, G. Christenson, Y.-C. Shen, C. Lowery, P. S. Martin, S. Subramanya, W. Gotz, N. F. Gardner, R. S. Kern, and S. A. Stockman: Appl. Phys. Lett. **78**, 3379 (2001)

- [1.24] J. Shakya, K. H. Kim, J. Y. Lin and H. X. Jiang: Appl. Phys. Lett. **85**, 142 (2004)
- [1.25] C. Huh, J. M. Lee, D. J. Kim, and S. J. Park: J. of Appl. Phys. **92**, 2248 (2002)
- [1.26] J. K. Sheu, G. C. Chi, and M. J. Jou: Phot. Tech. Lett. **13**, 1164 (2001)
- [1.27] S. Nakamura, M. Senoh, S. Nagahama, N. Iwasa, T. Yamada, T. Matsushita, H. Kiyoku, Y. Sugimoto, T. Kozaki, H. Umemoto, M. Sano and K. Chocho: Appl. Phys. Lett. **72**, 211 (1998)
- [1.28] T. Egawa, H. Ohmura, H. Ishikawa and T. Jimbo: Appl. Phys. Lett. **81**, 292 (2002)
- [1.29] K. Itaya: Japan. J. Appl. Phys. **35**, L1315 (1996)
- [1.30] G. E. Bulman, K. Doverspike, S. T. Sheppard, T. W. Weeks, H. S. Kong, H. M. Dieringer, J. A. Edmond, J. D. Brown, J. T. Swindell and J. F. Schetzzena: Electron. Lett. **33**, 1556 (1997)
- [1.31] M. P. Mack, A. Abare, m. Aizcorbe, P. Kozodoy, S. Keller, U. K. Mishra, L. Coldren and S. DenBaars: 1997 MRS Internet J. Nitride Semicond. Res. 2 41 (available from <http://nsr.mij.mrs.org/2/41/>)
- [1.32] A. Kuramata, K. Domen, R. Soejima, K. Horino, S. Kubota and T. Tanahashi: Jpn. J. Appl. Phys. **36**, L1130 (1997)

- [1.33] F. Nakamura et al 1998 J. Crystal Growth 189/190 84
- [1.34] M. Kneissl, D. P. Bour, N. M. Johnson, L. T. Romano, B. S. Krusor, R. Donaldson, J. Walker and C. D. Dunnrowicz: Appl. Phys. Lett. **72**, 1539 (1998)
- [1.35] H. Katoh, T. Takeuchi, C. Anbe, R. Mizumoto, S. Yamaguchi, C. Wetzel, H. Amano, I. Akasaki, Y. Kaneko and N. Yamada: Jpn. J. Appl. Phys. **37**, L 444 (1998)
- [1.36] S. Nakamura: Japan. J. Appl. Phys. **36**, L1568 (1997)
- [1.37] S. Nakamura: Japan. J. Appl. Phys. **37**, L627 (1998)
- [1.38] S. Nakamura: Japan. J. Appl. Phys. **37**, L309 (1998)
- [1.39] <http://www.nichia.com/>
- [1.40] M. Pelton, C. Santori, J. Vuckovic, B. Zhang, G. S. Solomon, J. Plant, and Y. Yamamoto: Phys. Rev. Lett. **89**, 233602 (2002)
- [1.41] H. Deng, G. Weihs, C. Santori, J. Bloch, and Y. Yamamoto: Science **298**, 199 (2002)
- [1.42] T. Kobayashi, T. Segawa, A. Morimoto, and T. Sueta: presented at 43rd Fall Meet. Japan Society of Applied Physics, Tokyo, September, 1982
- [1.43] J. M. Redwing, D. A. S. Loeber, N. G. Anderson, M. A. Tischler, and J. S. Flynn: Appl. Phys. Lett. **69**, 1 (1996)

- [1.44] T. Someya, K. Tachibana, J. Lee, T. Kamiya, and Y. Arakawa: Jpn. J. Appl. Phys. **37**, L1424 (1998)
- [1.45] Y.-K. Song, H. Zhou, M. Diagne, I. Ozden, A. Vertikov, A. V. Nurmikko, C. Carter-Coman, R. S. Kern, F. A. Kish, and M. R. Krames: Appl. Phys. Lett. **74**, 3441 (1999)
- [1.46] T. C. Lu, C. C. Kao, H. C. Kuo, G. S. Huang, and S. C. Wang: Appl. Phys. Lett. **92**, 141102 (2008)



Chapter 2 Fundamental of GaN-based light emitting device

2.1 Light emitting diodes

2.1.1 Issues involved in GaN-based LEDs on sapphire substrate

In GaN-based materials, the choice of the substrate for epitaxial growth is a considerable issue since the lattice-matched GaN substrate is not easily available. Sapphire has been used for GaN growth, despite the large lattice mismatch (13%). The crystal structure of GaN grown on sapphire is wurtzite. SiC is a more proper candidate for the substrate for GaN since it has small lattice mismatch for GaN (3.5%). However, the cost of a SiC substrate is very expensive. Therefore, sapphire becomes a suitable and alternative substrate for GaN growth. A regular GaN-based LED grown on sapphire substrate is depicted in Fig. 2.1. A blue LED basically consisting a n-GaN layer, multiple quantum wells layer, and a p-GaN layer. Since the sapphire is an electric insulator, a part area of LED should be etched to exposure the n-GaN for depositing the n-contact metal. The transparent contact layer (TCL) used for current spreading is necessary because of the high resistivity of the p-GaN layer [2.1]. The light generated from the MQWs is emitted from the p-GaN side.

There are some notable issues in the regular GaN-based LED structures. In order to deposit n-contact metal, a part area of the LED is etched from p-GaN layer to

n-GaN layer. For a LED mesa with $350 \times 350 \mu\text{m}^2$ in area, about 10% area be etched is necessary. In other words, 10% light emission area is sacrificed. The emission light pass through the TCL will be absorbed. The typical transmittance for commonly used TCL, Ni/Au or indium tin oxide (ITO) is 85% and 90% [2.2, 2.3], respectively. The emitted light from the MQWs goes down to the sapphire side is not effectively extracted outside the LED. The refractive indices of GaN and sapphire are 2.48 and 1.78, respectively. The reflectivity of the interface of n-GaN and sapphire therefore can be estimated by the equation,

$$R = \left(\frac{n_{\text{GaN}} - n_{\text{sapphire}}}{n_{\text{GaN}} + n_{\text{sapphire}}} \right)^2$$

, the reflectivity can be estimated as about 3%. Only 3% of the downward (to the sapphire side) light is reflected upward to the p-GaN side.

As a LED is operated, the heat will be generated as the current injected into the device. For a LED on sapphire substrate, the generated heat can not be dissipated easily due to the poor thermal conductivity of sapphire (35 W/mK). The heat could increase the junction temperature of the LED, consequently saturate the light output power and degrade the reliability of the LED.

As show in Fig. 2.1, due to the p-contact and n-contact are on the same side of the sapphire substrate, the current path from p-contact to the n-contact is partly lateral. Due to this geometry, the finite resistance of the n-type material of the GaN buffer and

lower confinement layer causes the current to “crowd” near the edge of the contact [2.4-2.7]. The current crowding effect becomes noticeable especially under high injection current density operation. It has also been shown experimentally that the current crowding increases with LED aging [2.5].

2.1.2 GaN-based LEDs on copper substrate

According to the above discussed issues, a GaN-based LED on an electrically conductive substrate with high reflectivity and high thermal conductivity is desired. However, for III-V nitride material, the substrate with these features is nearly unavailable. In this study, we present a method to transfer the GaN-based LED structure grown on sapphire substrate to an electrical conductive, high-reflectivity and high-thermal conductivity host substrate and to fabricate blue LEDs on it.

The host substrate used in this study is copper (Cu). Because the Cu is electrically conductive, the n- and p-contact can be deposited on the LED and Cu substrate dividedly. The etching process for depositing the n-contact on n-GaN is not necessary and therefore the emission area of LEDs can be more used efficiently. In addition, because the p and n contacts are deposited on the different sides of the LED structure, the injected current can flow vertically through the LED structure. Vertical current flow can reduce the current crowding effect and spread the injected current uniformly

over the LED devices. The uniform current spreading is more significant for high current density operation and could scale up the dimensions of a single LED chip (above $1 \times 1 \text{ mm}^2$) for the demand of high brightness for solid lighting application.

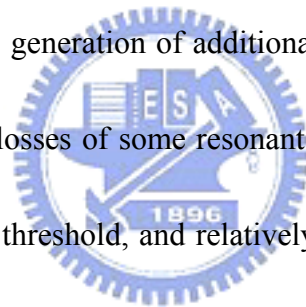
By inserting a metal layer between the LED film and the Cu substrate, the light emitted toward the metal reflector can be reflected upward to the outside of the LED. The light extraction efficiency could be improved by the reflected light. Since Cu has a high thermal conductivity value of 385 W/mK , the heat generated as operation can be dissipated more efficiently to improve the internal quantum efficiency and reliability of LEDs.



2.2 Vertical-cavity surface-emitting lasers

2.2.1 Fundamental of VCSELs

Diode lasers, like the other types of lasers, incorporate the following three ingredients. (1) *Gain medium*: The gain medium consisting of a material which normally absorbs incident radiation over some wavelength range of interest. But, if it is pumped by inputting either electrical or optical energy, the electrons within the material can be excited to the higher, nonequilibrium energy level, so that the incident radiation can be amplified rather than absorbed by stimulating the de-excitation of these electrons along with the generation of additional radiation. If the resulting gain is sufficient to overcome the losses of some resonant optical mode of the cavity, this mode is said to have reached threshold, and relatively coherent light will be emitted.

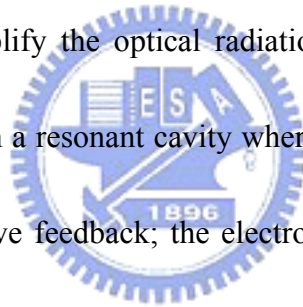


(2) *Pumping source*: Pumping source provides the energy that can excite the electrons within gain medium at lower energy level to higher energy level. It could be either optical or electrical energy. (3) *Resonant cavity*: The resonant cavity provides the necessary positive feedback for the radiation being amplified, so that a lasing oscillation can be established and sustained above threshold pumping level.

Diode lasers are distinguished from the other two types lasers (gas lasers and solid-state lasers) mainly by their ability to be pumped by an electrical current. This results in a higher efficient operation. Power conversion efficiency of ~50% is

commonly for diode lasers, whereas efficiencies for the gas and solid-state lasers are commonly 1~10%.

As depicted in Fig. 2.2, the structure of most VCSELs consist of two parallel reflectors which are distributed Bragg reflectors (DBRs) and a cavity including a multiple quantum wells (MQWs) served as active layer. The reflectivity necessary to reach the lasing threshold should normally be higher than 99.9%. The electrode pads are for injecting electrons and holes effectively into the active region is necessary for a current injection device. Corresponding to the ingredients of a laser, the active layer is the gain medium that amplify the optical radiation in the cavity; the top DBR, bottom DBRs and cavity form a resonant cavity where the radiation can interact with active region and have positive feedback; the electrode pads is for current injecting into the cavity to serve as pumping source.

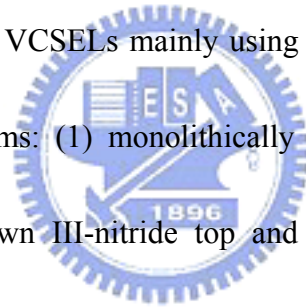


2.2.2 Obstacles in achieving a GaN-based VCSEL

In the GaN-based VCSEL structure, a micro cavity with a few λ in the optical thickness and a pair of high reflectivity (above 99%) distributed Bragg reflectors (DBRs) are necessary for reducing the lasing threshold. A difficulty in fabricating monolithically grown GaN-based VCSELs is the growth of high reflectivity epitaxial DBRs, which require a large number of AlGaIn/GaN pairs to reach a high reflectivity

owing to the small difference in refractive index (~ 0.1) between the AlGa_xN/GaN pairs.

In addition, the requirement of high reflectivity and high quality DBRs using Al_xGa_{1-x}N and GaN materials is quite formidable since these two materials have large lattice mismatch and difference in thermal expansion coefficients that tends to form cracks in the epitaxially grown DBR structure. These cracks in DBR could result in the reduction of reflectivity due to scattering, diffraction and absorption. The crystalline quality of the multiple quantum wells (MQWs) grown on the DBRs would also be degraded because of the cracks. Recently, several groups have reported optically pumped GaN-based VCSELs mainly using three different kinds of vertical resonant cavity structure forms: (1) monolithically grown vertical resonant cavity consisting of epitaxially grown III-nitride top and bottom DBRs (epitaxial DBR VCSEL), (2) vertical resonant cavity consisting of dielectric top and bottom DBR (dielectric DBR VCSEL). (3) vertical resonant cavity consists of an epitaxially grown III-nitride top DBR and a dielectric DBR (hybrid DBR VCSEL). In 1996, Redwing *et al.* proposed an all epitaxial DBR VCSEL structure consisting of a 10- μ m GaN microcavity embedded by two epitaxially grown 30-pair Al_{0.12}Ga_{0.88}N/Al_{0.4}Ga_{0.6}N DBRs [2.8]. The reflectivity of top and bottom DBR is 93% and 84%, respectively. Although the reflectivity of the DBR was not very high, a stimulated emission with a wavelength of 363 nm was observed due to the thick gain layer (10- μ m GaN). In

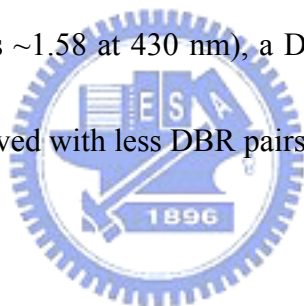


1998, Arakawa *et al.* grew an InGaN multiple quantum wells (MQWs) on 35-pair $\text{Al}_{0.34}\text{Ga}_{0.66}\text{N}/\text{GaN}$ DBR and deposited a 6-pair $\text{SiO}_2/\text{TiO}_2$ on the grown structure forming the hybrid DBR VCSEL structure [2.9]. The stimulated emission with 381 nm in wavelength and linewidth smaller than 0.1 nm were observed as the pumping power was above the threshold condition at 77 K. Cavity quality factor Q of the resonant cavity was estimated to be 165. Thereafter, in 1999, Song *et al.* demonstrated a dielectric DBR VCSEL structure consisting of InGaN MQWs and 10-pair $\text{HfO}_2/\text{SiO}_2$ top and bottom DBR using laser lift-off technology [2.10]. The reflectivity of top and bottom DBRs were 99.5% and 99.9%, respectively. The emission wavelength and linewidth of the resonant cavity tested at room temperature were 437 nm and 0.7 nm, respectively. Because of the high reflectivity DBRs, the cavity had a high Q factor of 600. In 2005, Feltin *et al.* showed that the $\text{Al}_{1-y}\text{In}_y\text{N}/\text{GaN}$ material system could be well suited to the growth of vertical cavity structures [2.11] because $\text{Al}_{1-y}\text{In}_y\text{N}$ ($y = 0.17$) was lattice-matched to GaN thus avoiding the subsequent appearance of additional structural degradation (new dislocations and/or cracks) while presenting a refractive index contrast around 7–8%, where the DBR requires over 40 pairs to reach a reflectivity of 99%. Their VCSEL structure consisted of $\text{In}_x\text{Ga}_{1-x}\text{N}/\text{GaN}$ ($x = 0.15$) MQWs and 28 (bottom)/23 (top) AlInN/GaN DBRs and exhibited a Q factor of 800. However there is so far few detailed report of the

performance characteristics of optically pumped GaN VCSELs.

2.2.3 GaN-based VCSELs with two dielectric mirrors

In this study we propose a VCSEL structure consisting two dielectric DBRs and a GaN-based resonant cavity. An epitaxially grown, thick ($\sim 4 \mu\text{m}$) GaN-based cavity incorporated with InGaN MQWs was separated from the sapphire substrate by using laser liftoff and then embedded the cavity between two dielectric DBRs. By using different dielectric materials with large difference in refractive index (for example, the difference in SiO_2 and TiO_2 is ~ 1.58 at 430 nm), a DBR with a high reflectivity and wide stop band could be achieved with less DBR pairs.



2.3 An approach: laser lift-off technique

The bonding energies of the III-V nitrides are relatively high compared to other III-V compounds. The bonding energy of GaN is high as 8.92 eV/molecule, results in the higher melting temperatures and good thermal stability of the GaN compounds compared to other compound semiconductors. Groh et al. [2.12] reported the activation energy for GaN decomposition to be 3.25 eV/atom. They also observed the presence of Ga droplets during decomposition in vacuum indicating the GaN decomposes into solid gallium and gaseous nitrogen. Sun et al. [2.13] found the

thermal decomposition of MOCVD grown GaN on r-plane sapphire occur at a temperature of 1000 °C in a hydrogen ambient. Their report indicated decomposition of the $\text{GaN} \rightarrow 2\text{Ga(l)} + \text{N}_2\text{(g)}$ will occur at a critical temperature of ~1000 °C at atmospheric pressure [2.12, 2.14].

In this dissertation, a KrF excimer laser with a wavelength of 248 nm (5 eV) was used to decompose the GaN grown on c-plane sapphire. The laser illuminated on the surface between GaN and sapphire and decomposed the GaN into Ga and N_2 , hence, the grown GaN-based LED or micro-cavity structure were transferred from the sapphire substrate to host substrate.



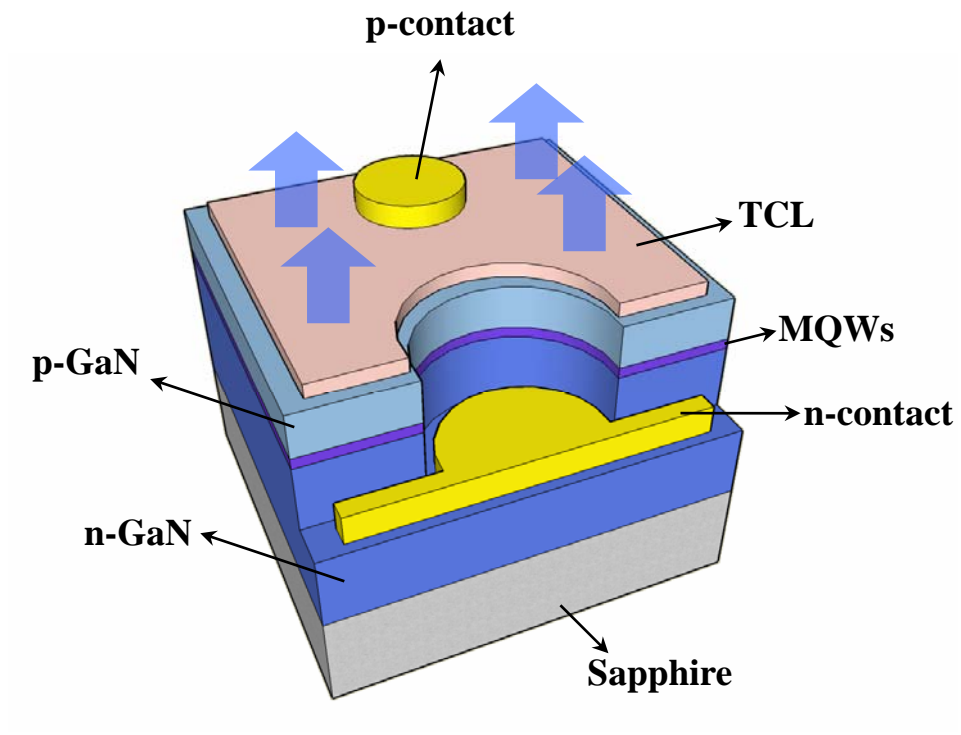


Figure 2.1 Schematic diagram of a conventional GaN-based LED on a sapphire substrate.

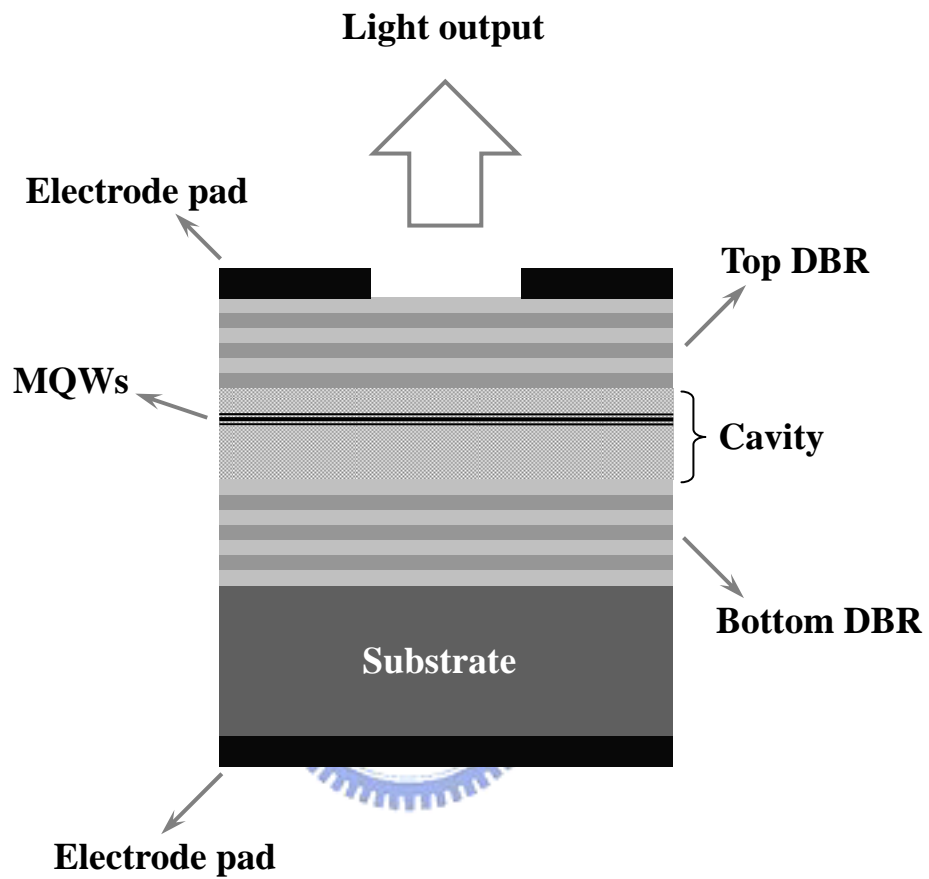


Figure 2.2 Basic geometry of a vertical-cavity surface-emitting laser.

Reference

- [2.1] S. Nakamura and G. Fahsol: *The Blue Laser Diode* (Springer, Berlin, 1997)
- [2.2] S. Y. Kim, H. W. Jang, and J. L. Lee: *Appl. Phys. Lett.* **82**, 61 (2003)
- [2.3] T. Margalith, O. Buchinsky, D. A. Cohen, A. C. Abare, M. Hansen, S. P. DenBaars, and L. A. Coldren: *Appl. Phys. Lett.* **74**, 3930 (1999)
- [2.4] X. Guo and E. F. Schubert: *J. of Appl. Phys.* **90**, 4191 (2001)
- [2.5] I. Eliashevich, Y. Li, and A. Osinsky: *Proc. SPIE* **3621**, 28 (1999)
- [2.6] G. H. B. Thompson: *Physics of Semiconductor Laser Devices* (Wiley, New York, 1980)
- [2.7] S. Fujita, M. Funato, and D. C. Park: *MRS Internet J. Nitride Semicond. Res.* **4S1**, G6.31 (1999)
- [2.8] Joan M. Redwing David A. S. Loeber and Neal G. Anderson Michael A. Tischler and Jeffrey S. Flynn: *Appl. Phys. Lett.* **69**, 1 (1996)
- [2.9] T. Someya, K. Tachibana, J. Lee, T. Kamiya and Y. Arakawa: *Jpn. J. Appl. Phys.* **37**, L1424 (1998)
- [2.10] Y.-K. Song, H. Zhou, M. Diagne, I. Ozden, A. Vertikov, A. V. Nurmikko C. Carter-Coman, R. S. Kern, F. A. Kish, and M. R. Krames: *Appl. Phys. Lett.* **74**, 3441 (1999)
- [2.11] J.-F. Carlin, J. Dorsaz, E. Feltin, R. Butté, N. Grandjean, M. Ilegems, and M. Lügt: *Appl. Phys. Lett.* **86**, 031107 (2005)
- [2.12] R. Groh, G. Gerey, L. Bartha, and J.I. Pankove: *Phys. Stat. Sol. A* **26**, 353

(1974)

[2.13] C.J. Sun, P. Kung, A. Saxler, H. Ohsato, E. Bigan, and M. Razeghi, J. Appl.

Phys.

76, 236 (1994)

[2.14] M. E. Lin, B. N. Sverdlov, and H. Morkoç: Appl. Phys. Lett. **63**, 3625

(1993)



Chapter 3 Large emission-area GaN-based blue LEDs

3.1 Fabrication of large emission-area vertical LEDs

The LED structure was grown by metalorganic chemical vapor deposition (MOCVD) on a c-plane (0001) sapphire substrate. The LED structure consists of a 3- μm -thick n-type GaN layer, a region of multiple quantum wells (MQWs) consisting of five pairs of $\text{In}_{0.25}\text{GaN}_{0.75}$ well (3nm) and GaN barrier (10nm), and a 100-nm-thick p-type GaN layer. Figures 3.1(1)-3.1(9) shows the fabrication steps of the large-area GaN LEDs with wafer bonding and laser lif-off (LLO) techniques. A SiN layer with 1 μm in thickness was deposited on the GaN LED wafer by a plasma enhanced chemical vapor deposition (PECVD) system. The SiN layer was then patterned as square mesas 1000x1000 μm^2 in size by stander lithography and dry etching process. With the SiN square mesas served as etching masks, the LED mesas were formed by etching the area without SiN masks to the sapphire substrate with an inductively coupled plasma reactive ion etching (ICP-RIE) system. After remove the SiN masks, a SiN layer (300 nm) serve as passivation layer was deposited on the LED mesas and p-GaN of the LED was explored by removing the SiN on the top of mesas. Then Ni/Au/Ni (20 nm/20 nm/250 nm) were deposited on the top of the mesas. The first two Ni/Au layers and the final Ni layer serve as contact metals for p-GaN and

bonding metal, respectively. Before bonding process, the metals-coated GaN LED was initially cleaned by surface treatment process as follow:

- (1) Cleaned by acetone (ACE) in ultrasonic bath for removing particle and/or organic contamination on sample surface;
- (2) Dipped in methanol (CH₃OH) bath for hydrophilic treatment;
- (3) Rinsed in de-ionized water (D.I. water) 3minute for surface clean;
- (4) Blowing with N₂ gas for drying.

After cleaning, the metals-coated sample and the Ni-coated Cu substrate were pre-mounted together in D.I. water to avoid particles in air. The pre-mounted sample was then blown by N₂ gas for drying and subsequently put into a fixture as depicted in

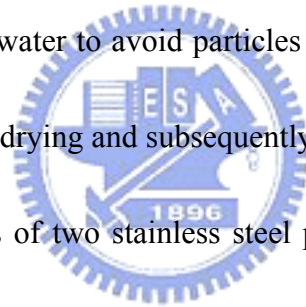


Fig. 3.2. This fixture consists of two stainless steel plates, molybdenum (Mo) screws and nuts, and high purity graphite plates. The fixture was then loaded in a stainless-steel tube chamber, which could be sealed and be filled with gaseous argon which was used to prevent oxidation of GaN and Cu samples during thermal treatment. As the chamber heated to 400 °C the compressive stress between the GaN LED and Cu substrate increased due to different thermal expansion (**Table 3.1**) between the various materials that comprise the fixture. The estimated pressure applied on the sample is on the order of few MPa/cm² by theory calculation. The exact compressive stress applied due to the difference in thermal expansion of

materials could not be determined by calculation because both the samples and the fixture underwent plastic deformation at some temperature during the process cycle [3.1]. The bonded structure was then subjected to the LLO process. A KrF excimer laser at a wavelength of 248 nm with an energy density of 400 mJ/cm^2 was used to remove the sapphire substrate. The laser with a beam size of $1.2 \text{ mm} \times 1.2 \text{ mm}$ was incident from the polished backside of the sapphire substrate onto the sapphire/GaN interface to decompose GaN into Ga and N_2 . In this process, the beam size of KrF laser was larger than that of the size of the LEDs. Therefore, the laser irradiation on the interface of sapphire and GaN was uniform. After the backside of the GaN LED structure on the sapphire substrate was decomposed by the laser beam, an n-GaN/MQW/p-GaN/Ni/Au/Ni structure was formed on the Cu substrate. After LLO process, the decomposition of GaN left Ga droplets on the surface of n-GaN as show by Fig. 3.3. Then the sample was dipped into HCl solution to remove residual Ga droplet on the n-GaN. Finally, patterned Ti/Al layers were deposited on n-GaN as an n-type contact without additional semitransparent contact layer. The final structure of the large emission area LED on Cu is depicted as Fig. 3.4.

3.2 Characteristics of large emission-area vertical LEDs

The scanning electron microscope (SEM) image of the transferred GaN LED on Cu substrate is shown in Fig. 3.5. A complete and smooth LED film without peeling or cracks was observed on the Cu substrate despite the large difference in thermal expansion coefficients of GaN ($4.4 \times 10^{-6} \text{K}^{-1}$) and Cu ($16.9 \times 10^{-6} \text{K}^{-1}$). A smooth and adhesive bonding interface was also observed. These results are essential to provide good optical and electrical characteristics of the LLO-LEDs. Figure 3.6(a) shows the light output power-current-voltage ($L-I-V$) characteristics of the large-area-emission GaN LEDs on Cu substrate under continuous-wave operation. The $L-I-V$ characteristics were measured with an on-wafer testing configuration, consisting of the Si detector mounted directly above the LED and the driving current being applied through two probes (anode and cathode). The light output power showed continuous increasing as the driving current was increased from 0 to 1000 mA. The high thermal conductivity of the Cu substrate (401 W/mK at 300 K) and the large area of the device enable high current operation without pronounced power saturation. The maximum output power is 240 mW with driving current of 1000 mA. The well behavior of $I-V$ characteristics was also observed. The voltage of the LLO-LED at 350 mA is 3.5 V. Figure 3.6(b) shows electroluminescence of the LLO-LED under a driving current of 200 mA. The peak wavelength is 456 nm and the full width at half maximum (FWHM)

is 22 nm.

3.3 Current spreading length

Because the mobility of electrons in n-GaN is higher than that of holes in p-GaN [3.3], the injected current is supposed to distribute more uniformly in p-down LLO-LEDs than that in p-up LEDs on sapphire. However, as the size of p-down LLO-LEDs are scaled up and the driving current is increased, the current spreading length in the device need to be concerned for a uniform optical emission pattern. The current spreading length is an important parameter as designing the pattern of electrode pad especially in a large area GaN-LED. The pattern of electrode should be designed by taking the current spreading length into consideration for providing a uniform current spread.

The current spreading length can be estimated since there is no transparent layer for enhancing current spread in our large-area p-down LEDs. A circular electrode with a diameter of 120 μm was deposited on the center of the $1 \times 1 \mu\text{m}^2$ p-down large-area LED. A micrograph of the optical emission from the LED driven at 200 mA is shown as the inset of Fig. 3.7. The micrograph clearly reveals that the emission intensity decreases with increasing distance from the electrode edge. The curve shows the experimental normalized intensity as a function of the distance from

the electrode edge. Since the emission intensity is proportional to the current density, the current spreading length can be defined as the distance that the emission intensity decreases to $1/e$ (about 36.8%) of the maximum intensity [3.4]. The result indicates that the current spreading length in the p-down LED is about $400\ \mu\text{m}$ under 200 mA operation. Therefore, a simple circular electrode pattern is not sufficient for providing a uniform current distribution in the large-area p-down LEDs.

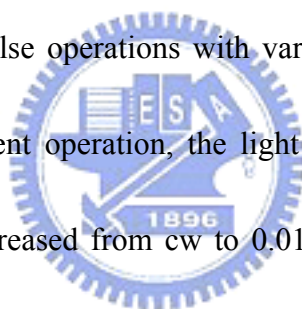
3.4 Effects of different n-electrode patterns on characteristics of large-area LEDs

In the p-side-down LLO-LED configuration, the n-GaN layer serves as a better current spreading layer than the p-GaN layer in the p-side-up configuration on a sapphire substrate due to the higher electron mobility and greater thickness of the n-GaN layer. Since the light emission intensity is directly proportional to the current density, a uniform current distribution in a n-GaN layer to provide a uniform light emission pattern is necessary. In this section, four different geometric n-electrode patterns were deposited on large-area p-side-down LLO-LEDs of $1000\times 1000\ \mu\text{m}^2$ in dimensions. The current crowding effect in the p-side-down GaN LLO-LEDs under high current injection level was observed and studied. The light emission patterns of LEDs with different n-electrode patterns are compared. The

electrode-pattern-dependent light output power is also discussed.

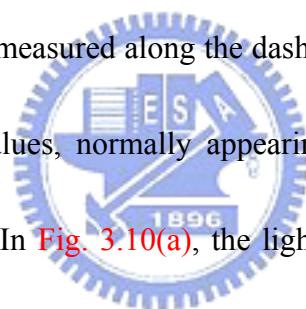
The fabrication process of the large-area p-down LEDs was same as mentioned in previous section. In the final step of deposition of n-electrode pad, Ti/Al layers with different patterns were deposited on the n-GaN layers as an n-type contact without additional transparent contact layers. The schematic top view of the LED devices with four different n-electrode patterns is shown in Fig. 3.8. The detailed dimensions of each electrode pattern are shown in Table 3.2.

In Fig. 3.9 the light output-current ($L-I$) characteristics of LED *a* under continuous-wave (*cw*) and pulse operations with various duty cycles are compared. Under the same driving current operation, the light output power increased as the operation duty cycle was decreased from *cw* to 0.01% as shown in the figure. The output power saturation is also less pronounced as the duty cycle is decreased. The inset shows the micrographic surface light emission pattern of LED *a* driven at 100 mA. The injected current crowded near the electrode, resulting in an area with a higher current density corresponding to the brighter area around the circular contact indicated by the surface light emission pattern of LED *a*. The crowded current could induce thermal and carrier over flow effects [3.4-3.7] which saturate and decrease the output power of the LEDs. The thermal effect induced by current crowded around the electrode is one reason for the power saturation of LED *a* as suggested by the $L-I$



characteristics for different operation duty cycles.

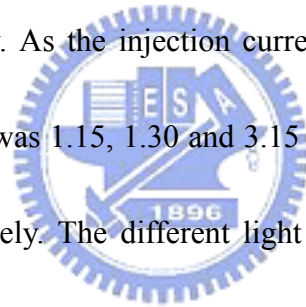
In order to reduce the current crowding effect and investigate the influence of the n-electrode pattern on optical characteristics, different n-electrode patterns were designed for the LLO-LEDs. Surface light emission patterns of the four LEDs with different n-electrode are shown in Fig. 3.10. The light emission patterns were obtained and analyzed at a driving current of 450 mA using a near-field microscope with a charge-couple device and a video analyzer (BeamView Analyzer, Coherent Inc.) linked to a computer. The solid curves at the bottom of the images stand for the relative light output intensity measured along the dashed lines. The light intensity was normalized with the peak values, normally appearing at the edges of the circular electrodes in the four LEDs. In Fig. 3.10(a), the light emission close to the circular electrode shows great intense intensity, which reveals that the injection current crowded around the electrode pad. In the absence of a transparent contact layer for current spreading, the n-electrode of LED *a* is insufficient to provide uniform current spreading in the large-area p-side-down LEDs configuration. In Fig. 3.10(b), more intense light emission around the extended cross-shaped electrode is observed. With the cross-shaped electrode for enhancement of current spreading, the distribution of light emission was more uniform compared with that of LED *a*, as shown by the relative intensity curve. The extended cross-shaped electrode improved the current



spreading over the large-area mesa and consequently provided a more uniform light emission pattern. The light emission patterns of the LEDs with two other electrodes are shown in Figs. 3.10(c) and 3.10(d). The light intensity of LED *d* showed a uniform distribution from the center to the edge of the mesa. In contrast, the light intensity of LED *c* decreased near the edge of the mesa. The light emission pattern of LED *d* is more uniform than that of LED *c*, in which a more intense emission appeared inside the square electrode. Figure 3.11 shows the 3-D isometric plot of the spatial intensity distribution of the LEDs with different electrode patterns. The isometric plots provide an intuitional observation of emission intensity distribution for these four LEDs.

The *L-I* characteristics of the LEDs with four different n-electrode patterns under cw operation are shown in Fig. 3.12. The insets show the micrographic top view of the four LEDs driven at 100 mA in the sequence LED *d*, LED *c*, LED *b*, and LED *a* from top to bottom. The output power measurement was performed from the upper side of the chip using a large-area Si photodiode placed 5 mm above the samples. The light output power of the LEDs showed a linear increase as the driving current was increased to 250 mA. The light output power of the four LEDs is also approximately equal when the driving current was below 250 mA. The injection current is supposed to spread uniformly over the mesas on the four LEDs, which results in equal light output power when the driving current was below 250 mA. As the driving current was

increased above 250 mA, the light output power of *LED a* began started to saturate and decrease due to the carrier overflow effect and the thermal effect caused by the high current density distributed around the circular electrode corresponding to the previous discussion for Fig. 3.9. In *LED b*, the output power saturation was also observed under a current injection level above 600 mA. *LED d* showed superior *L-I* characteristics compared with the other LEDs due to its well-designed electrode pattern for providing uniform current spreading as indicated in Fig. 3.10(d), which consequently reduced the thermal and carrier overflow effects caused by localized high injection current density. As the injection current was driven at 1000 mA, the light output power of *LED d* was 1.15, 1.30 and 3.15 times larger than that of *LED c*, *LED b* and *LED a*, respectively. The different light output powers among the four LEDs as the driving current increased to 1000 mA is caused by different current densities in the active region of each LED, which depend on the distribution of the injected current over the LEDs, resulting in carrier over flow and thermal effects at different levels and consequently different external quantum efficiencies [3.8]. The results indicate that the patterns of n-electrodes have a marked influence on the light output power.



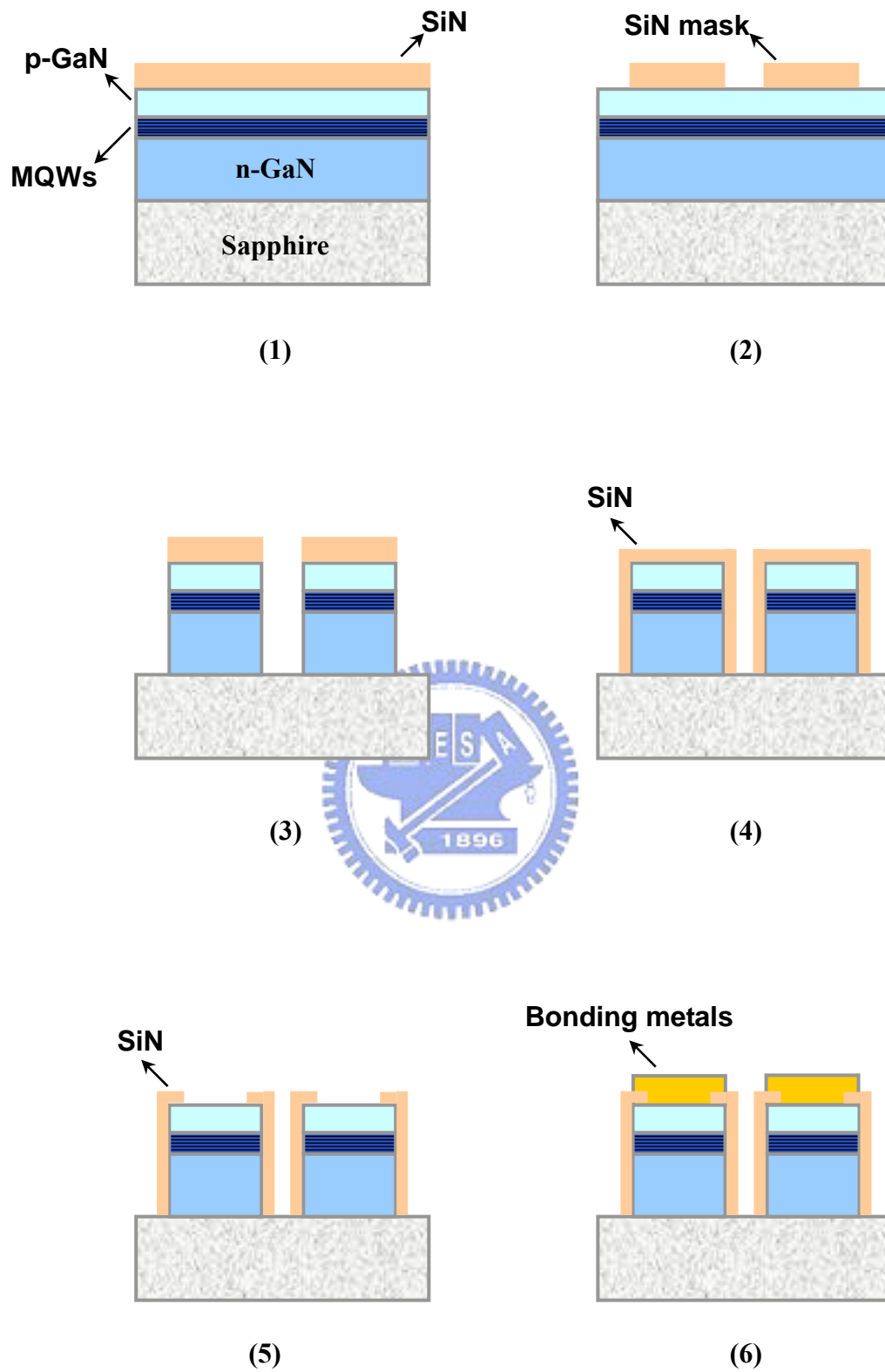


Figure 3.1 Schematic fabrication steps of the large emission-area GaN LEDs on Cu substrate.

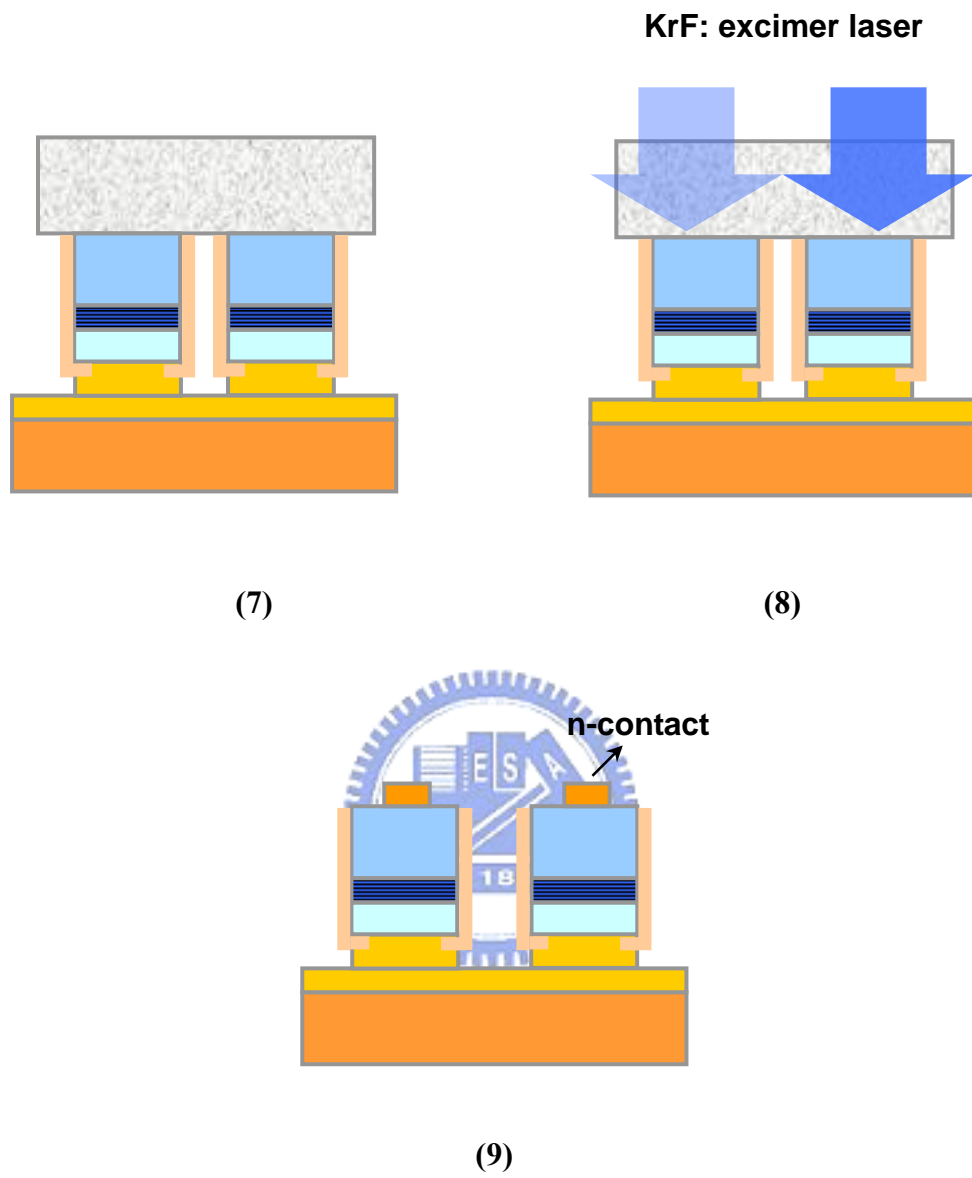


Figure 3.1 Schematic fabrication steps of the large emission-area GaN LEDs on Cu substrate.

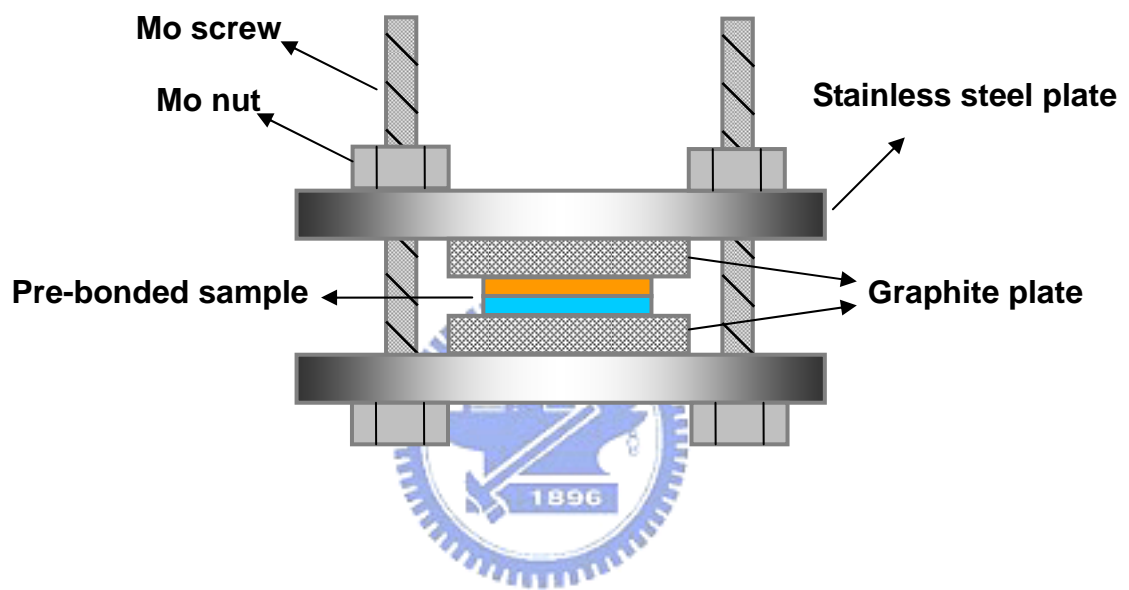


Figure 3.2 Schematic diagram of the fixture for metal bonding process.

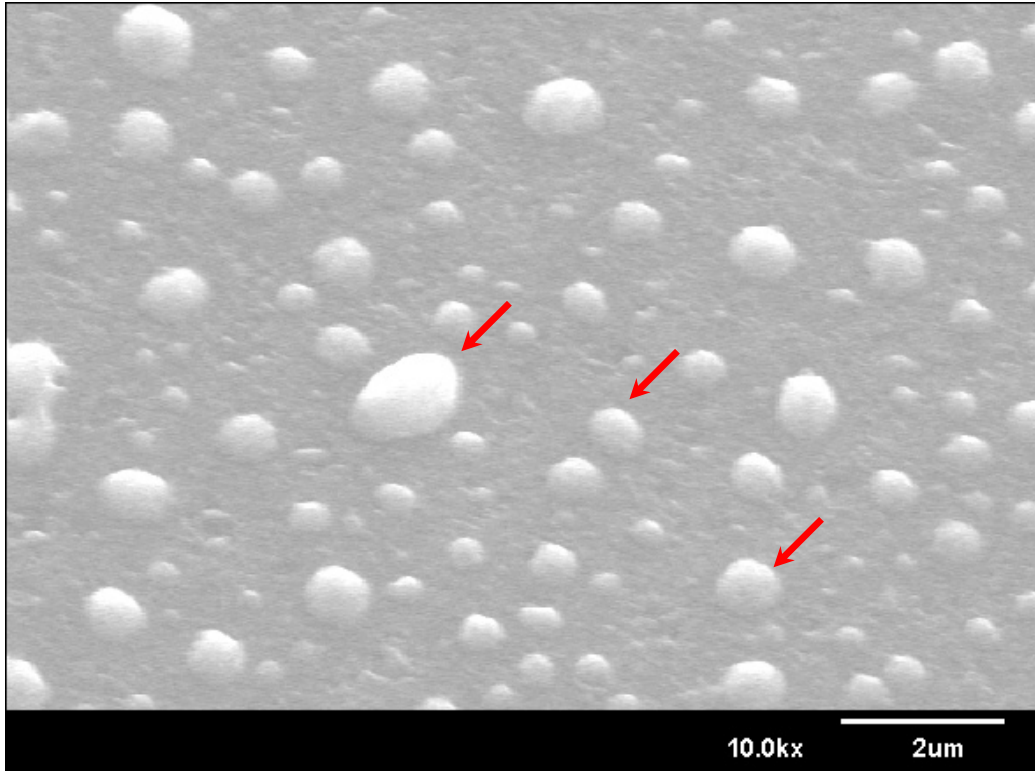


Figure 3.3 SEM image of the n-GaN surface after LLO process. Arrows indicate some Ga droplets left by the decomposition of GaN.

Table 3.1 Electrical and thermal properties for several materials used in this dissertation. (Ref. 3.2)

	Melting point (°C)	Electrical resistivity (μohm-cm)	Thermal expansion coeff. (10⁻⁶/°C)	Young's modulus (GPa)	Thermal conductivity (W/m-K)
Sapphire	2053	10 ¹¹ -10 ¹⁶ (ohm-cm)	5.0	390	35
Aluminum	660.1	4.3	23.0	70	240
Copper	1083	1.7	16.6	130	400
Gold	1063	2.2	14.2	78	297
Molybdenum	2625	5.2	4.8	329	146
Nickel	1455	6.8	12.8	214	92
Platinum	1774	10.6	9.0	168	71
Graphite	3800	2.2	6	1060	990
Steel	1400	4.5	11.8	195	16

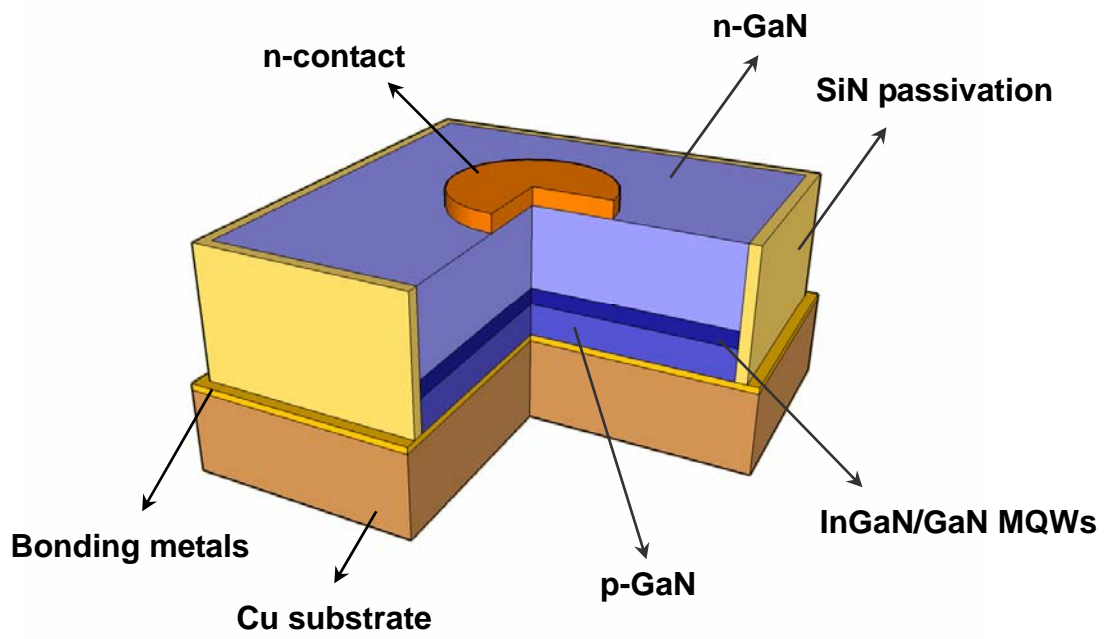


Figure 3.4 Schematic structure of the large-area emission LED on Cu.

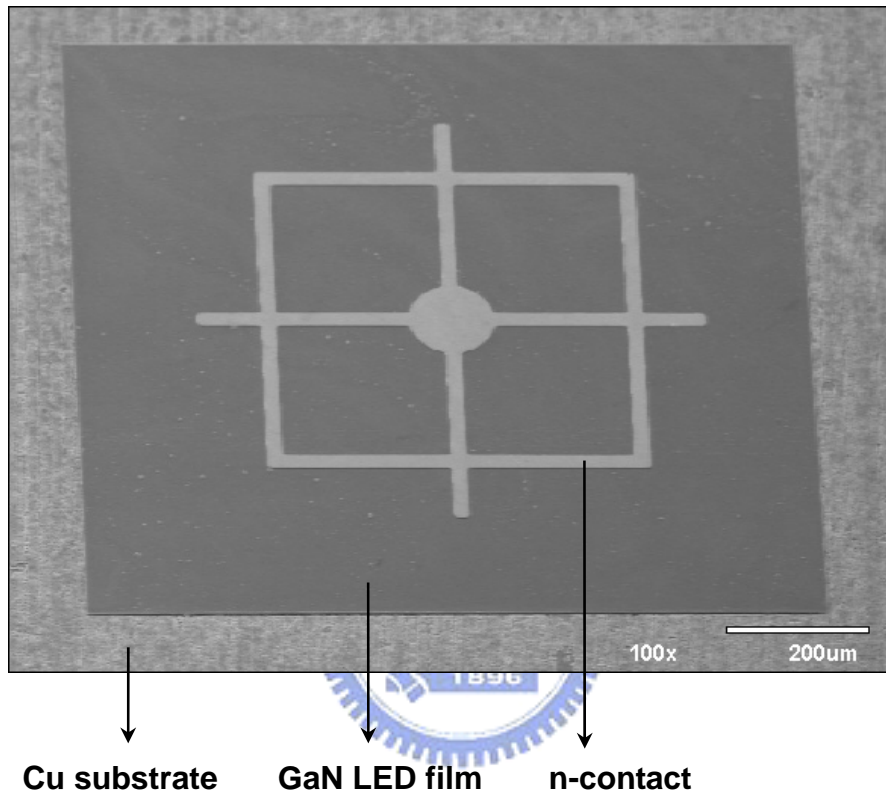


Figure 3.5 SEM image of the LED on Cu substrate.

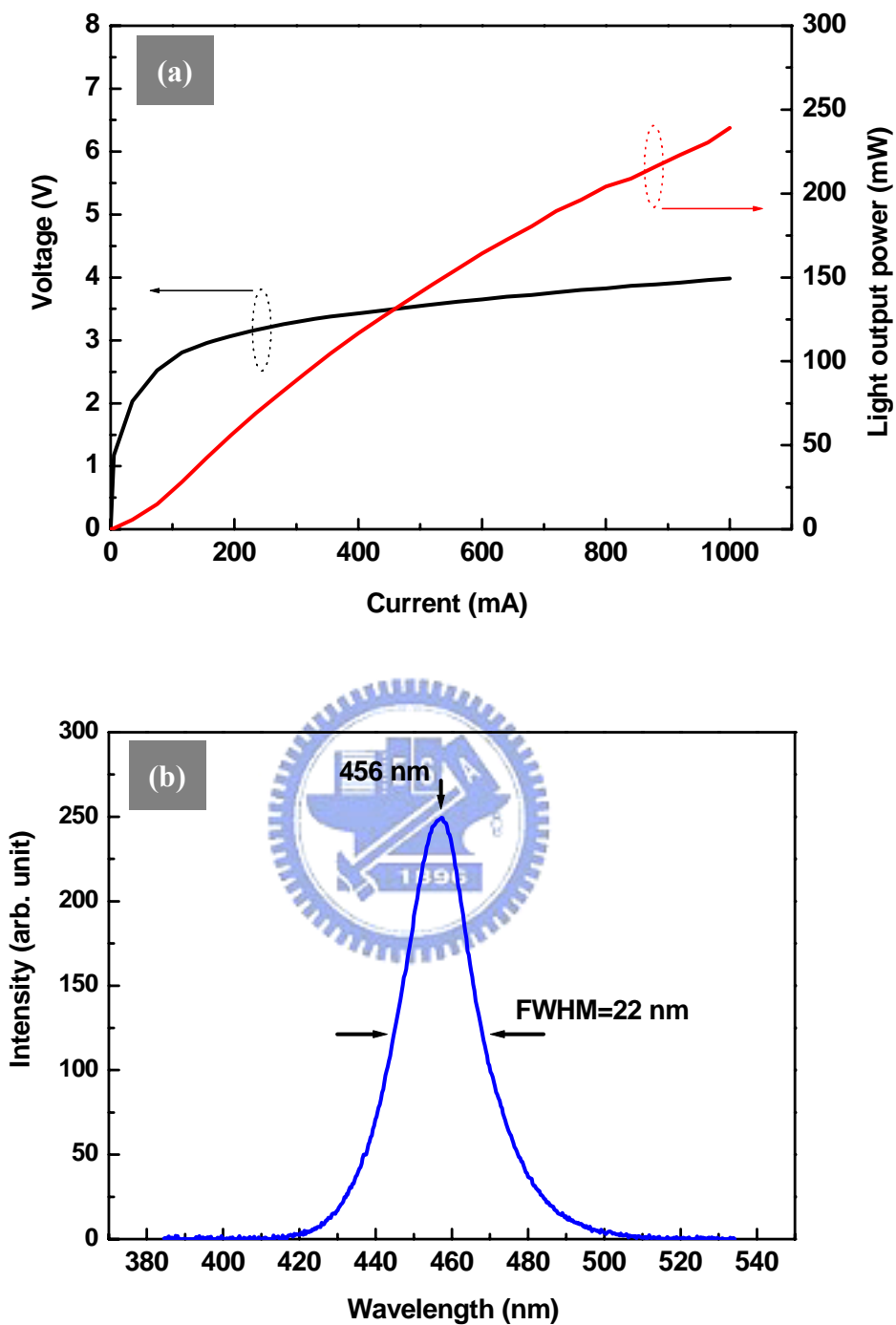


Figure 3.6 (a) $L-I-V$ characteristics of the large-area-emission GaN LEDs on Cu substrate under continuous-wave operation. (b) Electroluminescence of the LLO-LED under a driving current of 200 mA.

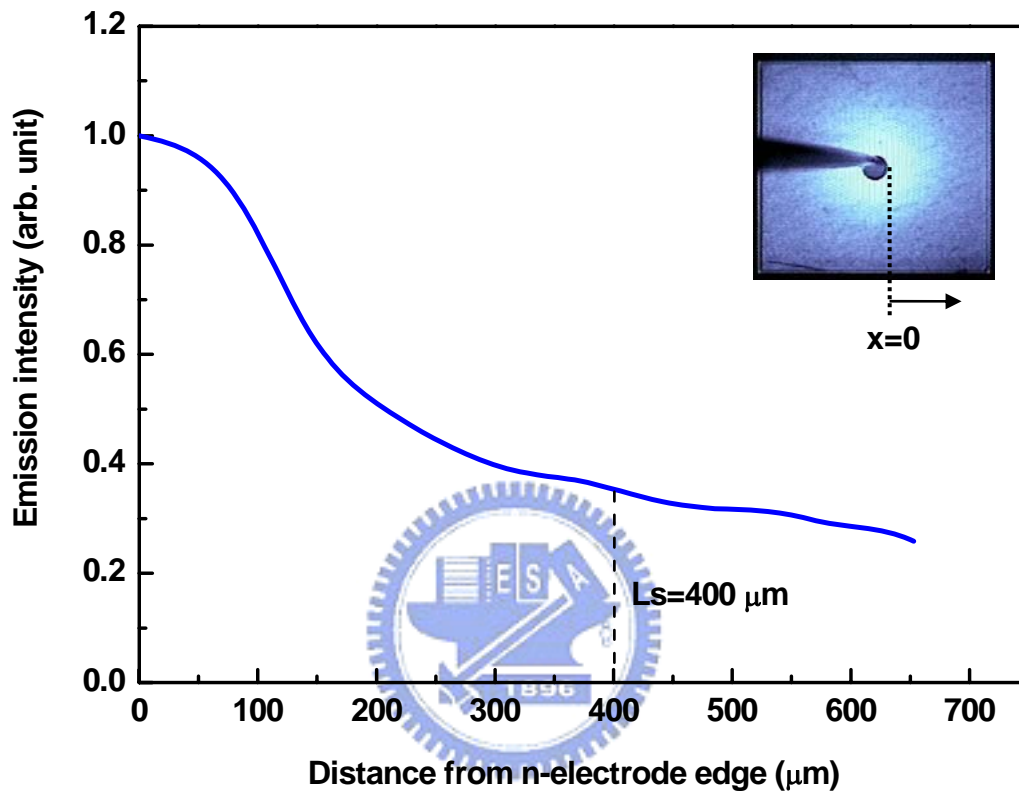


Figure 3.7 Normalized emission intensity as a function of the distance from the electrode edge. Inset shows the micrograph of the optical emission from the LED driven at 200 mA.

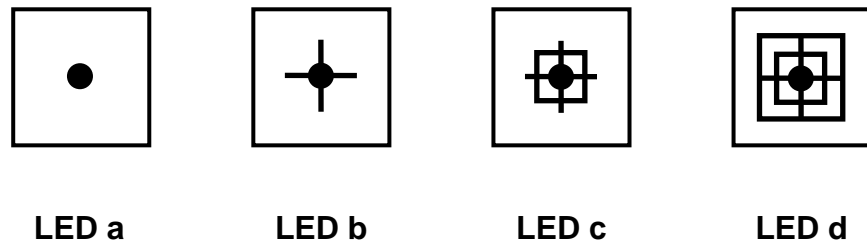






Figure 3.8 The schematic diagrams top view of the LED devices with four different n-electrode patterns.

Table 3.2 Detailed dimensions of the four electrode patterns.

Pattern	Dimension
	Diameter: 120 μm
	Length of cross: 700 μm
	Square width: 520 μm Length of cross: 700 μm
	Square width: 350 & 700 μm Cross width: 700 μm

* Circular diameter and linear linewidth are 120 μm and 20 μm , respectively in the four patterns.

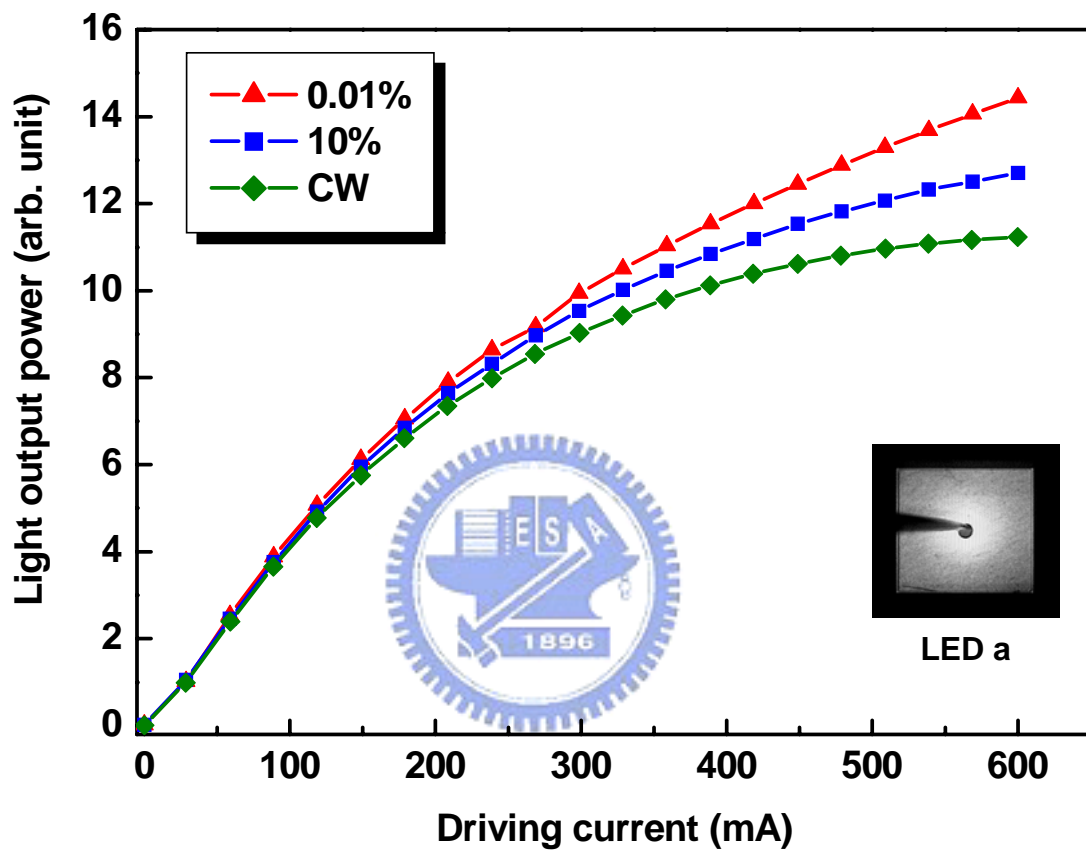


Figure 3.9 *L-I* characteristics of LED *a* under *cw* and pulse operations with various duty cycles.

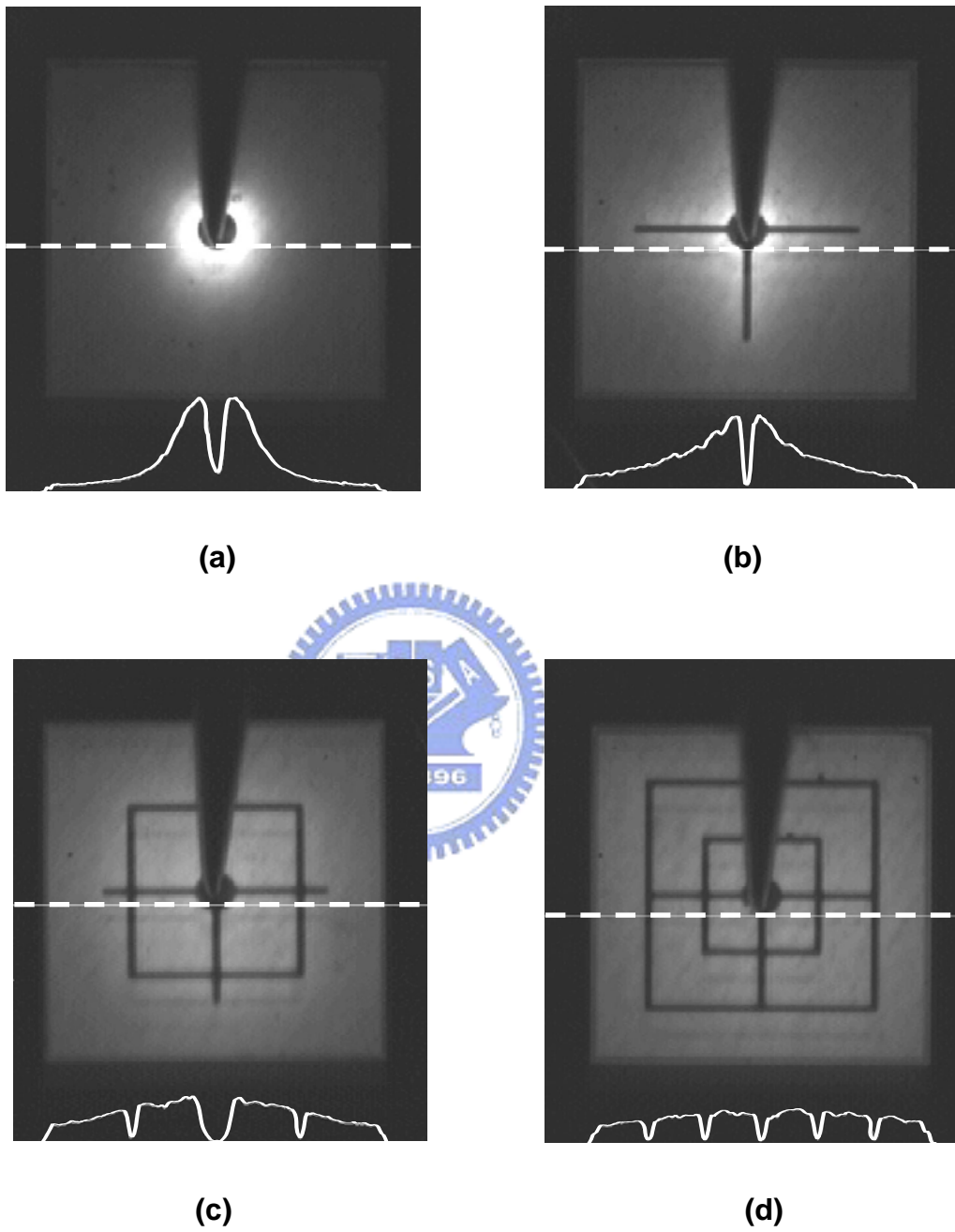


Figure 3.10 Light emission patterns and intensity distributions of the LEDs with different n-electrode patterns.

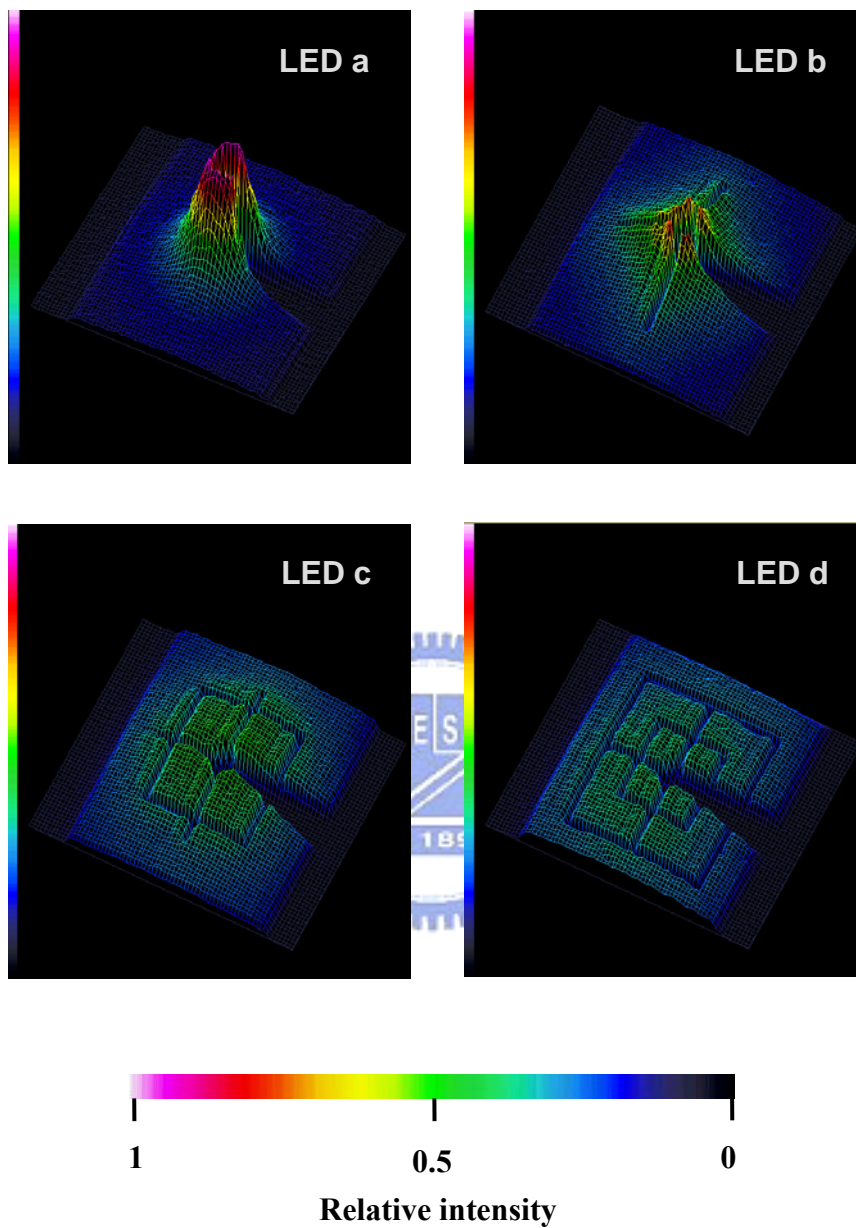


Figure 3.11 3-D isometric plot of the spatial intensity distribution of the *LED a*, *LED b*, *LED c* and *LED d* with different electrode patterns respectively.

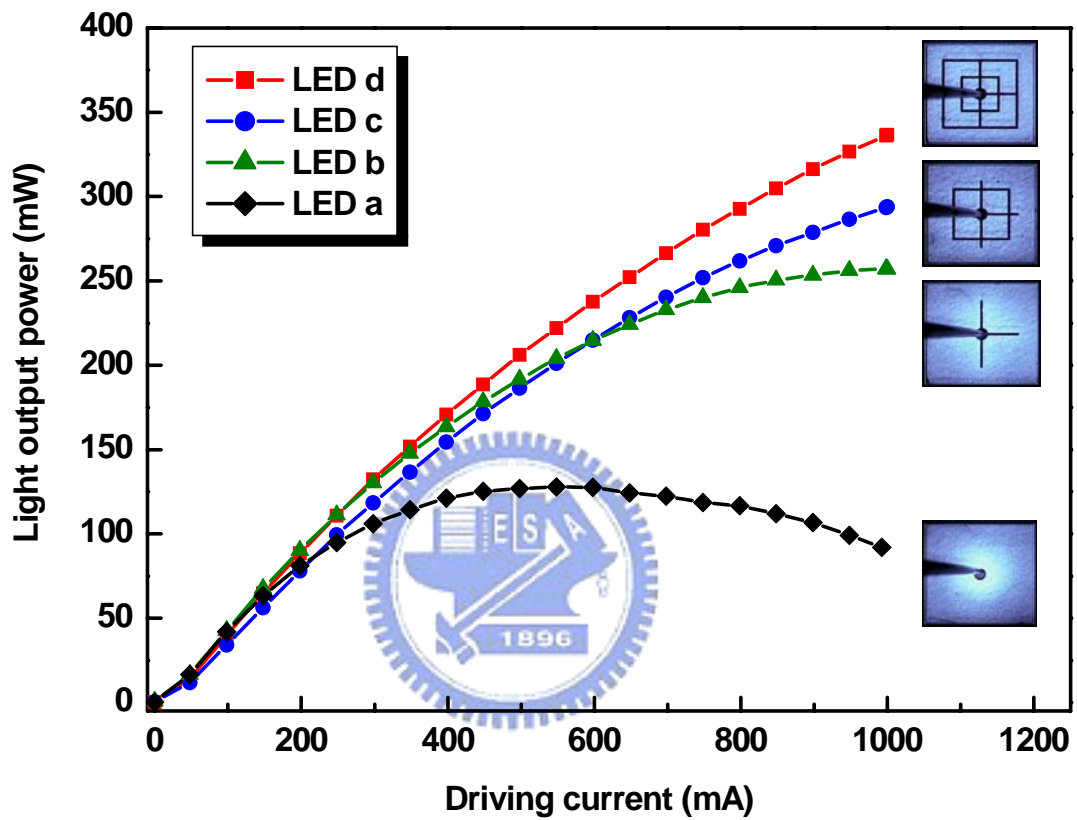


Figure 3.12 L - I characteristics of the LEDs with four different n-electrode patterns under *cw* operation.

Reference

- [3.1] Y. S. Wu, R.S. Feigelson, R. K. Route, D. Zheng, L.A. Gordon, M. M. Fejer, and R. L. Byer: *I. Electrochem. Soc.* **145**, 366 (1998)
- [3.2] N.A. Lange: *Handbook of Chemistry*, Handbook Publishers, Sandusky, Ohio, (1956)
- [3.3] S. Nakamura and G. Fahsol: *The Blue Laser Diode* (Springer, Berlin, 1997)
- [3.4] X. Guo and E. F. Schubert: *Appl. Phys. Lett.* **78**, 3337 (2001)
- [3.5] X. Guo and E. F. Schubert: *J. of Appl. Phys.*, **90**, 4191 (2001)
- [3.6] Hyunsoo Kim, Seong-Ju Park, and Hyunsang Hwang and Nae-Man Park: *Appl. Phys. Lett.* **81**, 1326 (2002)
- [3.7] Hyunsoo Kim, Jaehee Cho, Jeong Wook Lee, Sukho Yoon, Hyungkun Kim, Cheolsoo Sone, Yongjo Park and Tae-Yeon Seong: *Appl. Phys. Lett.* **90**, 063510 (2007)
- [3.8] M. Yamada, T. Mitani, Y. Narukawa, S. Shioji, I. Niki, S. Sonobe, K. Deguchi, M. Sano and T. Mukai: *Jpn. J. Appl. Phys.* **41**, L1431 (2002)

Chapter 4 GaN-based Vertical-Cavity Surface-Emitting

Lasers

4.1 Structure design and simulation

4.1.1 Distributed Bragg reflector

In order to obtain high reflectivity DBRs to reduce the threshold condition of the VCSELs, dielectric DBRs was used in the GaN-based VCSEL in this study.

Distributed Bragg reflector (DBR) consists of an alternating sequence of high and low

refractive index layers with quarter-wavelength thickness. The concept of DBR is that many small reflections at the interface between two layers can add up to a large net

reflection. At the Bragg frequency the reflections from each discontinuity add up exactly in phase. Spectral-dependent of the reflectivity can be calculated by the

transfer-matrix method [4.1]. Considering a layer of dielectric material b which is clad between two layers a and c as described by Fig. 4.1. A transverse electromagnetic

wave at normal incidence propagates through the layer in z direction. Taking the electric and magnetic (E and H) fields into consideration by Maxwell's equation, a

transmission matrix relating these fields can be written as

$$\begin{pmatrix} E(0) \\ \eta_o H(0) \end{pmatrix} = \begin{pmatrix} \cos(k_b d) & \frac{j}{n_b} \sin(k_b d) \\ j n_b \sin(k_b d) & \cos(k_b d) \end{pmatrix} \begin{pmatrix} E(d) \\ \eta_o H(d) \end{pmatrix}.$$

In the equation, n_b is the refractive index of layer b and η_o the impedance of free space,

j is the unit imaginary number, k_b is the phase propagation constant in layer b , $k_b = \frac{2\pi}{n_b \lambda}$, where λ is the wavelength in free space. Here, the absorption was not considered in this discussion. For a multilayer, a matrix M_i is formed for each layer i of thickness d_i in the stack. By considering the effect of all layers with summation length of each layers L , a matrix M relates to input and output fields ca be obtained,

$$\begin{pmatrix} E(0) \\ H(0) \end{pmatrix} = M \begin{pmatrix} E(L) \\ H(L) \end{pmatrix} \text{ and } M = \prod_i M_i = \begin{pmatrix} m_{11} & m_{12} \\ m_{21} & m_{22} \end{pmatrix}.$$

The reflection coefficient r of the stack is:

$$r = \frac{Y_o m_{11} + Y_o m_{12} - m_{21} - Y_s m_{22}}{Y_o m_{11} + Y_o m_{12} + m_{21} + Y_s m_{22}},$$

where the Y is wave admittance and o and s refer to the incident and substrate respectively. If we have a layer of index n_l between layer o and s of lower under, then the reflection from interface has a phase of π radians relative to the incident wave, because of the positive index step. If the thickness of the layer is a quarter wavelength the two reflection add in phase at the front interface due to the π round trip phase delay for the second reflection. For a stack with many alternate 1/4 wave (or $(n/2+1/4)$ wave, n integral) layers of low and high index, all interfacial reflections will add in phase.

For s Bragg reflector made from quarter wavelength layers of indices n_1 and n_2 (Fig. 4.2), the maximum reflectivity R at resonant wavelength, also denoted as Bragg wavelength (λ_B), of a stack with m non-absorbing pairs can be expressed by:

$$R = \left[\frac{1 - \frac{n_s}{n_o} \left(\frac{n_1}{n_2} \right)^{2m}}{1 + \frac{n_s}{n_o} \left(\frac{n_1}{n_2} \right)^{2m}} \right]^2.$$

The n_o and n_s in the equation are the refractive indices of incident medium and substrate, respectively and m is pair numbers of the DBR. Layer thicknesses $L_{1,2}$ have to be chosen as $L_{1,2} = \lambda_B / (4n_{1,2})$. The maximum reflectivity of a DBR therefore increases as the increasing difference in refractive indices and pair number of DBR.

SiO₂/TiO₂ and SiO₂/Ta₂O₅ DBRs were used in our GaN-based VCSELs. The difference of refractive index between SiO₂ and TiO₂ is larger than that between SiO₂ and Ta₂O₅, therefore SiO₂/TiO₂ DBR can achieve a high reflectivity with less pair than SiO₂/Ta₂O₅ DBR. Since the absorption coefficient of Ta₂O₅ for the pumping laser (NbYVO₄ laser with laser wavelength of 355 nm) is smaller than TiO₂, SiO₂/Ta₂O₅ DBR was used in order to reduce the absorption of pumping laser as the pumping laser passes through the DBR.

Figure 4.3 shows the numerically determined spectral reflectivity $R(\lambda)$ for a SiO₂/TiO₂ DBRs with different number of pairs. In the calculation the λ_B was selected to be 450 nm. The maximum reflectivity shows increasing as the number of DBR pair increase. R_{\max} are 99.87%, 99.25% and 99.73% for 5, 6 and 7 pairs, respectively. A broad spectral plateau of high reflectivity, denoted as a stop-band, appear around the Bragg wavelength, the width of which can be estimated as [4.2]

$\Delta\lambda_{sb} \approx \frac{2\lambda_B \Delta n}{\pi n_{eff}}$. For the 7 pairs SiO₂/TiO₂ DBRs, the stop-band is proportional to the

refractive index difference $\Delta n = |n_1 - n_2|$, yielding $\Delta\lambda_{sb} \sim 156$ and $n_{eff} = 1.84$ for the

effective refractive index $n_{eff} = 2 \left(\frac{1}{n_1} + \frac{1}{n_2} \right)^{-1}$. Since a high reflectivity can reduce the

threshold condition of a VCSEL, a DBR with wide stop-band is desired to cover the

emission wavelength of the MQWs. A wide stop-band provides a larger tolerance

between the designed λ_B and the main wavelength of the cooperated MQWs, this is

another important reason for us to use dielectric DBRs as mirrors in our VCSEL

structure. **Figure 4.4** shows the numerically determined spectral reflectivity for a

SiO₂/TaO₅ DBRs with different number of pairs. Due to the difference of refractive

index between SiO₂ and Ta₂O₅ is smaller than that between SiO₂ and TiO₂, 8 pairs

DBR is needed to achieve maximum reflectivity above 99%. In addition, the

stop-band of 8 pairs SiO₂/TaO₅ DBR is 120 nm which is smaller than 7 pair SiO₂/TiO₂

DBR. The maximum reflectivity corresponding to pair numbers for SiO₂/TiO₂,

SiO₂/Ta₂O₅ and GaN/AlN DBRs are shown in **Table 4.1**. The table shows that the

GaN/AlN DBR needs 15 pairs to reach a reflectivity of 99.21. Due to the lattice

mismatch between GaN and AlN, it is a difficult goal to growth a high quality and

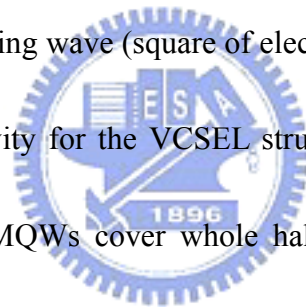
high reflectivity DBRs with such a large pair numbers. In this work, we used 6 pairs

SiO₂/TiO₂ and 8 pairs SiO₂/Ta₂O₅ DBRs in the VCSEL structure.

4.1.2 Resonant Cavity

The cavity, that is the layers between two DBRs, is another important issue need to be considered as designing a VCSEL structure. The thickness of the cavity and the position of the MQWs inside the microcavity are two key features of the VCSEL devices. Thickness of a cavity decides the resonant wavelength that will lase above threshold condition according to $L = N \frac{\lambda}{2n}$, where L is cavity length, N is an integral, λ is resonant wavelength and n is the refractive index of the cavity. Usually the resonant wavelength of the cavity is chosen to be equal to the Bragg wavelength, such that the resonant wavelength can encounter the maximum reflectivity of the DBR. Typically, the cavity length of VCSELs is on the order of few half operating wavelengths. In such a short cavity device, the electromagnetic waves would form standing wave patterns with nodes (electromagnetic wave intensity minima) and anti-nodes (electromagnetic wave intensity maxima) within the GaN microcavity. The location of the InGaN/GaN MQWs with respect to the anti-modes can significantly affect the coupling of laser mode with the cavity field. As the MQWs are well aligned with the cavity field, the more electromagnetic wave interact with the MQWs result in more photon generated in the cavity, that is optical gain of resonant mode is increased. The proper alignment of the MQWs region with the anti-nodes of the cavity standing wave field patterns will enhance the coupling and reduce laser threshold condition. As

a result, the precise layer thickness control in the VCSEL fabrication is important. In this study, we used ten pairs InGaN/GaN MQWs to form a $1/2\lambda$ optical thickness to fully overlap with one standing wave pattern in order to have a more thickness tolerance during the fabrication and to have a higher longitudinal confinement factor with respect to the total cavity length. The thickness of p-GaN is decided as 1.5λ in order to maximize the overlap between anti-node and MQWs. Figure 4.5 shows the layer structure used for calculation of standing wave patterns. The structure for simulation is constructed according to the fabricated dielectric DBRs VCSLEs. Figure 4.6 shows the simulated standing wave (square of electric field) patterns calculated by transfer matrix inside the cavity for the VCSEL structure. The numerical simulation indicates that the ten pairs MQWs cover whole half λ optical field, therefore the resonant modes in the cavity can be amplified efficiently. The thick n-type GaN layer in the structure can prevent the damage on the InGaN/GaN MQWs since the dislocation or defect might migrate into the MQWs during the laser lift-off process [4.3]. From the numerical simulation of the VCSEL structures with different p- and n-GaN thickness, we also found that the overlap between optical field and MQWs strongly depends on the thickness of p-GaN layer, but not on the thickness of the n-type GaN. In addition, since the MQW region with $1/2\lambda$ optical thickness can compensate the possible misalignment between the anti-nodes of the standing wave

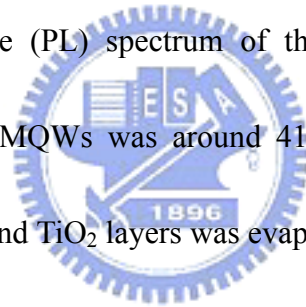


pattern and the active region position, the effect of the thickness variation of n-GaN that can not be controlled precisely during laser lift-off can be minimized.

4.2 Fabrication of the GaN-based VCSEL with two dielectric DBRs

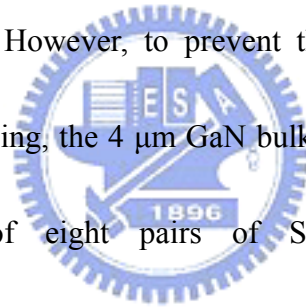
The layer structure of the GaN-based micro-cavity grown on a (0001)-oriented sapphire substrate by metalorganic chemical vapor deposition is as follows: a 30 nm nucleation layer, a 4 μm GaN bulk layer, MQWs consisting of 10 periods of 5 nm GaN barriers and 3 nm $\text{In}_{0.1}\text{Ga}_{0.9}\text{N}$ wells, and a 200 nm GaN cap layer. **Figure 4.7**

shows the photoluminescence (PL) spectrum of the as-grown sample. The peak emission wavelength of the MQWs was around 416 nm. Then, a dielectric DBR consisting of 6 pairs of SiO_2 and TiO_2 layers was evaporation-deposited on the surface



of the GaN-based cavity. In order to measure the spectral reflectivity of the deposited DBR, a glass substrate served as a monitor sample was deposited in the same deposition run. The reflectance spectrum of the $\text{SiO}_2/\text{TiO}_2$ DBR is obtained by measuring the monitor sample as shown by **Fig. 4.8**. Next, in order to enhance the adhesion between the epitaxial layers and the silica substrate, an array of disk-like patterns with a diameter of 60 μm was formed by standard photolithography and the $\text{SiO}_2/\text{TiO}_2$ DBR mesas were formed using a buffer oxide etcher. This wafer was then mounted onto a silica substrate, which is nearly transparent to the wavelengths of the

pumping laser and our VCSEL. The epitaxial layers with SiO₂/TiO₂ DBR was then separated from sapphire substrate by LLO process. After the LLO, the sample was dipped in HCl solution to remove residual Ga droplets on the exposed GaN layer. In the next step, the sample was lapped and polished using diamond powders to smooth the GaN surface since the laser lift-off process left a roughened surface. The mean surface roughness of the polished GaN surface measured by atomic force microscopy (AFM). **Figure 4.9** show the surface morphology and cross-sectional profile that scanned over an area of 10x10 μm². The image indicates the root-mean-square surface morphology is about 1 nm. However, to prevent the possible degradation of the quality of MQWs during lapping, the 4 μm GaN bulk layer was preserved. Finally, a second DBR consisting of eight pairs of SiO₂ and Ta₂O₅ layers was evaporation-deposited on the polished GaN surface. The measured reflectance spectrum of the SiO₂/Ta₂O₅ DBR is shown as **Fig. 4.8**. The fabrication process of the GaN-based dielectric DBRs VCSELs are schematically shown in **Fig. 4.10**. **Figure 4.11(a)** shows a photograph of the fabricated VCSEL on a silica host substrate. **Figure 4.11(b)** shows the microscopic image of a fabricated 2x2 VCSEL array. The circular areas are the locations of VCSELs with DBRs, also serving the emission apertures.



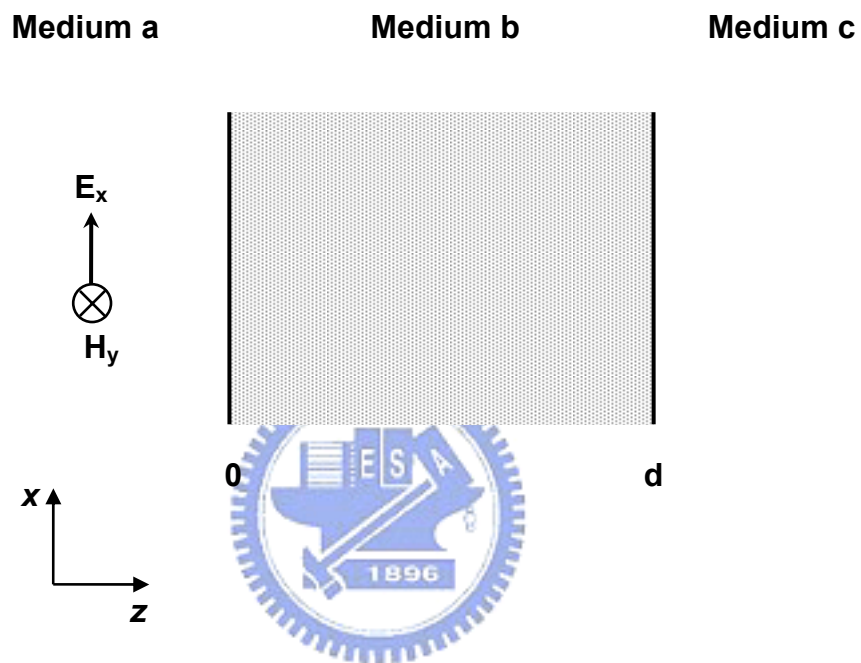


Figure 4.1 The transmission matrix can be determined by solving Maxwell's equation at the interfaces of layer b.

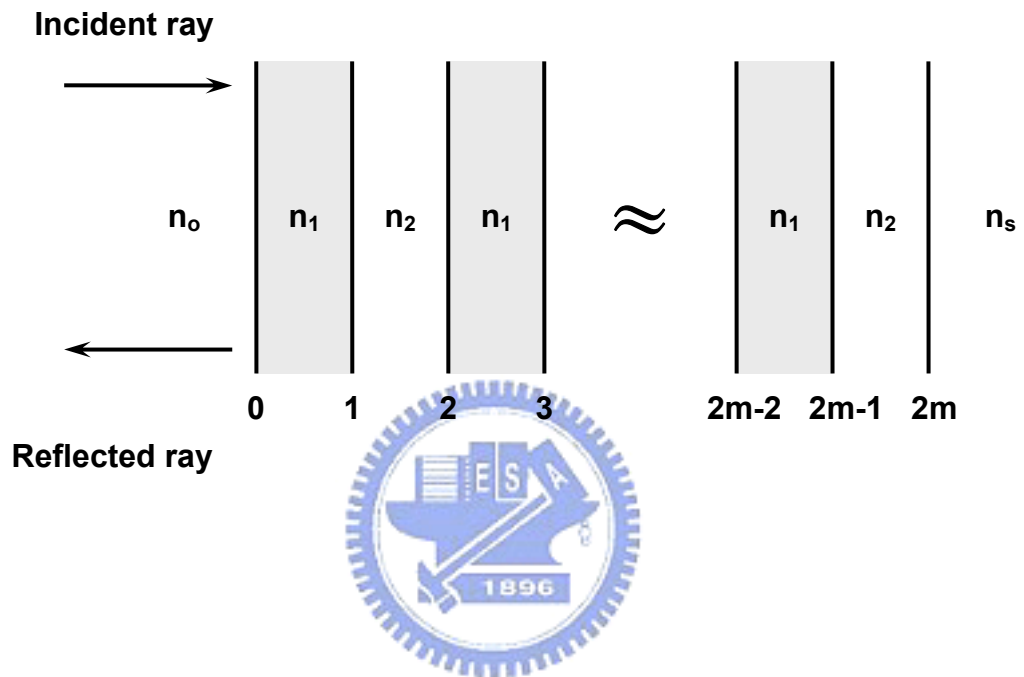


Figure 4.2 Schematic of distributed Bragg reflector incorporating m pairs of two mediums with indices n_1 and n_2 .

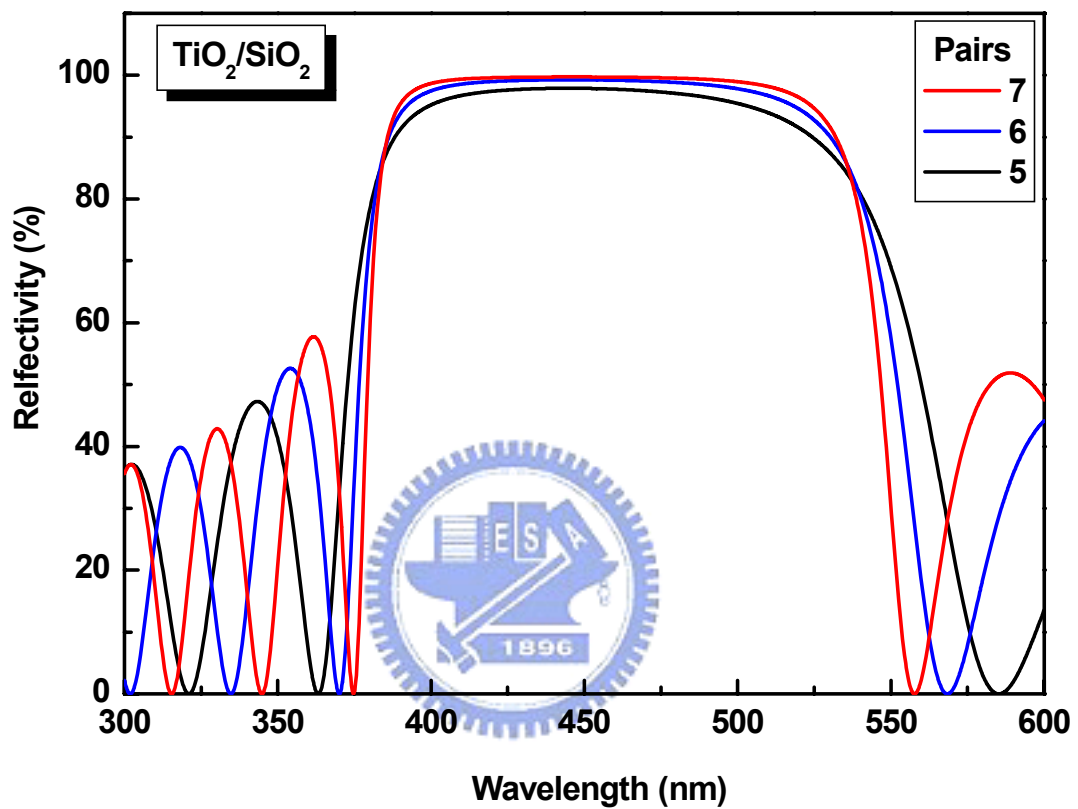


Figure 4.3 Numerically determined spectral reflectivity $R(\lambda)$ for $\text{SiO}_2/\text{TiO}_2$ DBRs with different number of pairs.

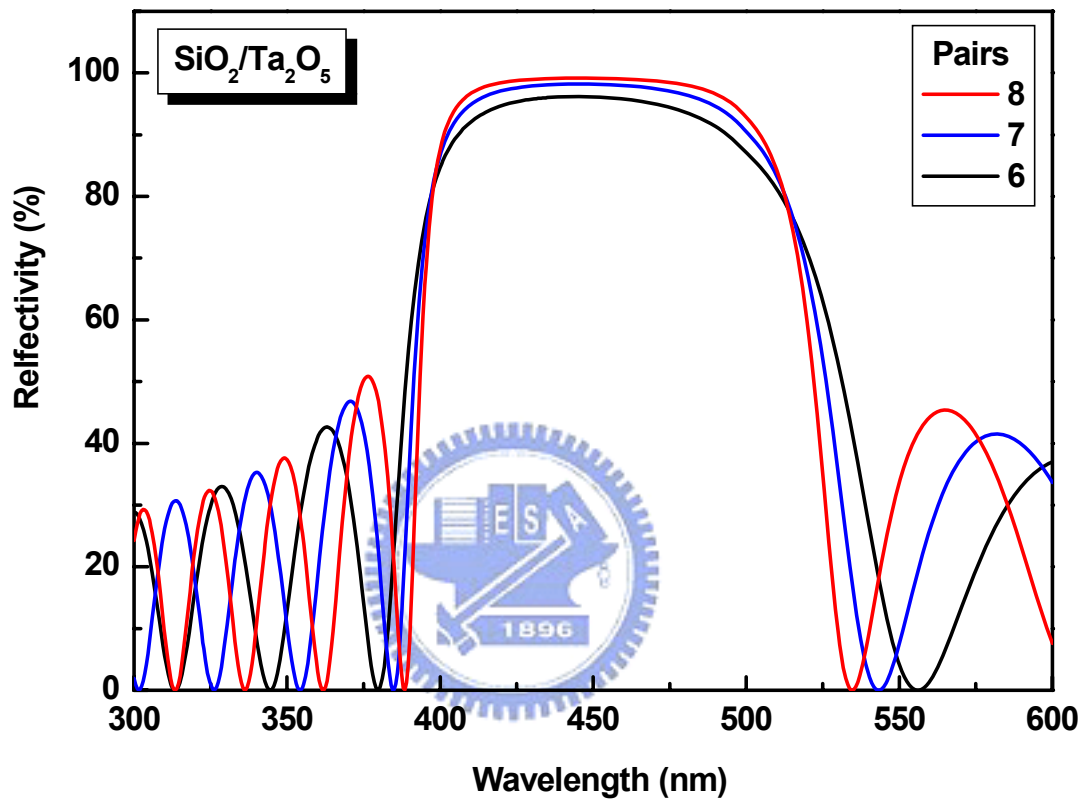


Figure 4.4 Numerically determined spectral reflectivity $R(\lambda)$ for $\text{SiO}_2/\text{Ta}_2\text{O}_5$ DBRs with different number of pairs.

Table 4.1 Maximum reflectivity corresponding to pair numbers for SiO₂/TiO₂,

SiO₂/Ta₂O₅ and GaN/AlN DBRs.

	$\Delta n/n$ (%)	Max. R (%) [number of pairs]		
TiO ₂ /SiO ₂	40	97.88 [5]	99.25 [6]	99.73 [7]
Ta ₂ O ₅ /SiO ₂	33.5	96.13 [6]	98.19 [7]	99.15 [8]
GaN/AlN	17.6	98.20 [13]	98.81 [14]	99.21 [15]
Refractive index (@ ~ 450nm)	SiO ₂ : 1.463, TiO ₂ : 2.469, Ta ₂ O ₅ : 2.2, AlN: 2.05, GaN: 2.49			

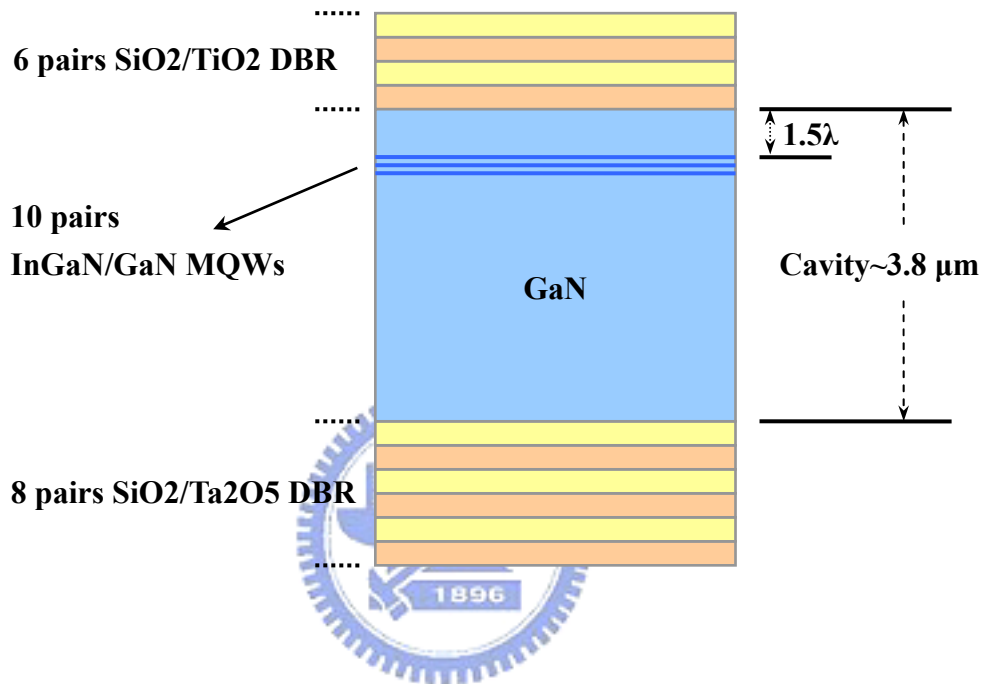


Figure 4.5 The layer structure used for calculation of standing wave patterns. The structure was constructed according to the fabricated dielectric DBRs VCSLEs.

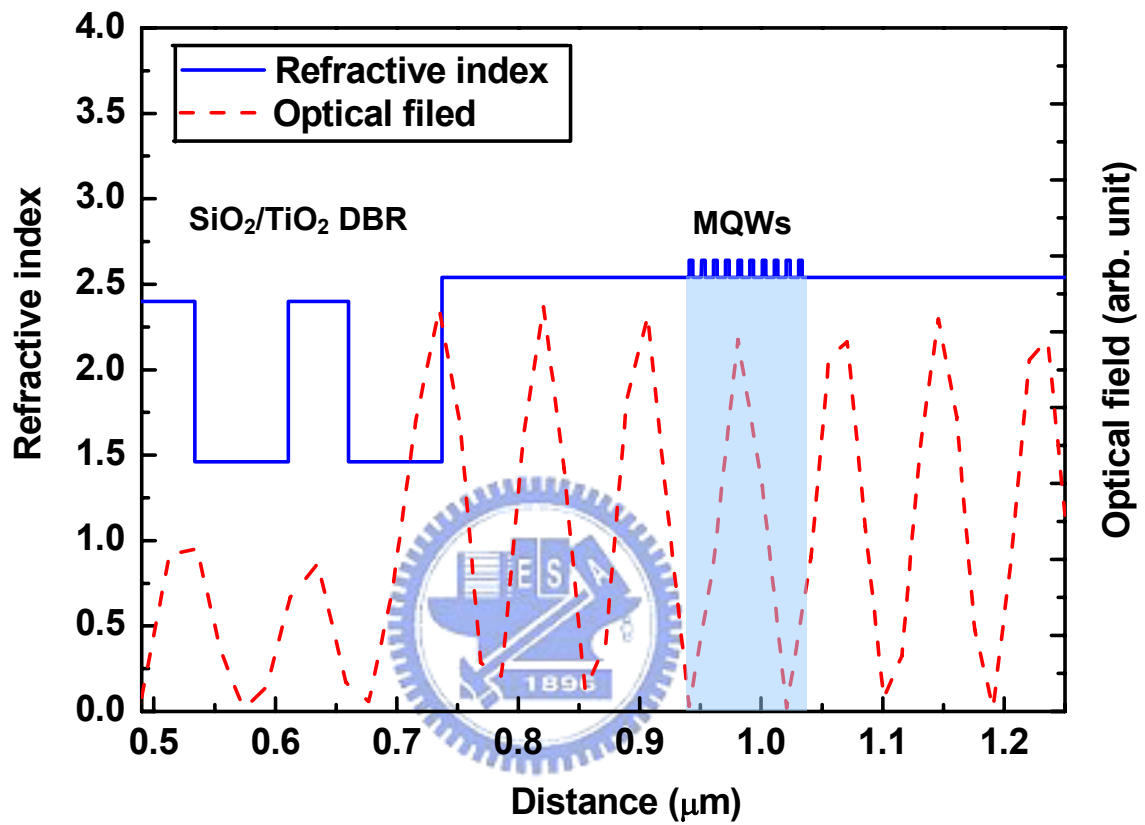


Figure 4.6 The simulated standing wave (square of electric field) patterns inside the cavity for the dielectric DBRs VCSEL structure.

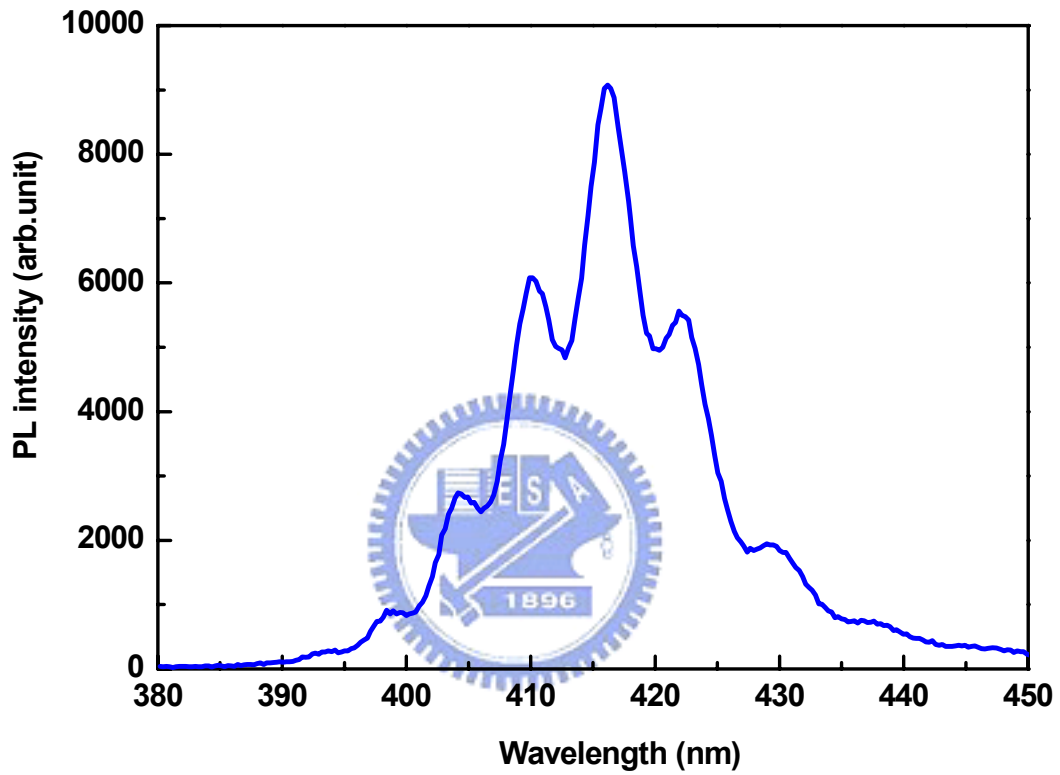


Figure 4.7 PL spectrum of the as grown cavity consists of 10 pairs of 5 nm GaN barriers and 3 nm $\text{In}_{0.1}\text{Ga}_{0.9}\text{N}$ wells.

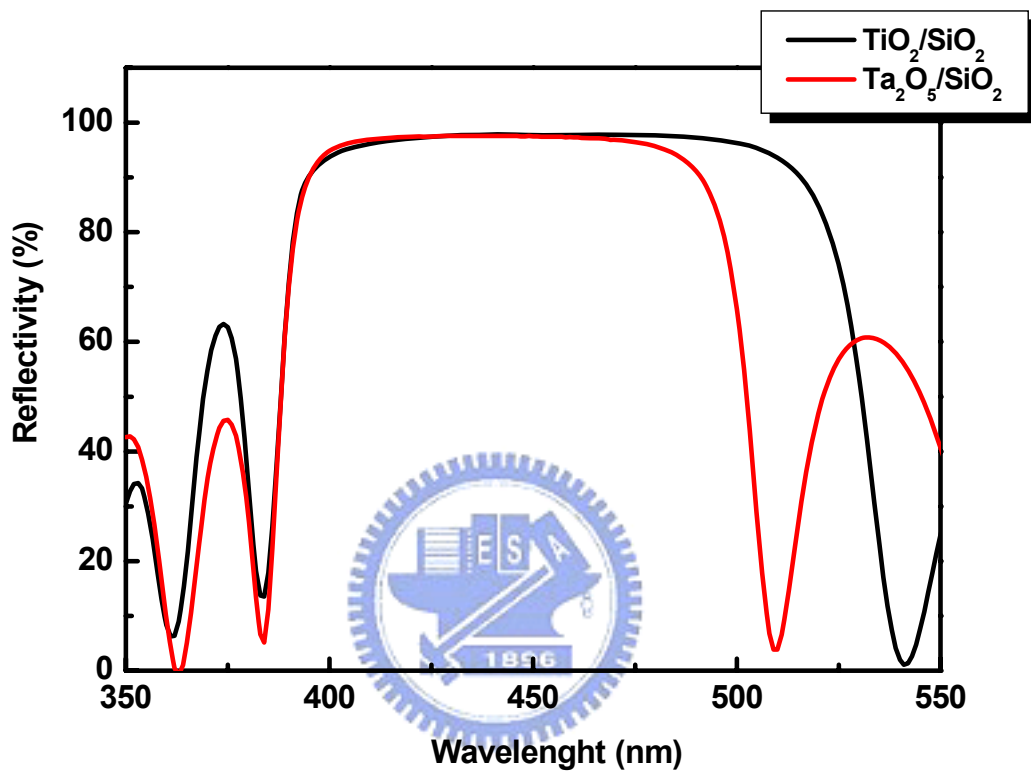


Figure 4.8 Measured spectral reflectivity of 6 pairs of SiO₂ and TiO₂ DBR and 8 pairs SiO₂/Ta₂O₅ DBR.

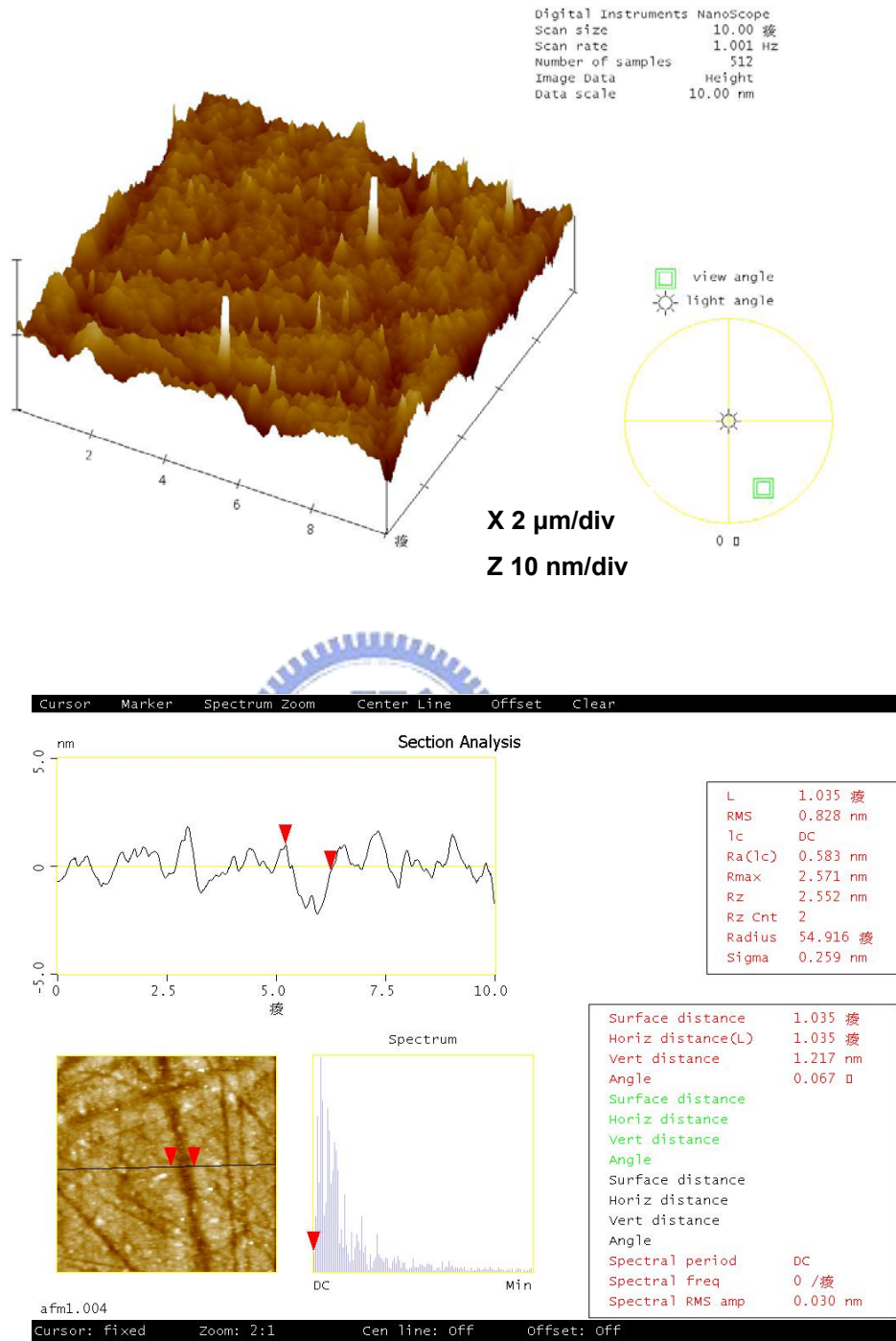


Figure 4.9 Surface morphology and cross-sectional profile of the GaN surface after LLO and polishing process.

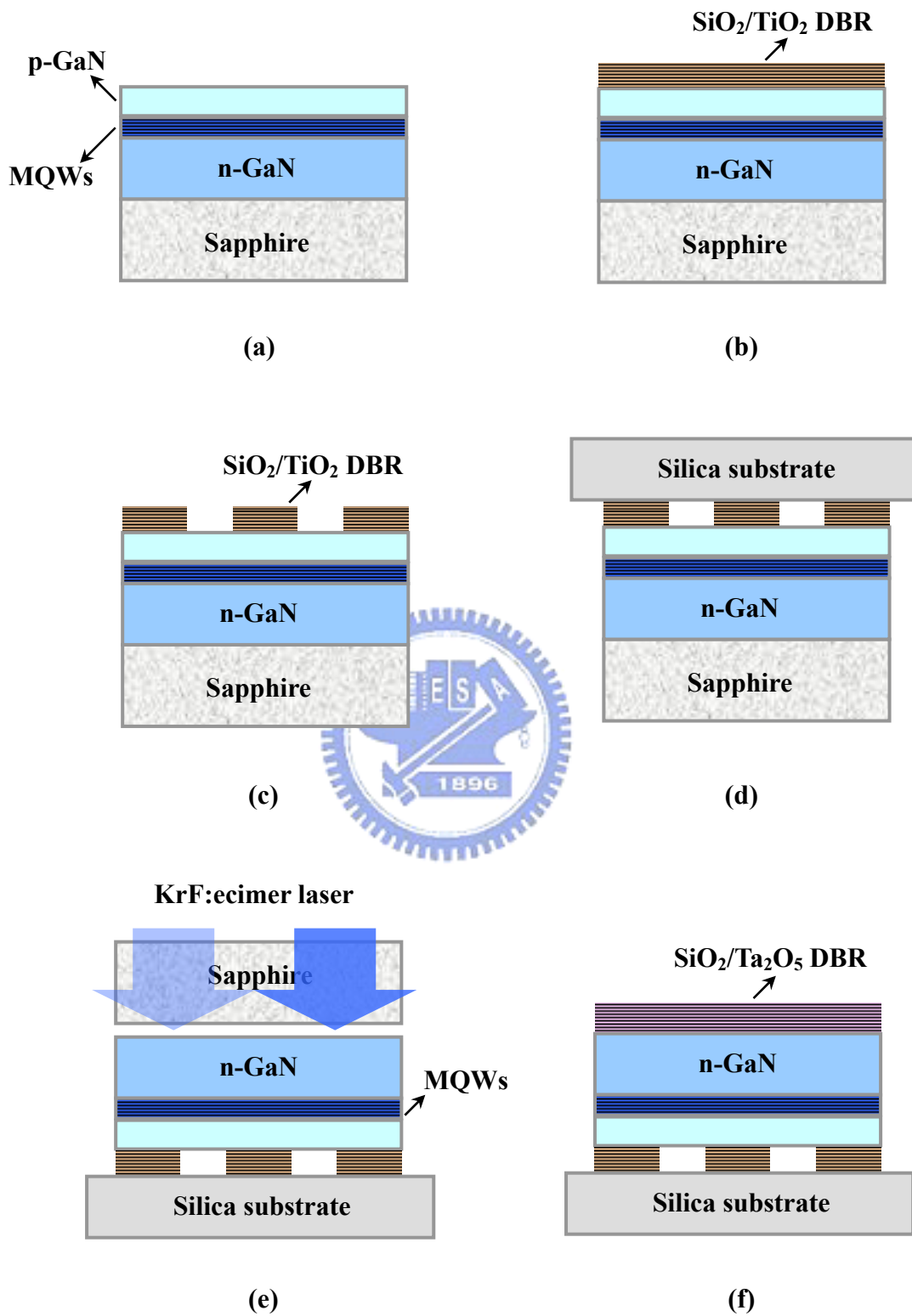
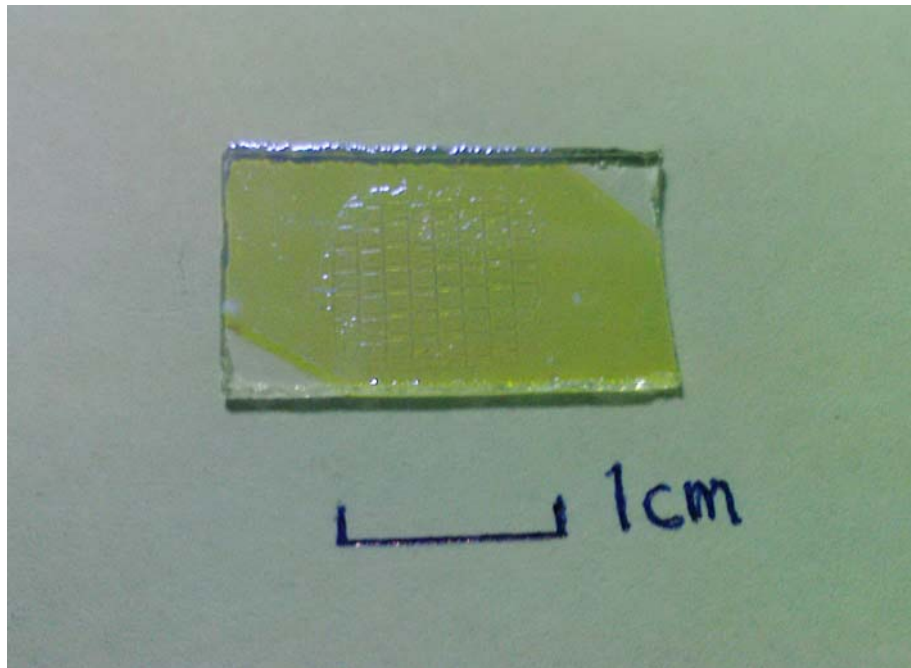
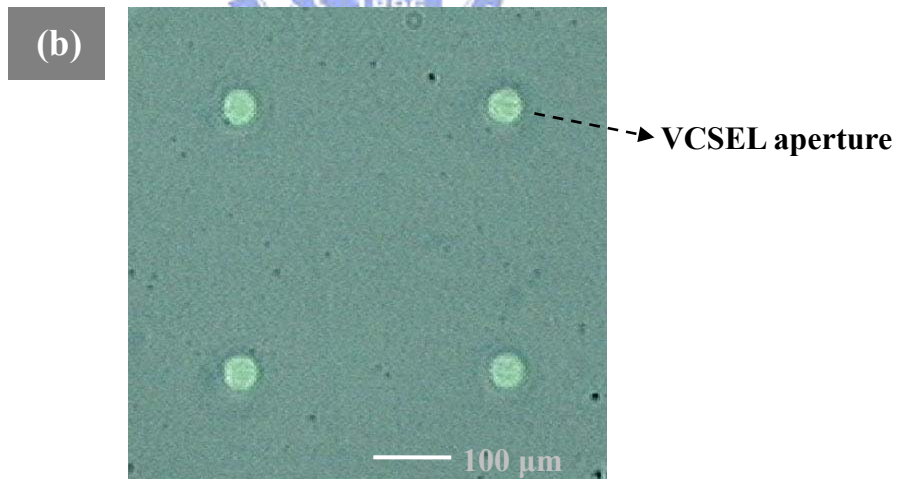


Figure 4.10 Schematic fabrication steps of the GaN-based dielectric DBRs VCSEL.



(a)



(b)

Figure 4.11 (a) A photograph of the fabricated VCSEL on a silica host substrate. (b) Microscopic image of a fabricated 2x2 VCSEL array. The circular areas are the locations of VCSELs with DBRs, also serving the emission apertures.

References

- [4.1] T. E. Sale: *VERTICAL CAVITY SURFACE EMITTING LASERS*, (Research Studies Press LTD. 1995)
- [4.2] Carl W. Wilmsen, Henryk Temkin and Larry A. Coldren: *Vertical-Cavity Surface-Emitting Lasers: Design, Fabrication, Characterization, and Applications*, (Cambridge, 1999)
- [4.3] P. R. Tavernier and D. R. Clarke: *J. Appl. Phys.* **89**, 1527 (2001).



Chapter 5 Performance and characteristics of the two dielectric DBR GaN-VCSELs

5.1 Measurement setup

The fabricated two dielectric GaN-based VCSELs were optically pumped by a Nd: yttrium aluminum garnet (YAG) laser (PowerChip NanoLaser CDRH model, JDS Uniphase). The lasing wavelength is 355 nm with a repetition rate of 1 k Hz and a pulse width of 0.5 ns. As shown in Fig. 5.1, the pumping laser beam was focused with a spot size about 60 μm in diameter by an objective lens (x15) and was vertically incident on the VCSEL sample from the $\text{SiO}_2/\text{Ta}_2\text{O}_5$ DBR in order to reduce the absorption of the pumping laser by the DBR. The light emission from the VCSEL sample was collected into a fiber (100 μm in diameter) using an imaging optic and led to a spectrometer (Jobin-Yvon Triax 320) with a spectral resolution of 0.1 nm. The VCSEL sample was put in a cryostat chamber for measuring the temperature dependent characteristics. In addition, a charge-coupled device (CCD) camera was used to locate the aperture and observe the emission patterns of the VCSEL.

5.2 Threshold condition and spectrum evolution

Figure 5.2 shows laser emission intensity obtained from the emission spectra as a

function of pumping energy at room temperature. Clear threshold condition was obtained at a pumping energy of $E_{th}=270$ nJ corresponding to an energy density of 21.5 mJ/cm². Output laser intensity from the sample increased linearly with pumping energy beyond the threshold. The estimated carrier density at the threshold is on the order of 10^{20} cm⁻³ assuming that the pumping light with an emission wavelength of 355 nm has experienced a 60% transmission through the SiO₂/Ta₂O₅ DBR layers and undergone a 98% absorption in the thick GaN layer. According to a report by Park [5.1], the gain coefficient of InGaN at this carrier density is about 10^4 cm⁻¹. We estimated the threshold gain (g_{th}) of our VCSEL using the equation $g_{th} \geq 1/(\xi L_a) \times \ln(1/R_1R_2)$, where ξ is the axial enhancement factor, L_a is the total thickness of the InGaN MQWs and R_1 and R_2 are the reflectivities of the dielectric DBRs. Since the active region covers half the emission wavelength, ξ is unity. We obtained an estimated gain coefficient of about 10^4 cm⁻¹ which is consistent with the above g_{th} estimated from carrier density. This also proved that the quality of the MQWs had been maintained after laser lift-off and lapping.

Figure 5.3 shows the evolution of the VCSEL emission spectrum under different pumping levels at room temperature. As the pumping energy increased, a lasing mode was obtained from one of the cavity modes that can be observed below threshold condition. When the pumping energy is below the threshold, the spontaneous

emission spectrum shows multiple cavity modes as shown in Fig. 5.4. The cavity length of the VCSEL can be estimated by

$$\Delta\lambda = \frac{\lambda^2}{2\left(n - \frac{dn}{d\lambda}\lambda\right)L},$$

where λ is the wavelength of cavity mode, L is cavity length and $n - \frac{dn}{d\lambda}\lambda$ is refractive index of the cavity with taking wavelength dispersion into consideration.

The cavity modes spacing show by the PL emission is about 7 nm corresponding to a cavity length of 4.3 μm , which is nearly equal to the thickness of the epitaxial cavity.

The linewidth of each individual cavity mode is 0.8 nm. The cavity quality factor (Q factor), which is a measure of the sharpness or selectivity of a resonant cavity, therefore can be estimated from the ratio of wavelength to linewidth ($\lambda/\Delta\lambda$) is about

518. Considering the optical absorption of the GaN layer, the estimated effective cavity reflectivity based on this Q factor is about 97%, which is close to the cavity

reflectivity achieved by the two dielectric DBRs. This result indicates that the laser cavity structure was nearly intact after laser lift-off process. As pumping energy

increased above the threshold, a dominant laser emission line appeared at 414 nm with a narrow linewidth of about 0.25 nm. The lasing wavelength is located at one of

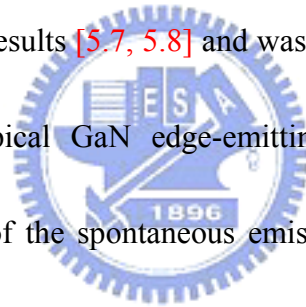
the cavity modes near the peak emission wavelength of the InGaN MQWs. Moreover, the lasing action can be observed only when the pumping source was focused on the

region where embedded between two DBRs. By contrast, no lasing action was

observed in the regions bordered by just one DBR. The results indicate that lasing operation is a vertical action but not an in-plan stimulated action caused by cracks [5.2, 5.3, 5.4, 5.5].

By normalizing the pumping energy according to E_{th} and re-plotting Fig. 5.2 in logarithmic scale, the spontaneous emission factor β which indicated the coupling efficiency of the spontaneous emission to the lasing mode, can be estimated from the difference between the heights of the emission intensities before and after lasing [5.6].

As shown by Fig. 5.5, the value of β can be estimated as about 1×10^{-3} which was in agreement with the reported results [5.7, 5.8] and was nearly two orders of magnitude higher than that of the typical GaN edge-emitting semiconductor lasers [5.9], indicating the enhancement of the spontaneous emission into a lasing mode by the high cavity quality factor (cavity Q factor) of the microcavity of the VCSEL structure.



The laser emission patterns of the VCSEL were examined from the aperture using a CCD camera and a video analyzer (Beam View Analyzer 2.2, Coherent Inc.).

Figure 5.6(a) shows the 2-D contour plot of the spatial intensity distribution of the laser beam. The cross-section profiles (white curves) show a near-Gaussian intensity distribution in both axes. Figure 5.6(b) shows the 3-D isometric plot of the spatial intensity distribution of the laser beam.

The laser emission polarization contrast between two orthogonal directions was

measured by placing a polarizer in front of the entrance of the spectrum analyzer. As shown in Fig. 5.7, the laser emission intensity varied as a function the polarizer rotation angle. The angle dependent laser intensity shows a good agreement with the fitting curve with a function of $\cos^2\theta$. The difference between the two angles of minimum intensities is 180° indicating the emission laser a linear polarization. The degree of polarization of the VCSEL emission is about 70% according to the definition of $P = \frac{I_{\max} - I_{\min}}{I_{\max} + I_{\min}}$, where I_{\max} and I_{\min} is the intensity maximum and minimum of the laseremission, respectively. The 70% degree of polarization suggests a strong polarization property of the laser emission.



5.3 Temperature dependent threshold

The temperature dependence of the lasing threshold of the VCSEL is shown in **Fig. 5.8**. The threshold pumping energy increased gradually with increasing temperature. The dependence of the threshold condition on the temperature can be expressed as $E_{th}(T) = E_0 \exp(T/T_0)$, where E_0 is a constant and T_0 is the characteristic temperature. We obtain a characteristic temperature of about 278 K for this dielectric type VCSEL for the temperature range of 58 to 322 K by linearly fitting the experimental result. This T_0 value is close to the T_0 value of 300 K for GaN-based VCSELs predicted by Honda *et al.* [5.10], and higher than the reported T_0 of 170 K [5.11] or 235 K [5.12] for the GaN-based edge-emitting laser diode. This T_0 value is also higher than the T_0 value for the hybrid DBR VCSEL we reported earlier [5.13].

The high T_0 value could be attributed to a better gain-alignment of the MQWs with the cavity mode and a lower threshold carrier density due to the higher quality factor provided by both dielectric DBRs.

5.4 Temperature dependent gain characteristics

Figure 5.8 shows the normalized photoluminescence spectra of the GaN-based VCSEL under different pumping power levels at 300K. The PL spectra indicate that there are about six axial cavity modes. Above the threshold condition, only one lasing mode at 419 nm dominates. The optical gain can be therefore estimated using the Hakki-Paoli [5.14] method to analyze these multiple cavity modes from the photoluminescence spectra below the threshold condition. By applying the Hakki-Paoli method, the gain in a VCSEL structure can be expressed as

$$G(\lambda) = \frac{\Gamma}{d_a} \ln \left[\frac{(I^+)^{\frac{1}{2}} + (I^-)^{\frac{1}{2}}}{(I^+)^{\frac{1}{2}} - (I^-)^{\frac{1}{2}}} \right] - \left(\frac{1}{2d_a} \right) \ln(R_1 R_2) + \frac{\alpha_i L}{d_a},$$

where λ is the wavelength at which the cavity modes are being measured. Confinement factor of the laser structure is estimated as $\Gamma = 0.05$ by calculating the spatial overlap between the optical field and MQWs layers in the VCSEL cavity, d_a is the thickness of ten quantum wells, I^+ and I^- are the maximum and minimum PL intensities for each cavity mode obtained from the measured PL spectra, R_1 and R_2 are DBRs reflectivities which are 99% and 98%, respectively, α_i is the average internal loss of the cavity, which is dominated by the absorption of thick GaN layer and was set to be 30 cm^{-1} [5.15] and L is the cavity length. Under different pumping levels, the I^+ and I^- would vary and the individual gain for each cavity modes can be

obtained from the Eq. (1). The gain spectra of the VCSEL under different pumping power levels at 300K are shown in Fig. 5.9. Each data point was calculated from the corresponding cavity mode in Fig. 5.8. The gain curves show an increasing trend as the pumping intensity increases and the gain bandwidth keeps broadening. In addition, the mode peaks blue shift due to the increase of the optical gain. At room temperature, the peak gain of $2.9 \times 10^3 \text{ cm}^{-1}$ was obtained at threshold condition. The gain spectra under different temperature (at 220K, 150K and 80K) were also obtained with the same measurement and calculation method, respectively.

The pumping carrier density dependence of the peak gain of the lasing mode (at ~420 nm) is plotted in Fig. 5.10 for different measurement temperature. Here the carrier density in QWs was estimated from the power density of the pumping laser assuming that the pumping light with the emission wavelength of 355 nm has experienced a 60% transmission through the $\text{SiO}_2/\text{Ta}_2\text{O}_5$ DBR layers and undergone a 98% absorption in the thick GaN layer with a absorption coefficient of 10^4 cm^{-1} [5.16]. At room temperature, the threshold carrier density was estimated to be about $6.5 \times 10^{19} \text{ cm}^{-3}$. The figure shows that the carrier density required to reach a given gain increases with increasing temperature. We use the logarithmic law to express the relation between gain and carrier density in QWs as $g(N) = g_0 \ln(N/N_0)$, where g_0 is a constant describing the increasing rate of gain corresponding to the increasing carrier

density. The solid curves in Fig. 5.10 were fitted to the data for different measurement temperature respectively. The g_0 as a function of temperature is shown as Fig. 5.11.

Increasing of g_0 was observed as the temperature decreased. It implies that the gain increase more rapidly as a function of the injected carrier density at lower temperature, which could be resulted from several reasons. Firstly, the ratio of radiative to nonradiative recombination is higher at low temperature than that at high temperature. Secondly, carrier overflow becomes pronounced at higher temperatures resulting in less radiative recombination in the MQWs and consequently a lower gain [5.17].

Another main cause is the broadening of Fermi occupation probability function which spreads carriers over a larger energy range for a given overall carrier density. The result is a lower spectral concentration of inverted carriers, which leads to a broadening and flattening of the gain spectrum.

The linewidth enhancement factor can be measured from the amplified spontaneous emission spectra below the threshold condition [5.18]. The α -factor is the ratio of the change of the refractive index (n) with carrier density (N) respect to the change in optical gain with carrier density and can be expressed by

$$\alpha = \frac{2\pi}{L\Delta\lambda} \frac{d\lambda}{dg},$$

where λ is the wavelength of each mode peak, $\Delta\lambda$ is the cavity mode spacing, L is the cavity length, $d\lambda$ is the wavelength shift when the carrier density is varied by dN , and

dg is the change in optical gain as the carrier is changed by dN . Using Eq. (2), the α -factor can be calculated from the emission spectra under different pumping power levels below the threshold.

The calculated α -factors as a function of wavelength for different measurement temperature are shown in Fig. 5.12. The α -factor shows dependence on wavelength and is smaller at shorter wavelength. As temperature varied, taking the lasing mode for example, the α -factors decrease with the decreasing temperature. However, the increase or decrease of α -factor with respect to the temperature could be due to two different mechanisms in VCSEL operations. As the temperature increased, the lasing wavelength is detuned to the shorter wavelength side of the gain peak, thus the α is reduced as the laser operates closer to the differential gain maximum, whereas the lasing operation away from the gain maximum could increase the carrier density required to the threshold condition, and thus increase the α value [5.19]. In our case, the decrease of α values as the temperature goes down could be mainly due to the reduction of carrier density in the QWs. For the lasing mode, the α -factors varied from 2.8 to 0.6 as the temperature varied from 300K to 80K. In comparison to the InGaN/GaN edge emitting laser structure that the α value varies between 2.5 and 10 [5.20], the linewidth enhancement factor in the GaN-based VCSEL structure is smaller.

5.5 Effect of Indium inhomogeneity on laser characteristic

The laser emission patterns from the aperture show single-spot and multiple-spots emission patterns under different pumping conditions as shown in Fig. 5.13(a) and 5.13(b) at pumping energy of $1.15E_{th}$ and $1.2E_{th}$. The lasing wavelength from the each emission spot also differed in few nanometers. At low pumping energy, the emission pattern showed a single spot with a spot size of about $3 \mu m$. As the pumping energy increased, a second spot appeared showing a double spot emission pattern with a spatial separation of about $22 \mu m$ apart. The corresponding emission spectra of these two spots are shown in Fig. 5.13(c). The wavelength of the single emission spot is about 415.9 nm . For the double emission pattern, there is second emission wavelength at about 414.9 nm in addition to the 415.9 nm emission line. Since the separation between these two spots is large compared to the axial mode spacing, the difference of the emission wavelengths could be caused by either the spatial non-uniformity in InGaN MQWs or the non-uniformity in the DBR cavity.

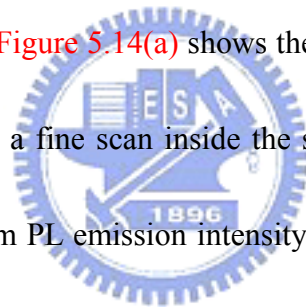
The band gap of InGaN is decided by the Indium composition in the alloy. The composition dependence of the room-temperature band gap of $In_{1-x}Ga_xN$ alloys can be expressed by the following equation [5.21]

$$E_g(x) = 3.24x + 0.77(1 - x) - 1.43x(1 - x).$$

According to this equation, we can estimate the wavelength variation induced by

Indium composition change. To simplify the calculation, the quantum effect is not considered in this estimation since we just discussed the composition dependence of emission wavelength. As shown by the lasing spectra, the difference of lasing wavelength is 1 nm, which can correspond to 0.002 (0.2%) of difference in Indium composition. This amount of variation in In composition is possible and reasonable for InGaN alloy grown by a MOCVD system.

In order to clarify the origin of these emission wavelengths variation through the aperture, we conducted the micro-PL intensity mapping of the VCSEL using a scanning optical microscopy. **Figure 5.14(a)** shows the intensity mapping of the entire aperture of the VCSEL. With a fine scan inside the square area in **Fig. 5.14(a)**, **Fig. 5.14(b)** shows the non-uniform PL emission intensity across the aperture has patches of bright areas with about 2~4 μm in size. The bright areas have about 1.8-times higher intensity than the dark areas. **Fig. 5.14(c)** shows the PL spectra of bright (marked as A) and dark (marked as B) areas. Nevertheless, spatial inhomogeneity in cavity loss due to potential micrometer-scale imperfection of the DBRs could also cause different threshold gains in spatial distribution. However, micro-PL measurement results in **Fig. 5.14(c)** show similar linewidth of the spontaneous emission for bright and dark areas, indicating no significant spatially non-uniformity in the DBRs across the circular mesa. On the other hand, the different micro-PL



intensities across the VCSEL aperture imply a non-uniform material gain distribution existed in InGaN/GaN MQW layers. In fact, the indium fluctuation was commonly observed for the expi axially grown InGaN MQWs and also the subsequent carrier localization effect had been reported [5.22]. Therefore, we believe the indium inhomogeneity in the VCSEL MQWs could be responsible for the appearance of spatially separated lasing spots within the mesa aperture and the difference in the emission wavelength could be due to the slight variation in the indium content of the MQW.

For further investigating the indium inhomogeneity in our InGaN MQWs, the as-grown cavity with InGaN MQWs used in the VCSEL structure was examined.

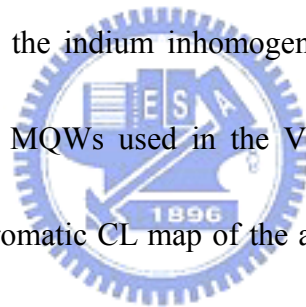


Figure 5.15 shows a monochromatic CL map of the as-grown InGaN MQWs sample at 410 nm. The CL image shows that the intensity of 410 nm emission has a non-uniform distribution implying that the In inhomogeneity in the InGaN/GaN MQWs. We believe the spatially non-uniform emission intensity results from the indium inhomogeneity in the MQWs, and consequently result in multiple-spots laser emission pattern. This result also consists with the micro-PL measurement. Figure 5.16 shows a TEM image of the MQWs in the scope of about 4 pairs of well and barrier. In the InGaN layers, some brighter areas (indicated by arrows) which could be due to the indium inhomogeneous distribution were observed. The indium separation

in the InGaN wells is believed contributing to the results we observed in the micro-PL and CL measurement. Conclude from the results of micro-PL, CL, and TEM, the indium inhomogeneity in the InGaN/GaN MQWs have a remarkable influence on the emission characteristics of GaN-based VCSELs.



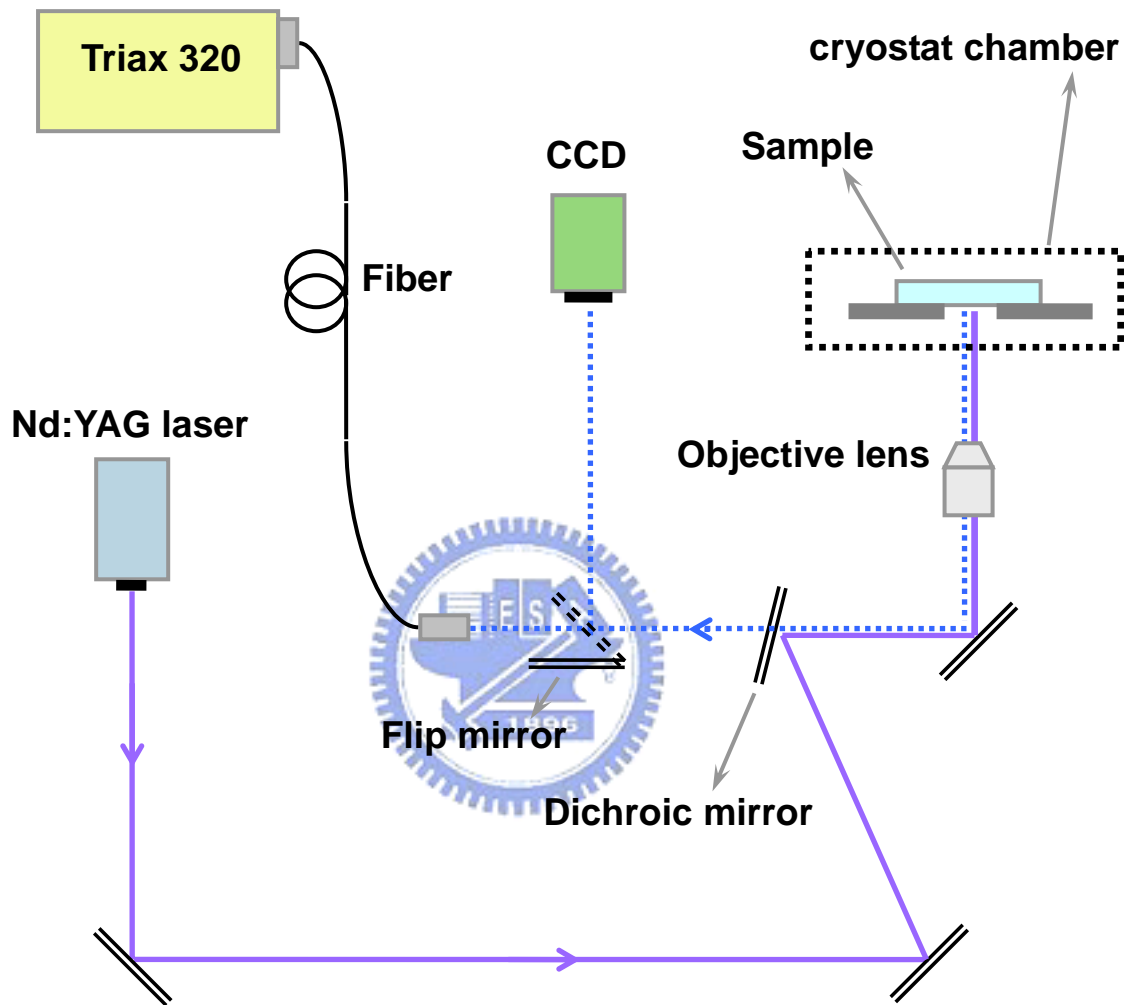


Figure 5.1 Schematic diagram of measurement setup for the characteristics of the GaN-based two dielectric DBRs VCSEL.

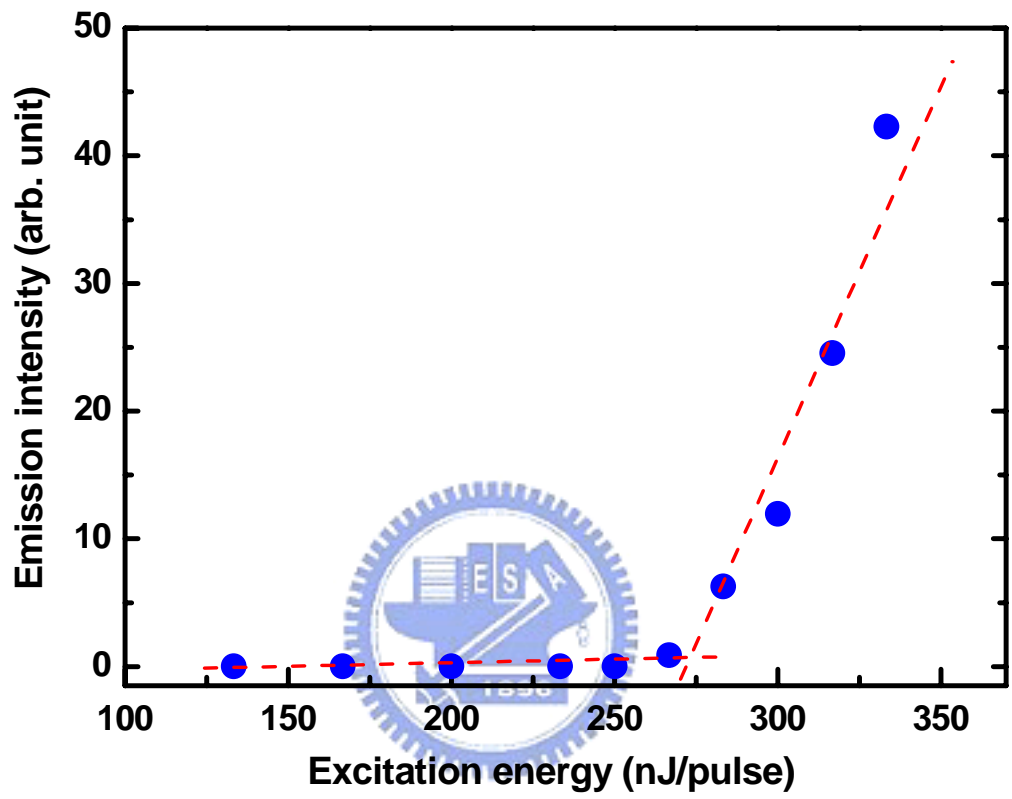


Figure 5.2 Laser emission intensity obtained from the emission spectra as a function of pumping energy at room temperature

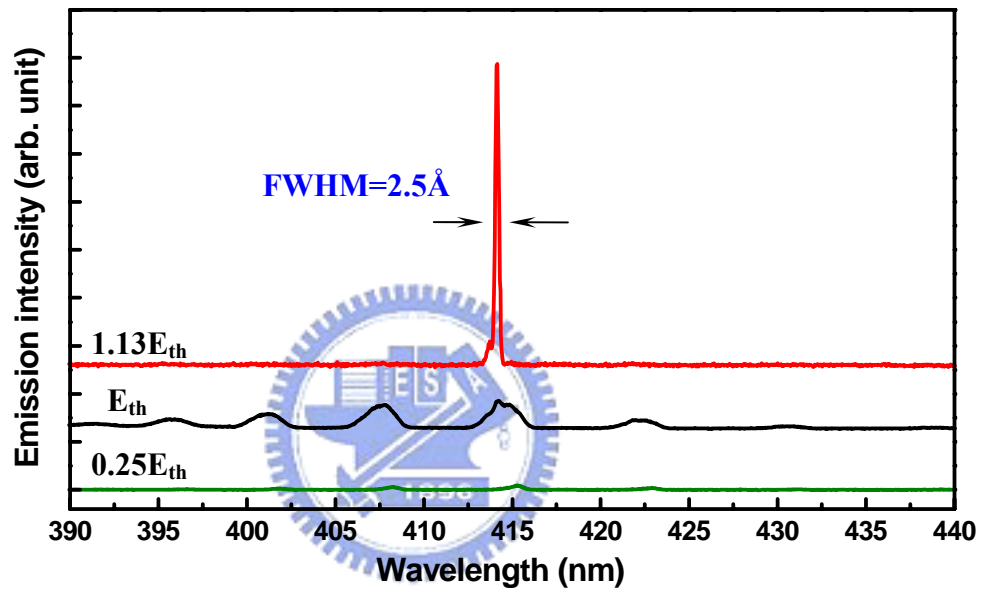


Figure 5.3 Spectral evolution of the VCSEL emission different pumping levels.

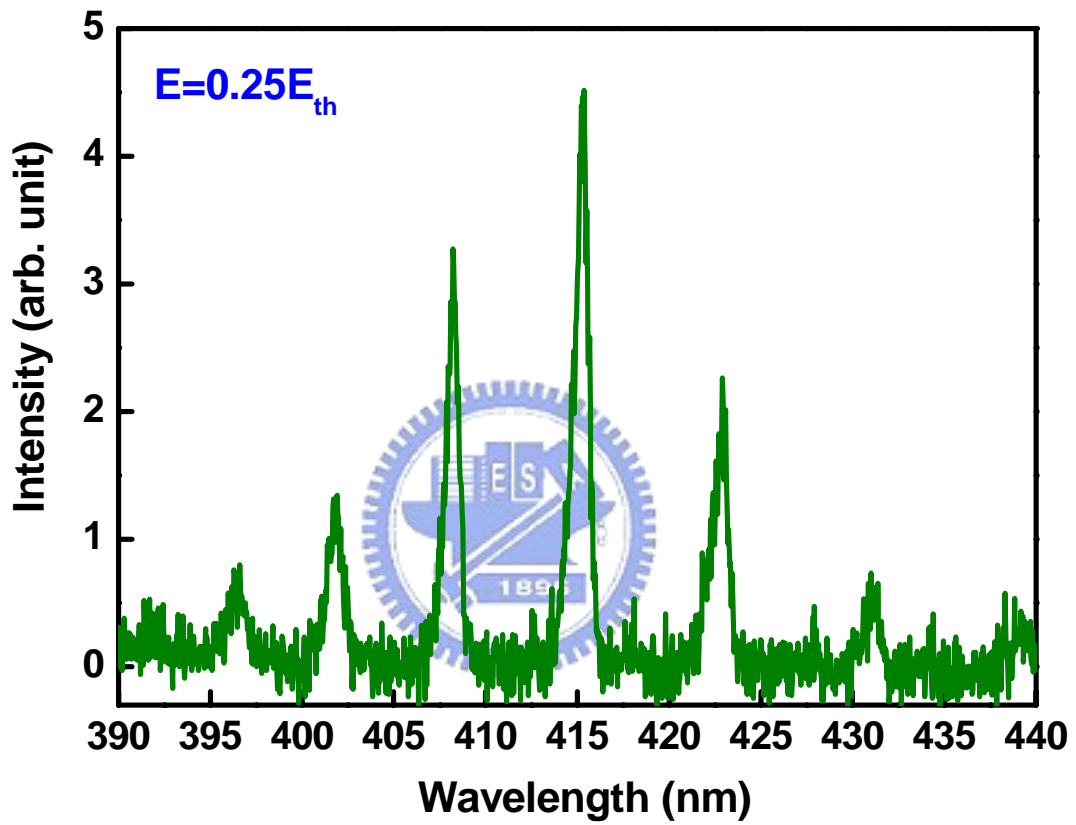


Figure 5.4 Spontaneous emission spectrum below threshold condition shows multiple cavity modes.

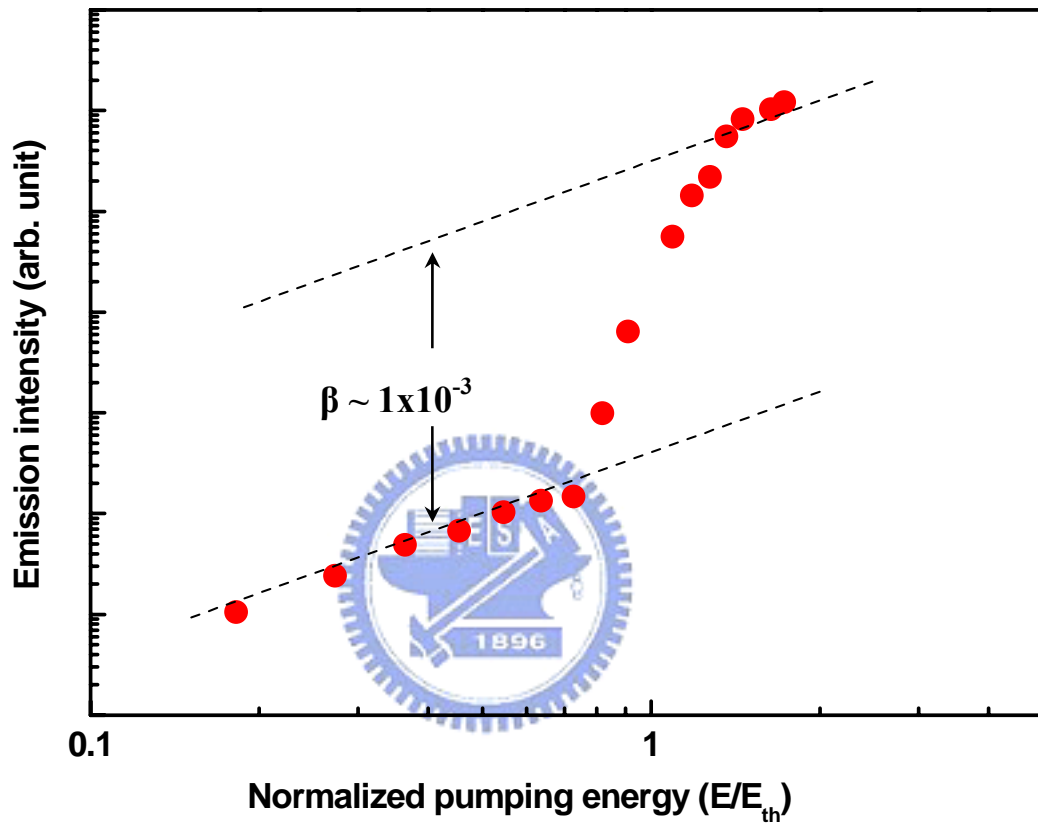


Figure 5.5 Laser emission intensity as a function of normalized pumping intensity in logarithmic scale.

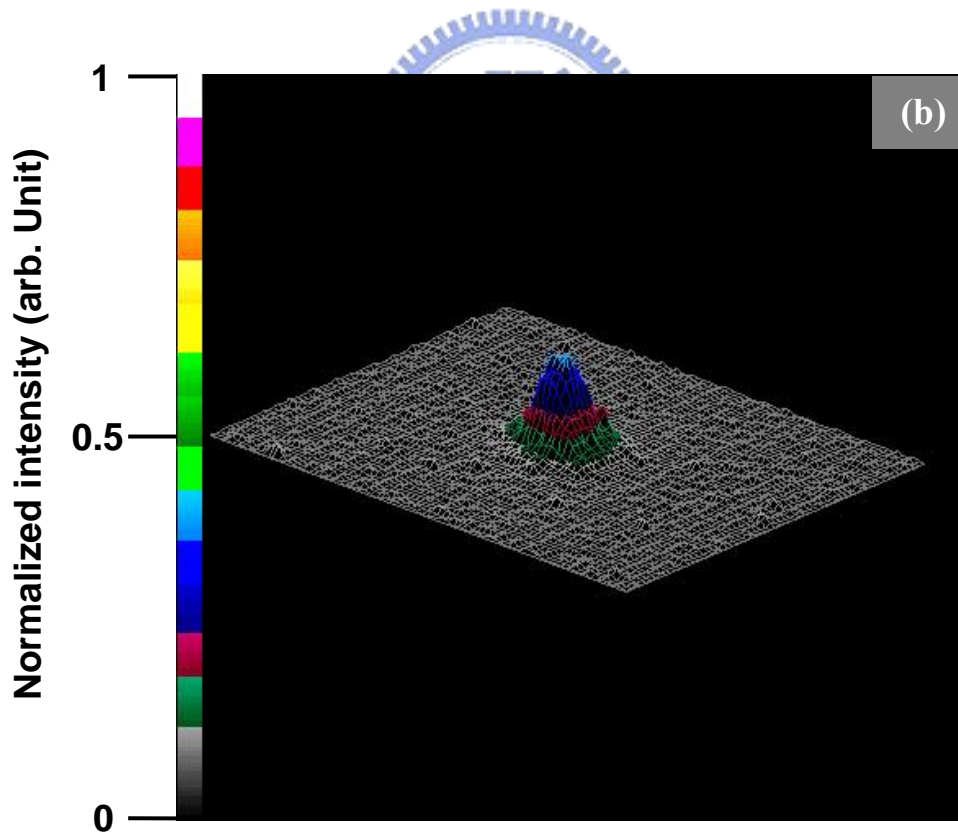
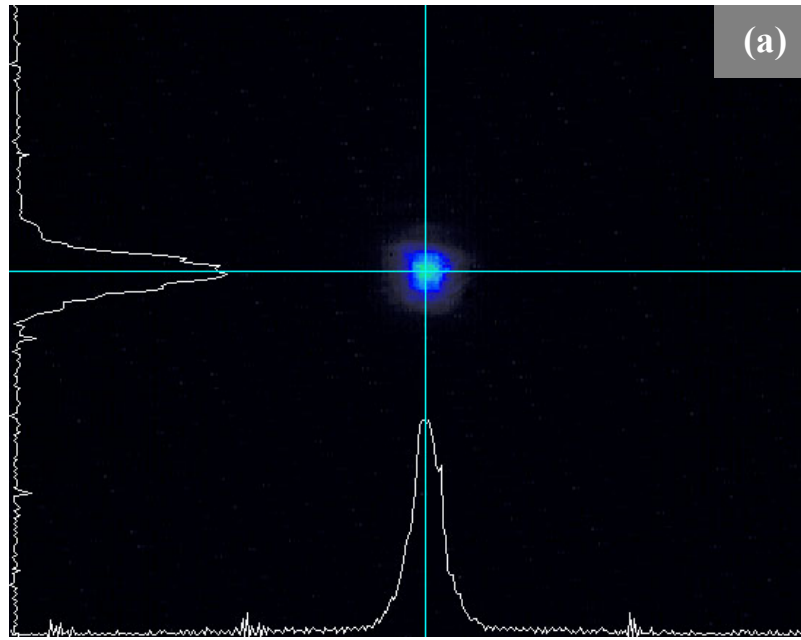


Figure 5.6 2-D contour plot (a) and 3-D isometric plot of the spatial intensity distribution of the laser beam from the VCSEL.

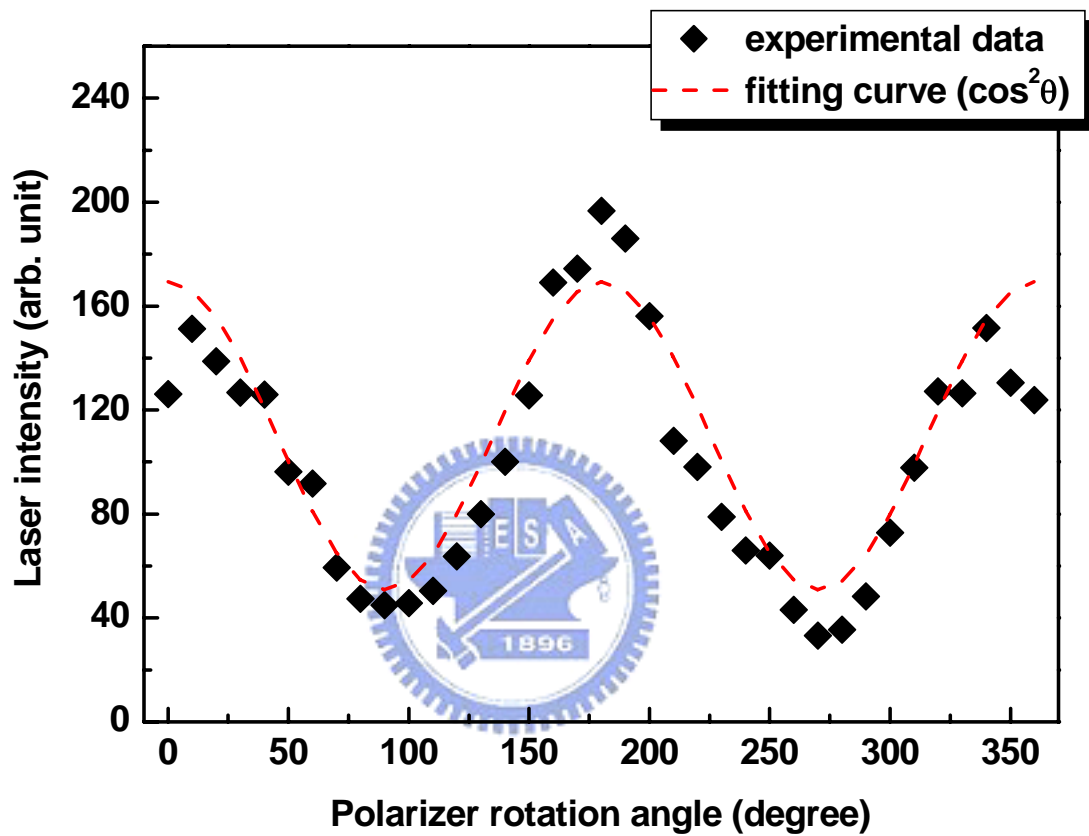


Figure 5.7 The angle dependent laser intensity.

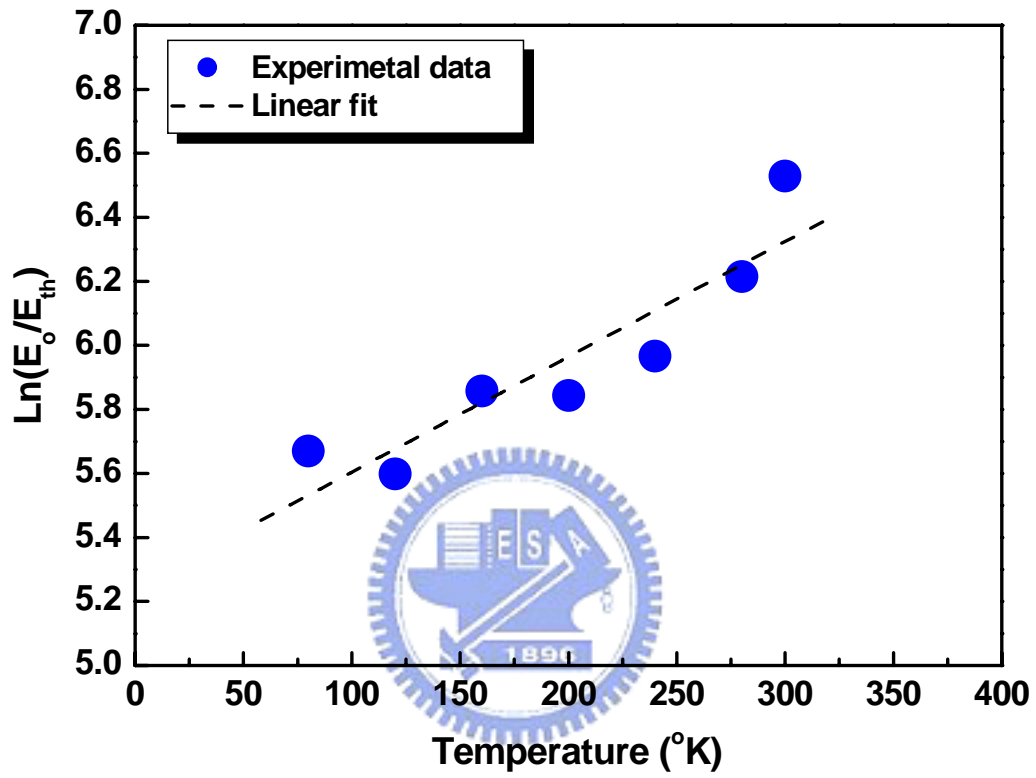


Figure 5.8 Temperature dependence of the lasing threshold of the VCSEL.

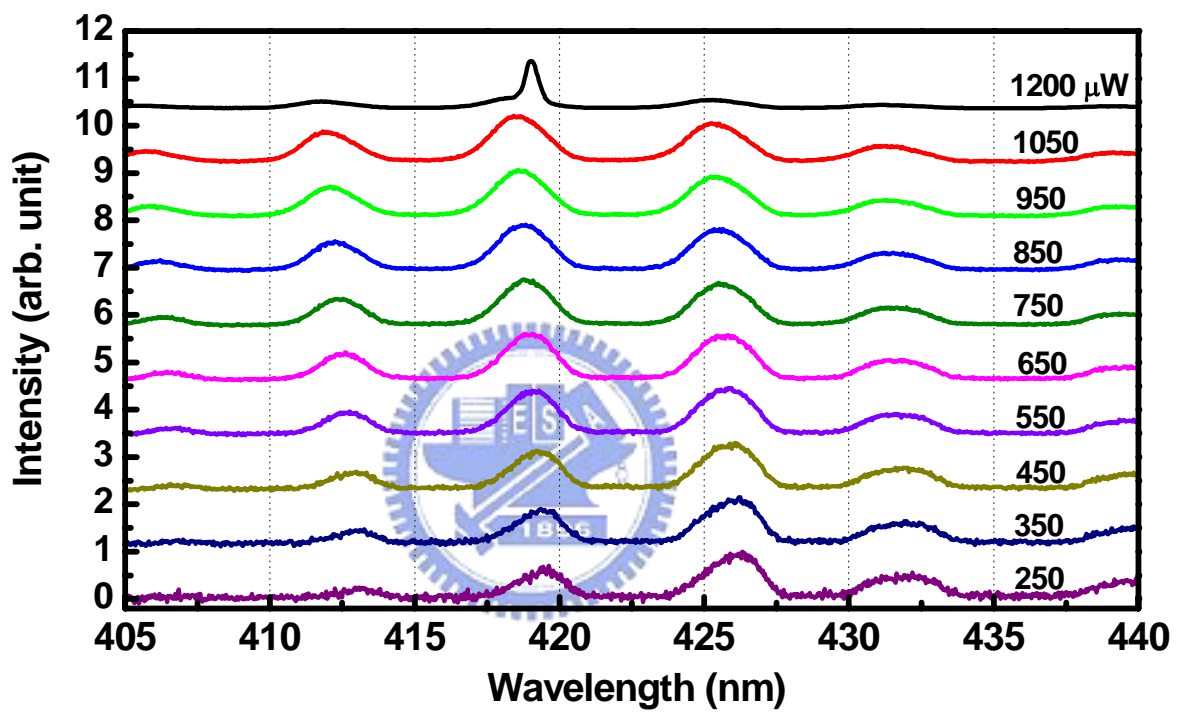


Figure 5.9 Normalized photoluminescence spectra of the GaN-based VCSEL under different pumping power levels at 300K.

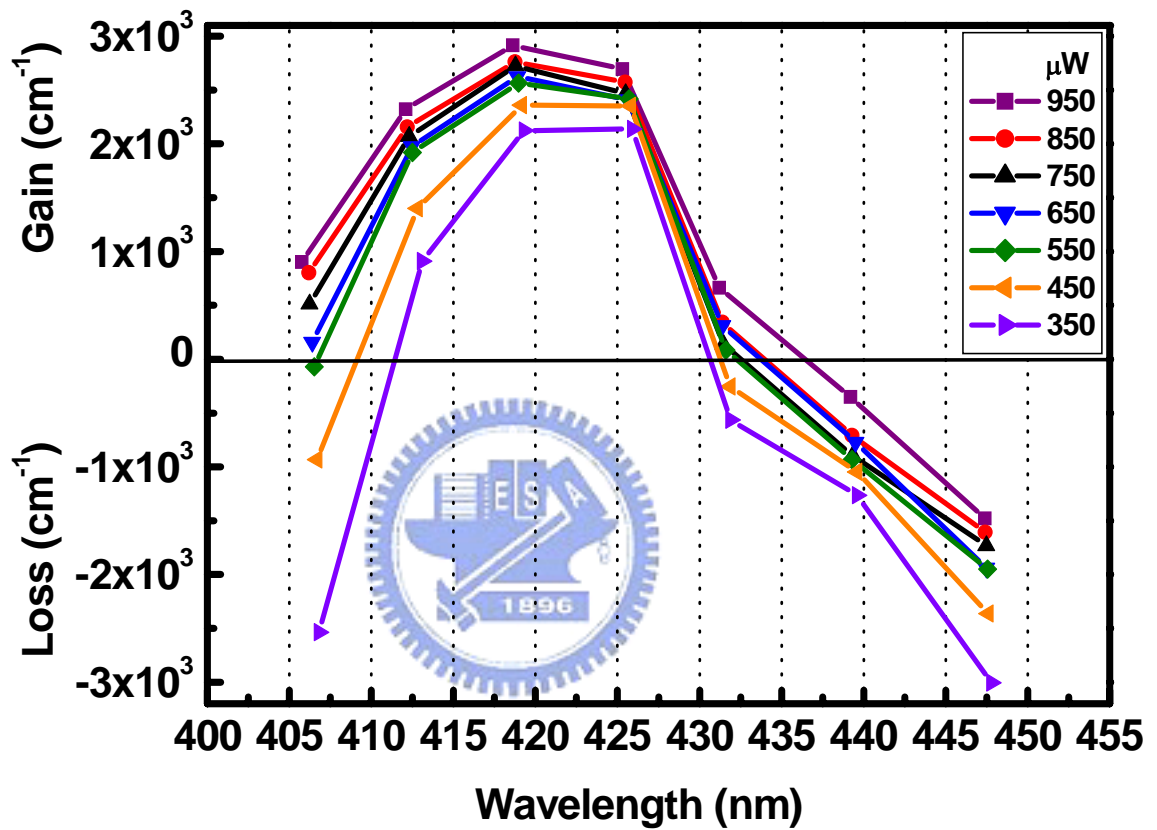


Figure 5.10 Gain spectra of the VCSEL under different pumping power levels at 300K.

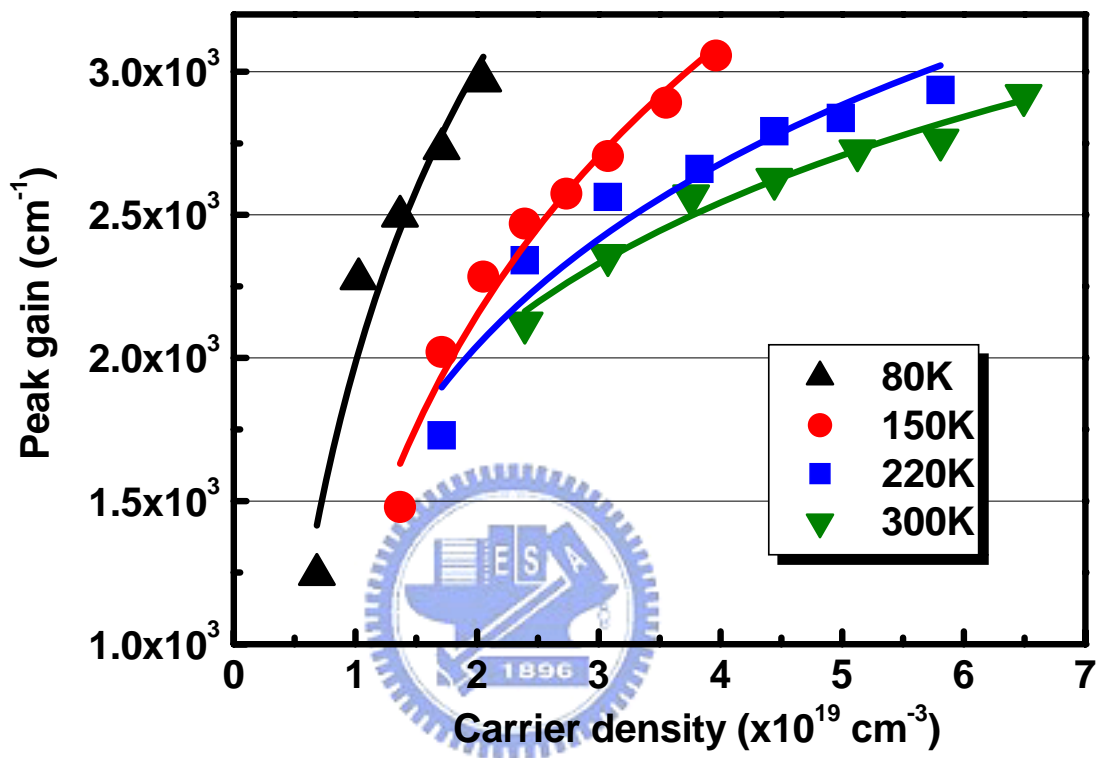


Figure 5.11 Pumping carrier density dependence of the peak gain of the lasing mode (at ~420 nm) for different measurement temperature.

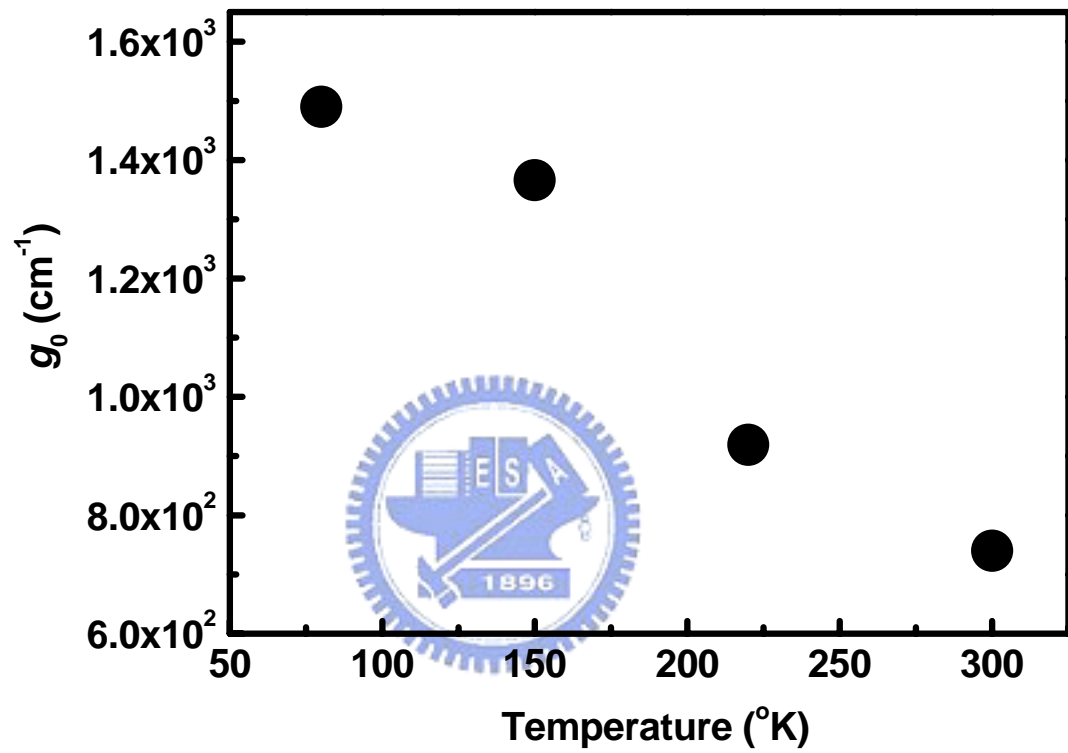


Figure 5.12 The g_0 factor as a function of temperature.

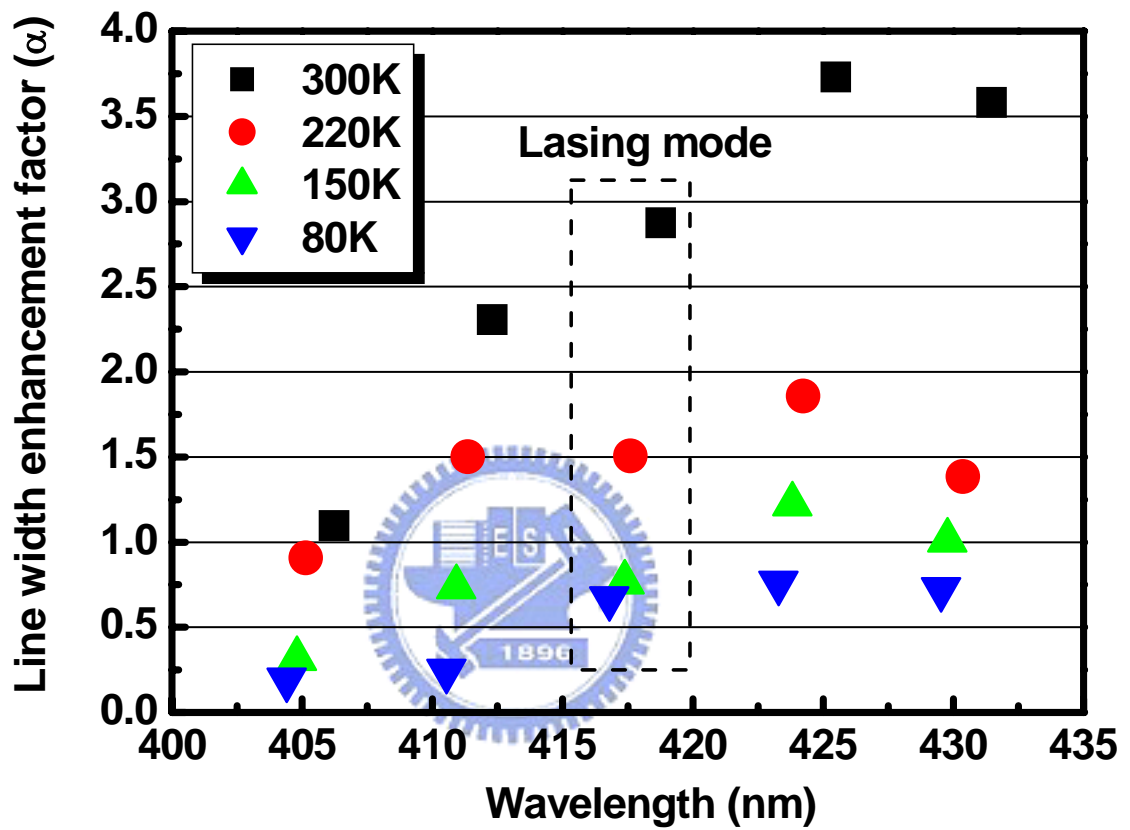


Figure 5.13 Calculated α -factors as a function of wavelength for different measurement temperature.

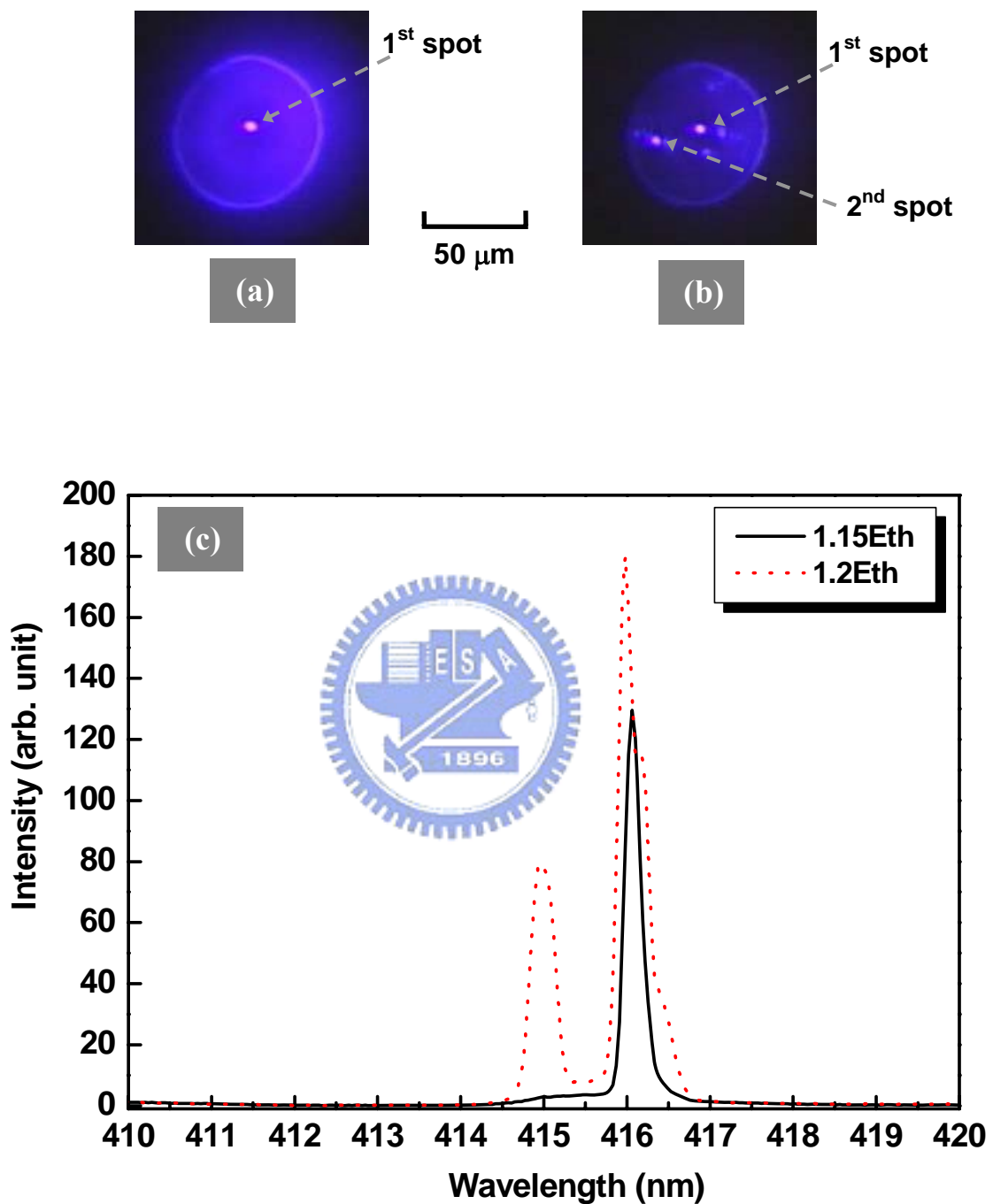


Figure 5.14 Emission pattern of the VCSEL at pumping energies of (a) $1.15E_{th}$ with single laser emission spot and (b) $1.2E_{th}$ with two laser emission spots. The arrows indicate the position of the first and second emission spots. (c) Spectra of the first emission spot and second emission spot at pumping energies of $1.15E_{th}$ and $1.2E_{th}$, respectively.

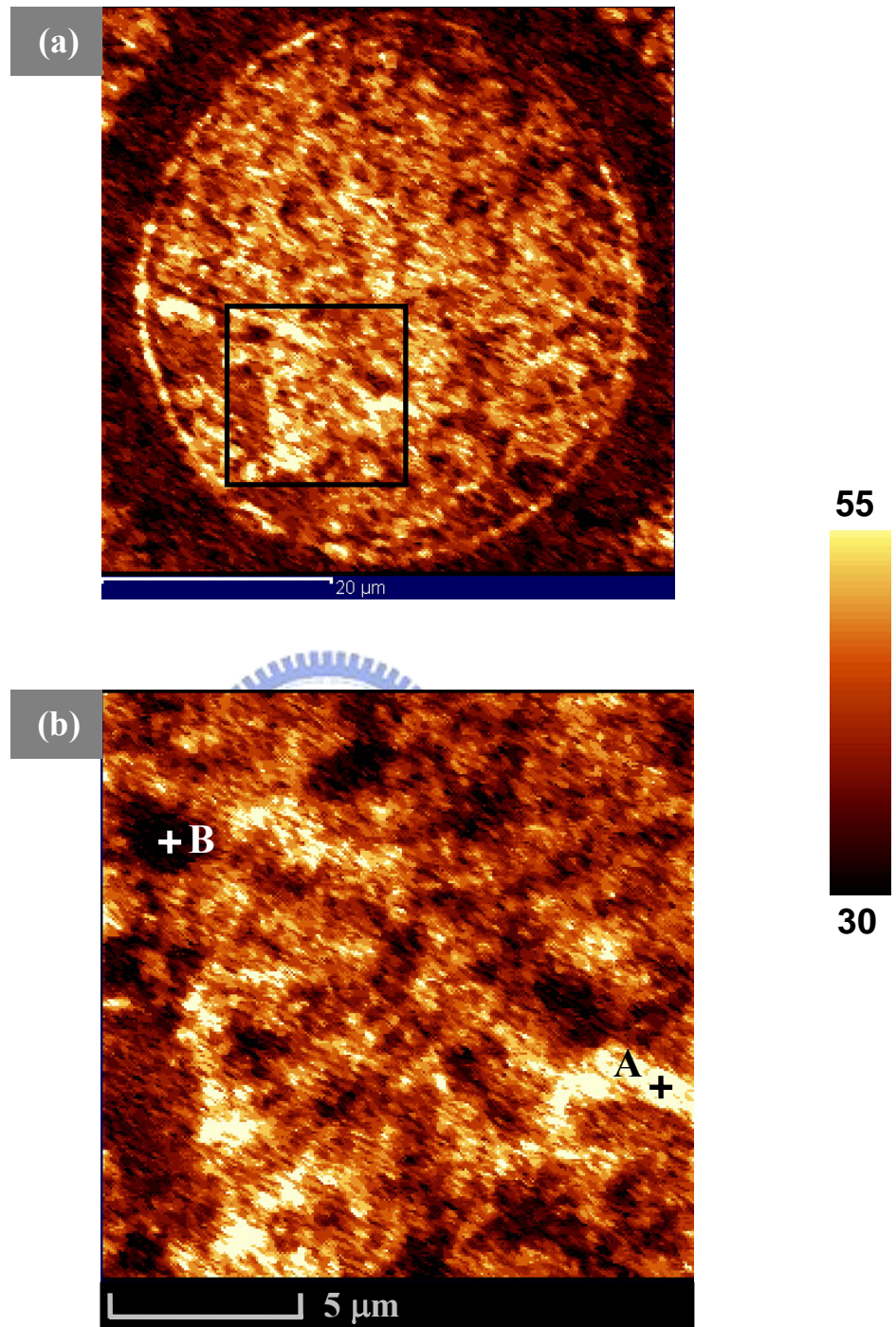


Figure 5.15 (a) Micro-PL intensity mapping image of the VCSEL aperture. (b) Fine micro-PL scan inside the square area in (a).

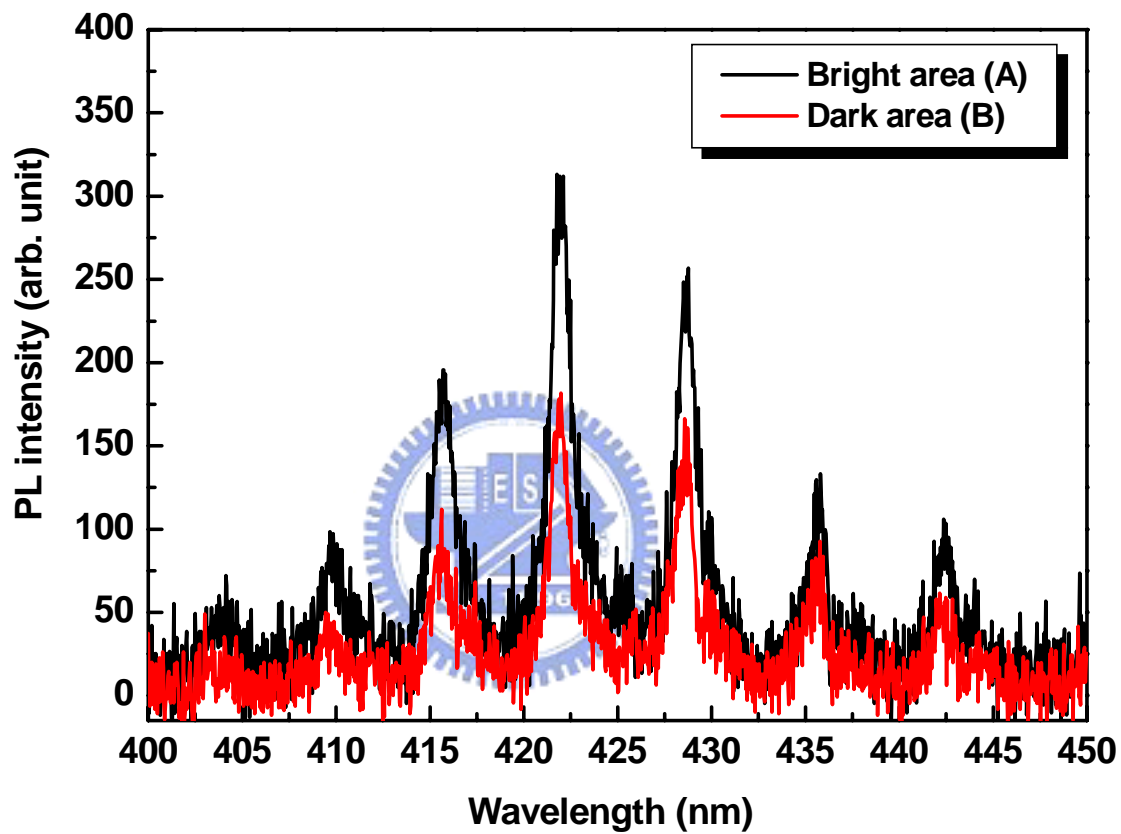


Figure 5.16 PL spectra of bright point (A) and dark point (B) areas.

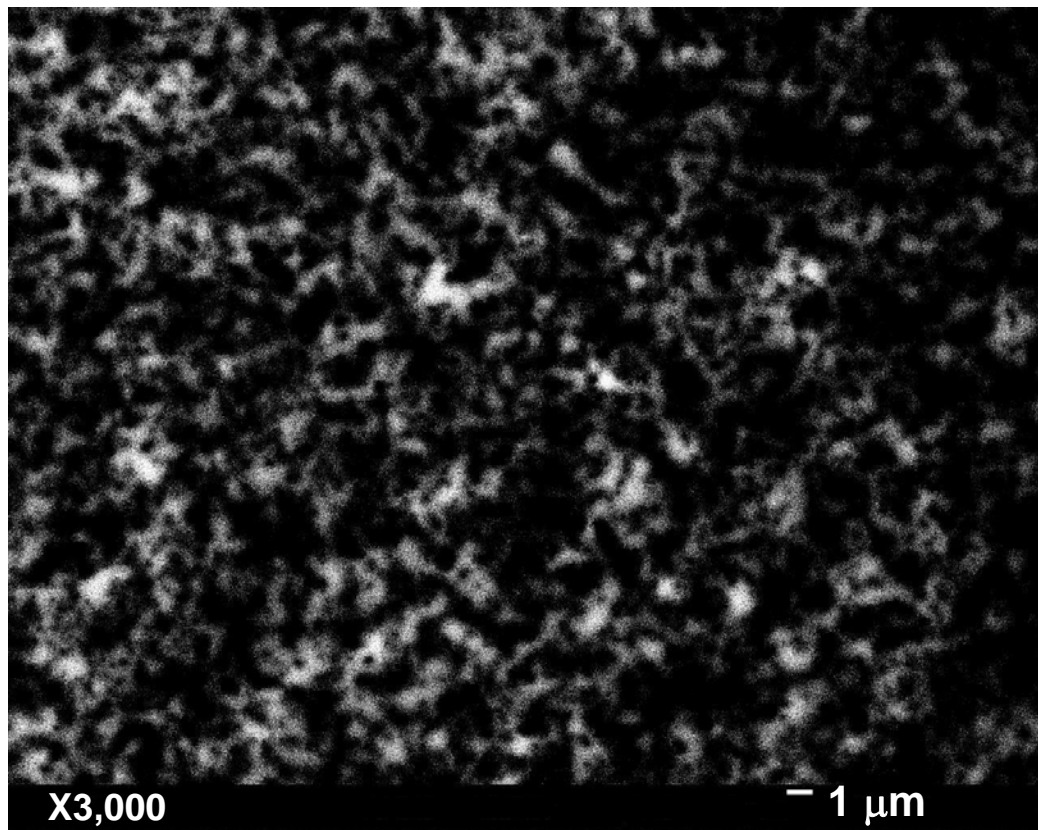


Figure 5.17 Monochromatic CL map of the as-grown InGaN MQWs sample at 410 nm.

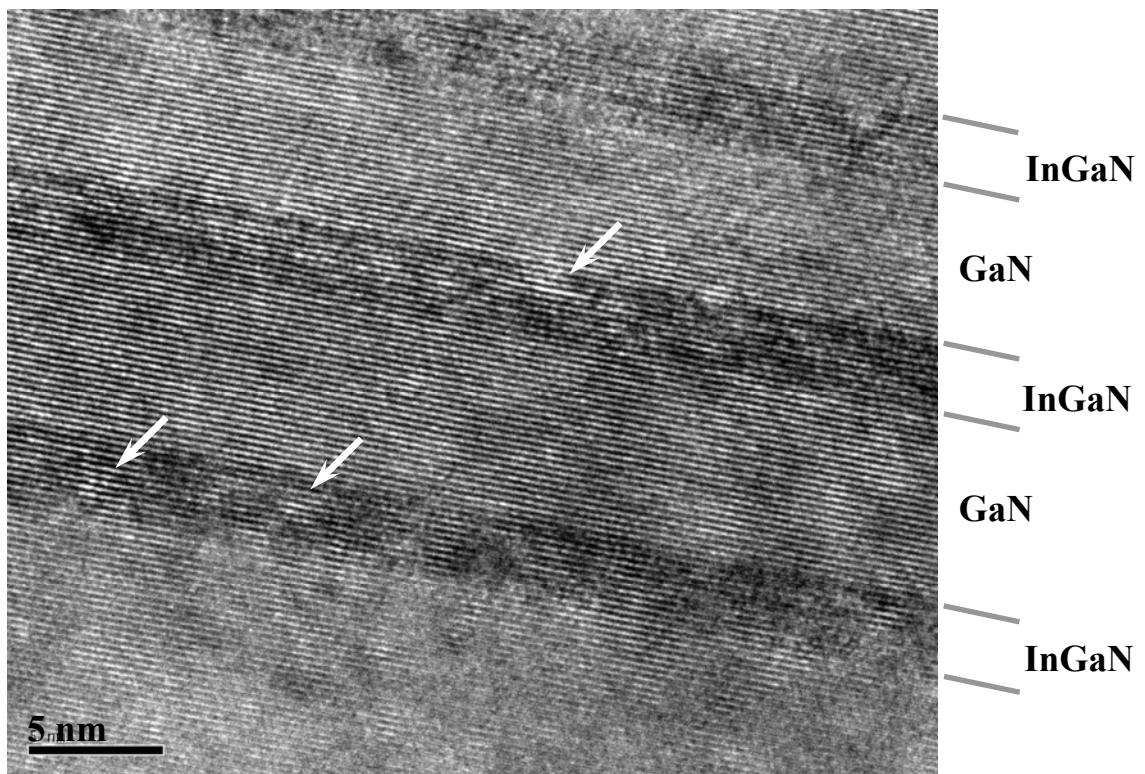


Figure 5.18 TEM image of the as-grown MQWs used in the VCSELs cavity.

Reference

- [5.1] S. H. PARK: Jpn. J. Appl. Phys. **42**, L170 (2003)
- [5.2] H. Zhou, M. Diagne, E. Makarona, A. V. Nurmikko, J. Han, K. E. Waldrip, and J. J. Figiel: Electron. Lett. **36**, 1777 (2000)
- [5.3] Y. K. Song, H. Zhou, M. Diagne, A. V. Nurmikko, R. P. Schneider, Jr., C. P. Cuo, M. R. Krames, R. S. Kern, C. Carter-Coman, and F. A. Kish: Appl. Phys. Lett. **76**, 1662 (2000)
- [5.4] M. A. Khan, S. Krishnankutty, R. A. Skogman, J. N. Kuznia, D. T. Olson, and T. George: Appl. Phys. Lett. **65** (1994) 520
- [5.5] D. M. Bagnall and K. P. O'Donnel: Appl. Phys. Lett. **68**, 3197 (1996)
- [5.6] R. J. Horowicz, H. Heitmann, Y. Kadota, and Y. Yamamoto: Appl. Phys. Lett. **61**, 393 (1992)
- [5.7] T. Tawara, H. Gotoh, T. Akasaka, N. Kobayashi, and T. Saitoh: Appl. Phys. Lett. **83**, 830 2003
- [5.8] S. Kako, T. Someya, and Y. Arakawa: Appl. Phys. Lett. **80**, 722 (2002)
- [5.9] T. Someya, R. Werner, A. Forchel, M. Catalano, R. Cingolani, and Y. Arakawa: Science **285**, 1905 (1999)
- [5.10] T. Honda, H. Kawanishi, T. Sakaguchi, F. Koyama, and K. Iga: MRS Internet J. Nitride Semicond. Res. 4S1, G6.2 (1999)
- [5.11] C. Skierbiszewski, P. Perlin, I. Grzegory, Z. R. Wasilewski, M. Siekacz, A. Feduniewicz, P. Wisniewski, J. Borysiuk, P. Prystawko, G. Kamler, T. Suski, and S. Porowski: Semicond. Sci. Technol. **20**, 809 (2005)
- [5.12] M. Ikeda and S. Uchida: Phys. Status Solidi A **194**, 407 (2002)
- [5.13] Chih-Chiang Kao, T. C. Lu, H. W. Huang, J. T. Chu, Y. C. Peng, H. H. Yao, J. Y. Tsai, T. T. Kao, H. C. Kuo, S. C. Wang, and C. F. Lin: IEEE Photonics

- Technol. Lett. **18**, 877 (2006)
- [5.14] B. W. Hakki and T. L. Paoli: J. Appl. Phys. **44**, 4113 (1973)
- [5.15] U. T. Schwarz, E. Sturm, W. Wegscheider, V. Kummler, A. Lell, and V. Harle: Appl. Phys. Lett. **83**, 4095 (2003)
- [5.16] M. O. Manasreh: Phys. Rev. B **53**, 16425 (1996)
- [5.17] A. V. Sakharov, W. V. Lundin, I. L. Krestnikov, V. A. Semenov, A. S. Usikov, A. F. Tsatsul'nikov, Yu. G. Musikhin, M. V. Baidakova, and Zh. I. Alferov: Appl. Phys. Lett. **74**, 3921 (1999)
- [5.18] I. D. Henning and J. V. Collines: Electron Lett. **19**, 972 (1983)
- [5.19] H. D. Summers, P. Dowd, I. H. White, and m. R. T. Tan: IEEE Photon. Tech. Lett. **7**, 736 (1995).
- [5.20] K.G. Gan and J. E. Bowers: IEEE Photon. Tech. Lett. **16**, 1256 (2004)
- [5.21] J. Wu, W. Walukiewicz, K. M. Yu, and J. W. Ager III, E. E. Haller, Hai Lu and William J. Schaff: Appl. Phys. Lett. **80**, 24 (2002)
- [5.22] K. Okamoto, A. Kaneta, Y. Kawakami, S. Fujita, J. Choi, M. Terazima and T. Mukai: J. Appl. Phys. **98**, 064503 (2005)

Chapter 6 Summary and future works

6.1 Summary

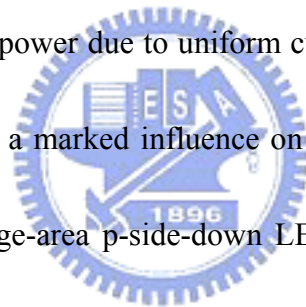
6.1.1 Large emission-area LEDs on Cu substrate

Applications such as solid-state lighting and out-door large display have promoted the development of a high optical power/efficiency GaN-based LEDs. The conventional LEDs on sapphire have inherent drawbacks including low thermal conductivity of sapphire, low light extraction efficiency and lateral current direction. By applying LLO technique, the large-emission area LEDs on Cu substrate have been demonstrated. The LEDs on Cu substrate have a high heat sink path, high reflection metal reflector and a vertical current path contributing to the electric and thermal conductivity of Cu.

In our study, a large-area GaN-based light-emitting diode (LED) $1000 \times 1000 \mu\text{m}^2$ in size with a p-side down configuration was fabricated using wafer bonding and laser LLO techniques. The thin GaN LED was transferred onto a copper substrate without peeling or cracks. The large-area LEDs showed a uniform light-emission pattern over entire defined mesa area without a transparent contact layer on the p-type GaN. The operating current of the large-area LEDs can be driven up to 1000 mA with continuously increasing light output-power. The light output-power is 240 mW with a

driving current of 1000 mA.

As the area of a single LED chip is scaled up, the current crowding effect under high current operation should be considered, while the current spreading length in the LEDs on Cu is about 400 μm . For optimizing the n-electrode pattern, we observed and reported the effect of n-electrode patterns on the optical characteristics of large-area p-side-down LLO LEDs. The light emitting patterns showed an obvious current crowding effect in the LEDs with poorly designed n-electrode patterns. The LEDs with well-designed n-electrode pattern showed a uniform distribution of light emission and a higher output power due to uniform current spreading. The geometric pattern of the n-electrode has a marked influence on the current distribution and the light output power of the large-area p-side-down LEDs without transparent contact layers. The LED with a well-designed n-electrode shows about a 4-fold increase in the light output power over a LED with a single circular n-electrode centered on the mesa. In the large-area p-side-down LEDs, the light output power and light emission pattern depends on the geometric pattern of the n-electrode. The LEDs employing the well-designed n-electrode pattern show superior $L-I$ characteristics compared with the other LEDs because the well-designed electrode pattern provides uniform current spreading.



6.1.2 Two dielectric DBRs VCSELs

Due to the lack of suitable substrate, difficulty in growing a high reflectivity DBR and p-doping in DBR layers, the development of GaN-based VCSELs have been restricted. We proposed a GaN-based VCSEL structure consists of InGaN/GaN MQWs and two dielectric DBRs with high reflectivity. The GaN-based cavity including MQWs was grown on a sapphire substrate. Then the grown cavity was embedded by two dielectric DBRs and transferred onto a silica substrate.

The laser emission characteristics of a GaN-based vertical-cavity surface-emitting laser with two dielectric distributed Bragg reflectors were investigated under optically pumped operation at room temperature. The Q factor of the VCSEL is 518, indicating a good interfacial layer quality of the structure. The laser emits emission wavelength at 415.9 nm with a linewidth of 0.25 nm. The measurement results, including the linewidth reduction, degree of polarization of 70% and emission images confined in patterned DBRs, clearly indicate a vertical lasing action. The laser has a threshold pumping energy of 270 nJ at room temperature and a characteristic temperature of 278 K. The VCSEL has a high spontaneous emission factor of about 2×10^{-3} . The Hakki-Paoli method was applied to analyze the temperature dependent optical gain and linewidth enhancement factor of the VCSELs. Due to multiple cavity modes in the structure, the optical gain can be obtained by measuring the photoluminescence

spectra below the threshold condition. At room temperature, the optical gain of $2.9 \times 10^3 \text{ cm}^{-1}$ was estimated at the threshold condition with a carrier density of $6.5 \times 10^{19} \text{ cm}^{-3}$. Under different ambient temperature, it is found that the gain increases more rapidly as a function of the injected carrier density at lower temperature. The α -factor shows dependence on the wavelength and was smaller at shorter wavelength. The α -factor at room temperature was estimated as 2.8 and decreased to as low as 0.6 at 80K. The characterization of temperature dependent gain and α -factor provides further understanding in operation of the GaN-based VCSEL. The laser emission patterns show single and multiple emission spots spatially with different emission spectra under different pumping conditions. μ -PL intensity mapping indicated that the nonuniform PL emission intensity across the VCSEL aperture. The CL and TEM images of the as-grown cavity used in the VCSEL also show the inhomogeneity of indium composition in the InGaN/GaN MQWs. The inhomogeneous material gain distribution could be due to the fluctuated indium composition in the MQW active layers and could lead to remarkable spatial and spectral broadening in laser emission properties and degrade the VCSEL performance.

6.2 Future works

Since the optically pumped lasing action of the two dielectric DBRs VCSEL have been demonstrated, current injection GaN-based VCSELs are desired to be achieved. Recently, electrically driven cw lasing of a GaN-based VCSEL was reported [6.1]. The VCSEL consists of an epitaxially grown GaN/AlN DBR, a GaN cavity with InGaN/GaN MQWs and a Ta₂O₅/SiO₂ dielectric DBR. In order to provide high reflectivity, a 29-pairs GaN/AlN was grown in the VCSEL structure of this report.

According to the two dielectric DBRs VCSEL structure, we propose a current injection GaN-based VCSEL structure with two dielectric DBRs that provide high reflectivity for reducing threshold current. Figure 6.1 shows the schematic diagram of the two dielectric DBRs VCSEL structure for electrical driving. The transparent contact on p-type GaN serves as a current spreading layer for improving uniform current distribution. Mg⁺ was implanted into the p-GaN layer before bonding process. The implanted p-GaN forms an area with high resistivity [6.2] such that the injection current flow through the area that was not implanted. The dash lines in the figure indicate the current path that is confined by the implanted area. Therefore the emission apertures of the VCSELs were defined by Mg⁺ implantation process.

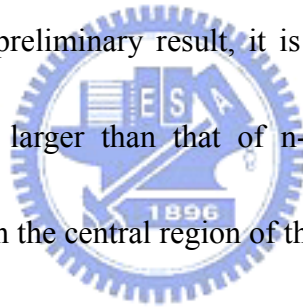
Preliminary demonstration of two dielectric DBRs VCSELs

SEM image of the VCSEL device is shown as Fig. 6.2. The n-contact and

dielectric DBR were on the n-GaN surface inside the defined mesa area. The emission aperture located at the center of the DBR could be found in the image. [Figure 6.3](#) shows the emission patterns of the two DBRs VCSELs under different current injection levels. The light emission was found inside the aperture indicating that Mg⁺ implant area provides an effective current confinement. However non-uniform emission spots were found inside the aperture. The spotty emission could be caused by two possible reasons. The inhomogeneity in indium composition in the MQWs causes the inhomogeneous emission just as indicated in the previous chapter. Another reason is that the injected current could not spread uniformly over the emission aperture because the diameters of aperture (which defined by implant area) and n-contact did not match well such that the injection current could not spread to the central region of the aperture but flow directly to the p-contact (bonding metal) along the fringe region of the aperture.

There are some issues that need to be improved and noticed for the following works. Since the ITO layer was embedded between the epitaxial GaN-based structure and dielectric DBRs, the ITO layer should be considered as a part of the resonant cavity. That is, the thickness of the ITO layer should be taken into consideration as designing the cavity length of the two dielectric VCSEL structure. The thickness of the ITO layer has influence on the overlap between ant-node of optical standing field and

MQWs. The thick thickness of the epitaxial structure is another noticeable issue. As mentioned in the previous chapter, in order to protect the MQWs from damaging during LLO, the total thickness of the epitaxial structure is about 4 μm . The thick cavity length results in a high threshold current. Thus the cavity length should be reduced in the future works. Modifying the thickness of the n-GaN by ICP etching after LLO is an alternative method. Because one of the DBRs should be deposited on the n-GaN surface, the surface roughness after ICP etching need to be concerned. The diameter ratio between emission aperture and n-contact aperture is also an important parameter. According to the preliminary result, it is suggested that the diameter of emission aperture should be larger than that of n-contact aperture such that the injected current can go through the central region of the emission aperture.



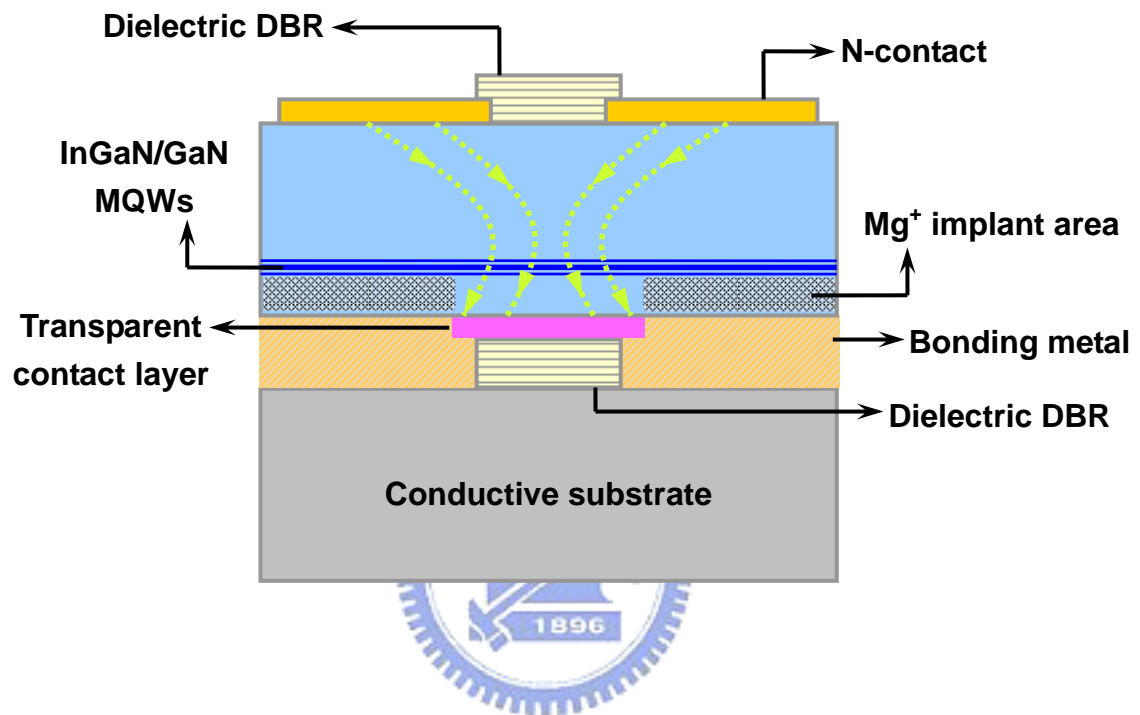


Figure 6.1 Schematic diagram of the two dielectric DBRs VCSEL structure for electrical driving.

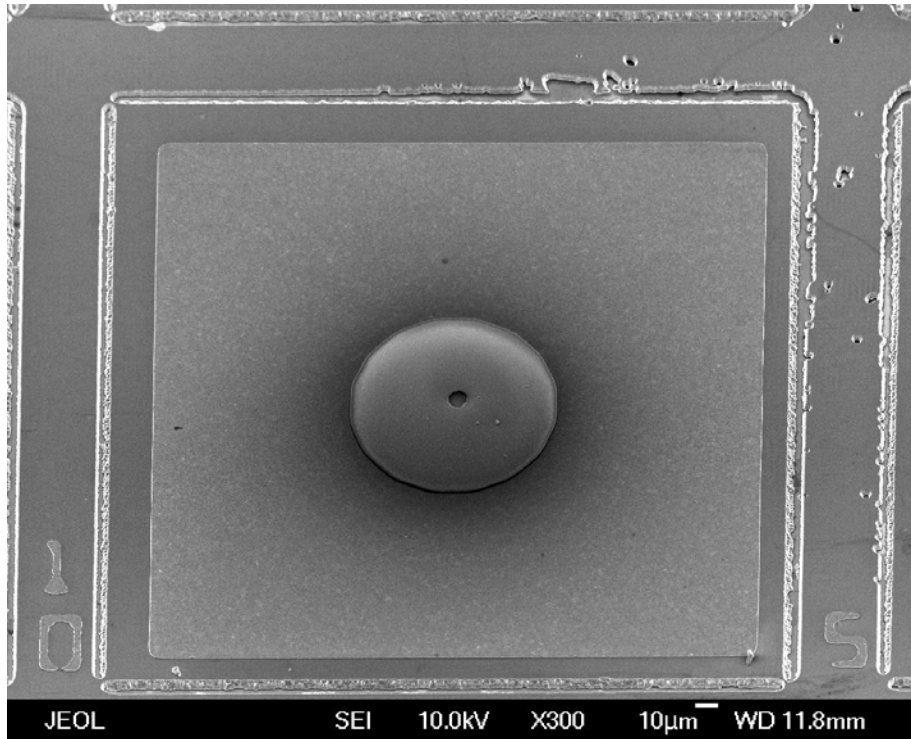


Figure 6.2 SEM image of the two dielectric DBRs VCSEL structure.

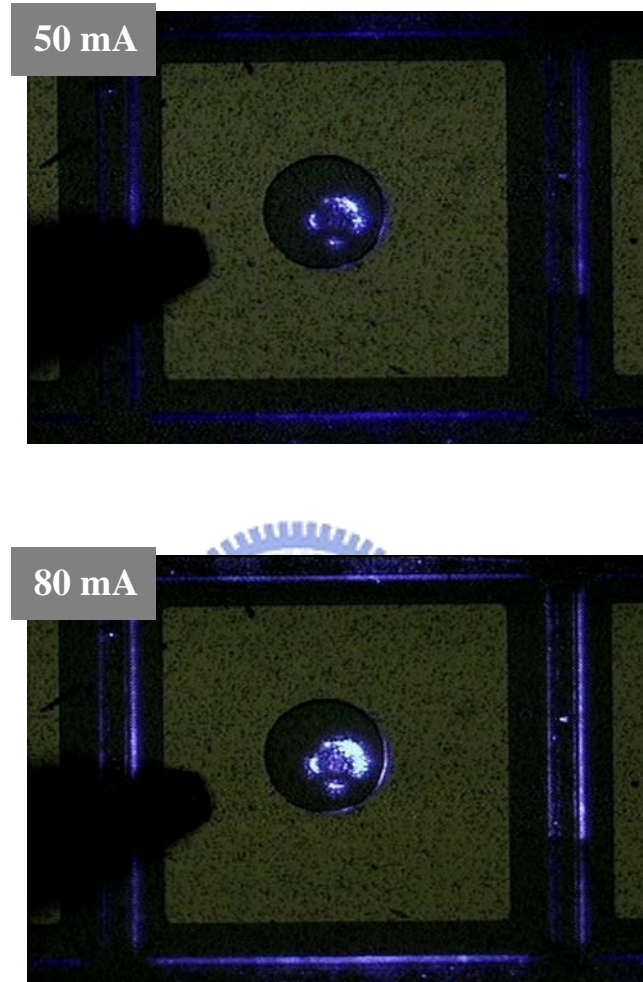


Figure 6.3 Emission images of the two dielectric VCSEL structure operated under different injection current.

References

- [6.1] T. C. Lu, C. C. Kao, H. C. Kuo, G. S. Huang, and S. C. Wang: Appl. Phys. Lett. **92**, 141102 (2001).
- [6.2] X. A. Cao and S. J. Pearton, G. T. Dang, A. P. Zhang, and F. Ren, R. G. Wilson, J. M. Van Hove: J. Appl. Phys. 87, 1091



Publication list

- [1] C. H. Chiu, T. C. Lu, H. W. Huang, C. F. Lai, C. C. Kao, **J. T. Chu**, C. C. Yu, H. C. Kuo, S. C. Wang, C. F. Lin, T. H. Hsueh: "Fabrication of InGaN/GaN nanorod light-emitting diodes with self-assembled Ni metal islands", *Nanotechnology* **18**, 445201 (2007)
- [2] T. C. Lu, T. T. Kao, C. C. Kao, **J. T. Chu**, K. F. Yeh, L. F. Lin, Y. C. Peng, H. W. Huang, H. C. Kuo, S. C. Wang: "GaN-based high-Q vertical-cavity light-emitting diodes", *IEEE Elec. Devi. Lett.* **28**, 884 (2007)
- [3] S. C. Wang, T. C. Lu, C. C. Kao, **J. T. Chu**, G. S. Huang, H. C. Kuo, S. W. Chen, T. T. Kao, J. R. Chen, L. F. Lin: "Optically pumped GaN-based vertical cavity surface emitting lasers: Technology and characteristics", *Japa. J. of Appl. Phys.* **46**, 5397 (2007)
- [4] H. G. Chen, N. F. Hsu, **J. T. Chu**, H. H. Yao, T. C. Lu, H. C. Kuo, S. C. Wang: "Strong ultraviolet emission from InGaN/AlGaIn multiple quantum well grown by multi-step process", *Japa. J. of Appl. Phys.* **46**, 2574 (2007)
- [5] C. C. Kao, H. C. Kuo, K. F. Yeh, **J. T. Chu**, W. L. Peng, H. W. Huang, T. C. Lu, S. C. Wang: "Light-output enhancement of nano-roughened GaN laser lift-off light-emitting diodes formed by ICP dry etching", *IEEE Phot. Tech. Lett.* **19**, 849 (2007)
- [6] H. W. Huang, C. C. Kao, **J. T. Chu**, W. C. Wang, T. C. Lu, H. C. Kuo, S. C. Wang, C. C. Yu, S. Y. Kuo: "Investigation of InGaN/GaN light emitting diodes with nano-roughened surface by excimer laser etching method", *Mate. Scie. and Engi. B* **136**, 182 (2007)
- [7] J. W. Shi, H. Y. Huang, C. K. Wang, J. K. Sheu, W. C. Lai, Y-S. Wu, C. H. Chen, **J. T. Chu**, H. C. Kuo, W. P. Lin, T. H. Yang, J. I. Chyi: "Phosphor-free GaN-based transverse junction light emitting diodes for the generation of white light ", *IEEE Phot. Tech. Lett.* **18**, 2593 (2006)
- [8] H. W. Huang, C. C. Kao, **J. T. Chu**, W. D. Liang, H. C. Kuo, S. C. Wang, C. C. Yu: "Improvement of InGaN/GaN light emitting diode performance with a

nano-roughened p-GaN surface by excimer laser-irradiation”, *Mate. Chem. and Phys.* **99**, 414 (2006)

[9] **J. T. Chu**, T. C. Lu, M. You, B. J. Su, C. C. Kao, H. C. Kuo, S. C. Wang: “Emission characteristics of optically pumped GaN-based vertical-cavity surface-emitting lasers”, *Appl. Phys. Lett.* **89**, 121112 (2006)

[10] H. W. Huang, **J. T. Chu**, T. H. Hsueh, M. C. Ou-Yang, H. C. Kuo, S. C. Wang: “Fabrication and photoluminescence of InGaN-based nanorods fabricated by plasma etching with nanoscale nickel metal islands”, *J. of Vacu. Scie. & Tech. B* **24** 1909 (2006)

[11] H. W. Huang, H. C. Kuo, **J. T. Chu**, C. F. Lai, C. C. Kao, T. C. Lu, S. C. Wang, R. J. Tsai, C. C. Yu, C. F. Lin: “Nitride-based LEDs with nano-scale textured sidewalls using natural lithography”, *Nanotechnology* **17**, 2998 (2006)

[12] H. W. Huang, **J. T. Chu**, C. C. Kao, T. H. Hsueh, T. C. Lu, H. C. Kuo, S. C. Wang, C. C. Yu, S. Y. Kuo: “Enhanced light output in InGaN/GaN light emitting diodes with excimer laser etching surfaces”, *Japa. J. of Appl. Phys.* **45** (4B): 3442 (2006)

[13] Y. C. Peng, C. C. Kao, H. W. Huang, **J.T. Chu**, T. C. Lu, H. C. Kuo, S. C. Wang, C. C. Yu: “Fabrication and characteristics of GaN-based microcavity light-emitting diodes with high reflectivity AlN/GaN distributed Bragg reflectors”, *Japa. J. of Appl. Phys.* **45**, 3446 (2006)

[14] **J. T. Chu**, T. C. Lu, H. H. Yao, C.C. Kao, W. D. Liang, J. Y. Tsai, H. C. Kuo, S. C. Wang: “Room-temperature operation of optically pumped blue-violet GaN-based vertical-cavity surface-emitting lasers fabricated by laser lift-off”, *Japa. J. of Appl. Phys.* **45** (4A): 2556 (2006)

[15] C.C. Kao, T.C. Lu, H.W. Huang, **J.T. Chu**, Y.C. Peng, H.H. Yao, J.Y. Tsai, T.T. Kao, H.C. Kuo, S.C. Wang, C.F. Lin: ” The lasing characteristics of GaN-based vertical-cavity surface-emitting laser with AlN-GaN and Ta₂O₅-SiO₂ distributed Bragg reflectors”, *IEEE Photo. Tech. Lett.* **18**, 877 (2006)

[16] Y. A. Chang, **J. T. Chu**, C. T. Ko, H. C. Kuo, C. F. Lin, S. C. Wang: “MOCVD growth of highly strained 1.3 μm InGaAs : Sb/GaAs vertical cavity surface emitting

laser”, J. of Crys. Grow. **287**, 550 (2006)

[17] **J. T. Chu**, C. C.Kao, H. W.Huang, W. D.Liang, C. F. Chu, T. C. Lu, Kuo H C, S. C. Wang: “Effects of different n-electrode patterns on optical characteristics of large-area p-side-down InGaN light-emitting diodes fabricated by laser lift-off”, Japa. J. of Appl. Phys. **44** 7910 (2005)

[18] H. C. Kuo, Y. H. Chang, Y. A. Chang, F. I. Lai, **J. T. Chu**, M. N. Tsai, S. C. Wang: “Single-mode 1.27- μ m InGaAs : Sb-GaAs-GaAsP quantum well vertical cavity surface emitting lasers”, IEEE J. of Sele. Topi. in Quan. Elec. **11**, 121 (2005)

[19] H. W. Huang, **J. T. Chu**, C. C. Kao, T. H. Hseuh, T. C. Lu, H. C. Kuo, S. C. Wang, C. C. Yu: “Enhanced light output of an InGaN/GaN light emitting diode with a nano-roughened p-GaN surface”, Nanotechnology **16**, 1844 (2005)

[20] C. C. Kao, Y. C. Peng, H. H. Yao, J. Y. Tsai, Y. H. Chang, **J. T. Chu**, H. W. Huang, T. T. Kao, T. C. Lu, H. C. Kuo, S. C. Wang, C. F. Lin: “Fabrication and performance of blue GaN-based vertical-cavity surface emitting laser employing AlN/GaN and Ta₂O₅/SiO₂ distributed Bragg reflector”, Appl. Phys. Lett. **87**,081105 (2005)

[21] **J. T. Chu**, H. W. Huang, C. C. Kao, W. D. Liang, F. I. Lai, C. F. Chu, H. C. Kuo, S. C. Wang: “Fabrication of large-area GaN-based light-emitting diodes on Cu substrate” , Japa. J. of Appl. Phys. **44**, 2509 (2005)

[22] Y. H. Chang, H. C. Kuo, Y. A. Chang, **J. T. Chu**, M. N. Tsai, S. C. Wang: “10 Gbps InGaAs : Sb-G-aAs-GaAsP quantum well vertical cavity surface emitting lasers with 1.27 μ m emission wavelengths”, Japa. J. of Appl. Phys. **44**, 2556 (2005)

[23] H. W. Huang, C. C. Kao, **J. T. Chu**, H. C. Kuo, S. C. Wang, C. C. Yu: “Improvement of InGaN-GaN light-emitting diode performance with a nano-roughened p-GaN surface”, IEEE Phot. Tech. Lett. **17**, 983 (2005)

[24] C. C. Kao, H. W. Huang, **J. T. Chu**, Y. C. Peng, Y. L. Hsieh, C. Y. Luo, S. C. Wang, C. C. Yu, C. F. Lin: “Light-output enhancement in a nitride-based light-emitting diode with 22 degrees undercut sidewalls”, IEEE Phot. Tech. Lett. **17**, 19 (2005)

[25] H. W. Huang, C. C. Kao, T. H. Hsueh, C. C. Yu, C. F. Lin, **J. T. Chu**, H. C. Kuo, S. C. Wang: “Fabrication of GaN-based nanorod light emitting diodes using self-assemble nickel nano-mask and inductively coupled plasma reactive ion etching”, *Mate. Scie. and Engi. B* **113**, 125 (2004)

[26] **J. T. Chu**, H. C. Kuo, C. C. Kao, H.W. Huang, C. F. Chu, C. F. Lin, and S. C. Wang: “Fabrication of p-side down GaN vertical light emitting diodes on copper substrates by laser lift-off”, *physica status solidi (c)* **1**, 2413 (2004)

[27] H. W. Huang, C. C. Kao, **J. T. Chu**, H. C. Kuo, S. C. Wang, C. C. Yu, C. F. Lin: “Investigation of GaN LED with Be-implanted Mg-doped GaN layer”, *Mate. Scie. and Engi.* **113**, 19 (2004)

[28] C. F. Chu , F. I. Lai , **J.T. Chu** , C. C. Yu , C. F. Lin , H. C. Kuo , S. C. Wang: “Study of GaN light-emitting diodes fabricated by laser lift-off technique,” *J. of Appl. Phys.* **95**, 3916 (2004)

[29] T. C. Lu, J. Y. Tsai, **J. T. Chu**, Y. S. Chang, S. C. Wang: “InP/InGaAlAs distributed Bragg reflectors grown by low-pressure metal organic chemical vapor deposition” *J. of Crys. Grow.* **250**, 305 (2003)

